InGaAsP-InP Semiconductor Microcavity Geometries for Annular Bragg Reflection, Optical Switching, and Sensing

Thesis by

William M. J. Green

In Partial Fulfillment of the Requirements

for the Degree of

Doctor of Philosophy

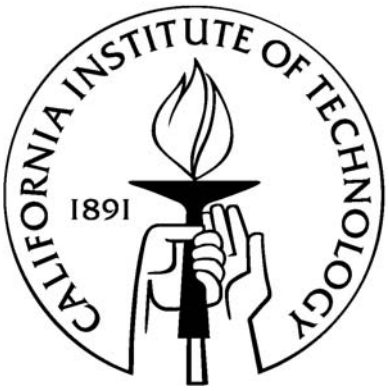

California Institute of Technology

Pasadena, California

2005

(Defended May 19, 2005)

This dissertation is dedicated to my family and friends, who have kept me going through their sincere support and encouragement.

Acknowledgements

Years from now, I am certain that I will look back upon my time at Caltech and recall how things were in "the good old days." From my very first days in Pasadena, where fast friends were made, to my last days on the California beaches before leaving one coast for the other, the years in between have been incredible.

None of this would have been so, if not for the many close friends with whom I've been blessed. Among the foremost is Dave Barsic, the coolest roommate an engineer could ever have. Of course, life would not have been the same without the other Canucks far from home, Jeff and Mel Bergthoson, Mike Johnson, Fok Leung, Carl Hansen, and Tara Klassen. I also have Tobias Kippenberg to thank for triathlons, training, the best shape I'll ever reach in my entire life, and for being a great friend. From late nights on homework in the library, to early mornings cycling to the top of Mount Wilson, we made it through a lot together.

My parents, Bill and Gloria have been a devoted source of strength during my time at Caltech. They have always given me support to follow my dreams, even though at times it must have been tough. My sister, Johanna, and brother, Nick, have helped me along many a time with words of encouragement, and we've enjoyed some good times together here in Los Angeles.

I'd like to thank Professor Amnon Yariv for making my studies at Caltech possible. His broad historical perspective and great appreciation for academic pursuits, both in optoelectronics as well in more worldly matters, has been a source of inspiration and motivation. I also owe my gratitude to Professor Axel Scherer, for welcoming me as a part of his group, and for his sincere mentorship and frank advice over the years. Professor Oskar Painter also deserves thanks for generously providing access to his

laboratory facilities.

The excellent post-doctoral fellows I've been fortunate enough to collaborate with, Koby Scheuer and Yanyi Huang, have contributed immensely to my education, both scientifically and otherwise. The labmates with whom I've spent all of my years in the Yariv Group, George Paloczi, John Choi, and Reg Lee, deserve a great deal of appreciation. Working together, and celebrating when things (finally) went right in the lab, was a lot of fun. On many occasions, I've been fortunate to have George and John as sources for particularly wise advice, and I've learned a lot from each of them. I'd also like to thank the members of the "young generation" of the Yariv Group, particularly Joyce Poon and Lin Zhu, for keeping me laughing and feeling positive during the long days and nights in the lab! And of course, things would not have been the same without Ali Ghaffari, who has been an excellent councellor and friend over the years.

Jeff and Mel Bergthorson, George and Christie Paloczi, and Tobias Kippenberg all deserve extra thanks for taking special care of me and serving as my support network, therapy group, and social life committee while Debbie was away in New York!

Finally, I owe a great deal of thanks to my wife, Debbie, whom I admire and respect more deeply each day that goes by. The excitement that she has brought to reality in my life, I would not have even considered possible on my own.

To the future, and to all it brings for each of us!

Will Green

May 5, 2005

Abstract

One of the key mandates of modern optoelectronic research is the development of compact photonic integrated circuits, capable of performing many diverse functions for the generation, manipulation, and detection of light, all on a single chip. A key practical requirement for such circuits is the development of optical devices for the localization and processing of light within extremely small dimensions. In recent years, planar microring and microdisk resonators, in which light is confined by total internal reflection, have emerged as versatile photonic elements for filling this role. The high quality factors and long photon storage times associated with the whispering-gallery modes supported by these microcavities result in several technologically useful characteristics, including narrow-band filter response, and large resonant enhancement of the circulating electric field. These properties have been exploited in numerous passive and active device applications, including optical add/drop multiplexers, all-optical switches, and tunable lasers.

This thesis describes the study of several unique ring-based optical microcavity geometries based upon the indium gallium arsenide phosphide/indium phosphide alloy semiconductor material system, undertaken in an effort to explore new optoelectronic architectures for confining and manipulating light.

The first portion of this work involves the analysis and demonstration of a new microcavity geometry, in which cylindrical Bragg reflection is used for radial optical confinement, as an alternative to total internal reflection. In this class of structures, collectively known as annular Bragg resonators, light can be guided within a ring or pillar defect layer surrounded by cylindrical Bragg mirrors. Several microcavities based upon this configuration are designed and fabricated using a thin InGaAsP

quantum well membrane. Using pulsed optical excitation, the characteristics of these structures as low threshold vertically emitting lasers is explored.

Second, a total internal reflection-based coupled waveguide-resonator geometry, having applications to low power optical switching and modulation, is analyzed. This geometry makes use of the hybrid integration of a Mach-Zehnder interferometer with a racetrack resonator. Switching takes place using the Mach- Zehnder to control the coupling parameters in the vicinity of the critical coupling condition. Characterization of the static and dynamic output response of a thermooptically actuated InGaAsP-InP hybrid switch device demonstrates good ON-OFF switching contrast, microsecond response time, and reduced switching power in comparison with a conventional Mach-Zehnder configuration.

Finally, this work concludes by examining both the annular Bragg resonator and hybrid switch geometries in application to chemical and biological sensing. Both microcavity devices are shown to possess unique characteristics making them ideal for sensitive monitoring of small changes in the refractive index of a chemical or biological analyte.

Contents

List of Figures

List of Publications

[1] J. Scheuer, W. M. J. Green, G. A. DeRose, and A. Yariv, "Lasing from a circular Bragg nanocavity with an ultra-small modal volume," accepted for publication in *Appl. Phys. Lett.*, June 2005.

[2] J. Scheuer, W. M. J. Green, G. A. DeRose, and A. Yariv, "InGaAsP annular Bragg lasers: theory, applications and modal properties," *J. Sel. Top. Quantum Electron.* **11**(2), pp. 476-484, 2005.

[3] W. M. J. Green, R. K. Lee, G. A. DeRose, A. Scherer, and A. Yariv, "Hybrid InGaAsP-InP Mach-Zehnder racetrack resonator for thermooptic switching and coupling control," *Opt. Express* **13**(5), pp. 1651-1659, 2005.

[4] L. Zhu, Y. Huang, W. M. J. Green, and A. Yariv, "Polymeric multi-channel bandpass filters in phase-shifted bragg waveguide gratings by direct electron beam writing," *Opt. Express* **12**(25), pp. 6372-6376, 2004.

[5] W. M. J. Green, J. Scheuer, G. A. DeRose, A. Yariv, and A. Scherer, "Assessment of lithographic process variation effects in InGaAsP annular Bragg resonator lasers," *J. Vac. Sci. Technol. B.* **22**(6), pp. 3206-3209, 2004.

[6] J. Scheuer, W. M. J. Green, G. DeRose, and A. Yariv, "Low-threshold two-dimensional annular Bragg lasers," *Opt. Lett.* **29**(22), pp. 2641-2643, 2004.

[7] W. M. J. Green, J. Scheuer, G. DeRose, and A. Yariv, "Vertically emitting annular Bragg lasers using polymer epitaxial transfer," *Appl. Phys. Lett.* **85**(17), pp. 3669-3671, 2004.

Glossary of Acronyms

2D - Two-dimensional

3D - Three-dimensional

ABR - Annular Bragg resonator

AFM - Atomic force microscope

BCB - Benzocyclobutene

DBR - Distributed Bragg reflector

DFB - Distributed feedback

EDFA - Erbium doped fiber amplifier

ESEM - Environmental scanning electron microscope

FD - Finite difference

FDTD - Finite-difference time-domain

FP - Fabry-Perot

FSR - Free spectral range

FWHM - Full-width-at-half-maximum

ICP-RIE - Inductively coupled plasma reactive ion etching

InGaAsP - Indium gallium arsenide phosphide

InP - Indium phosphide

IPA - Isopropyl alcohol

MIBK - Methyl isobutyl ketone

MMI - Multimode interference

MOCVD - Metal-organic chemical vapor deposition

MZI - Mach-Zehnder interferometer

NOA 73 - Norland optical adhesive, formulation 73

OSA - Optical spectrum analyzer

PECVD - Plasma enhanced chemical vapor deposition

PL - Photoluminescence

PMMA - Poly(methyl methacrylate)

Q - Quality factor

QW - Quantum well

RF - Radio frequency

SEM - Scanning electron microscope

TEC - Thermoelectric cooler

TIR - Total internal reflection

VCSEL - Vertical cavity surface emitting laser

WDM - Wavelength division multiplexing

WGM - Whispering gallery mode

Chapter 1

Introduction

1.1 Ring and disk microcavities in optoelectronics

The field of optoelectronics continues to be an important area of study in engineering and applied physics, encompassing broadly the generation, manipulation, storage, and detection of light. Much of the past and present work in this field has been performed in the pursuit of one of the key visions for optoelectronics, this being the development of compact photonic integrated circuits. Such devices are often modeled after the modern silicon microchip, in which data encoded onto electrical currents can be processed in a massively parallel fashion. By contrast, in ideal photonic integrated circuits, all data is carried and processed in the optical domain, taking advantage of the huge information capacity available in the optical and near infrared spectrum, where the electromagnetic carrier frequencies are on the order of hundreds of terahertz. Ultimately, such circuits would process multiple data channels in parallel, using a large number of passive and active photonic devices, all integrated, for example, upon a single semiconductor optical waveguide substrate.

As optoelectronic research pursues technologies to replace various electronic components with their photonic counterparts, a key motivation is the miniaturization of these components, in order to facilitate dense integration and minimize substrate consumption. Fundamentally, this requires the development of optical devices for the localization of light within extremely small dimensions. Optical microcavities have long been used as an ideal platform for the generation, processing, and localization

of light. Traditional semiconductor planar Fabry-Perot resonators can be realized in counterpart to their free-space geometries by defining two mirror surfaces using parallel cleaved crystal planes of a semiconductor slab waveguide. However, the necessity to cleave the semiconductor substrate naturally prevents the integration of such Fabry-Perot cavities with additional photonic components.

Ring and disk microcavities have emerged as excellent alternatives. The whispering gallery modes (WGMs) [1] propagating near the periphery of these cylindrical devices are confined by total internal reflection (TIR) at the curved interfaces between a waveguide core composed of a high refractive index dielectric, and a low-index cladding. These modes can be of high quality factor (Q), resulting in long photon storage times, and permitting the electromagnetic fields to build up to large amplitudes within the microcavity. As opposed to the Fabry-Perot geometry, ring and disk microcavities do not require substrate cleaving for introduction of optical feedback. Rather, the cylindrical reflecting surfaces can be generated simultaneously with any number of additional guided-wave components, using one of several parallel processes such as ion exchange, UV photocuring of polymeric materials, or reactive ion etching.

The original concept of an optical ring resonator was proposed by Marcatili in 1969 [2]. Early demonstrations of integrated ring resonators were made in direct laser written polymers [3] and ion-exchanged glass substrates [4], but due to the relatively low refractive index contrast between the core and cladding, the ring radii were on the order of several centimeters to avoid incurring severe radiative bend losses [5]. On the other hand, the high refractive index of many semiconductor materials, such as the AlGaAs-GaAs and InGaAsP-InP III-V systems, naturally permits the reduction of bend losses for small-radius microcavities particularly when low-index cladding materials are used, thus making these materials ideal platforms for the realization of dense photonic integrated circuitry. For example, the early demonstrations of microdisk semiconductor lasers [6–8] were made using these materials, with air as the outer cladding.

The majority of recent studies of ring and disk microcavities has focused upon coupled waveguide-resonator systems [9–11]. In such systems, single/multiple res-

onators are laterally/vertically coupled to one or more bus waveguides, which can either be integrated upon the same substrate as the microcavity [12, 13], or used in the form of an external fiber taper [14, 15]. When weakly coupled to the bus waveguides, the long photon storage times achieved by the high-Q WGMs can have a significant impact upon the propagation of light through the bus, imparting, for example, a narrow-band filter response [16], highly non-linear phase response [17], and large cavity enhancement of the electric field [18]. These characteristics have been used to propose and implement a wide range of passive and active devices, including all-pass [19] and tunable add/drop [20] filters, wavelength-selective mirrors [21], all-optical switches [22, 23], wavelength convertors [24], tunable lasers [25], and biochemical sensors [26, 27]. More complex architectures, incorporating chains of ring and disk resonators coupled to one another, have been suggested for observation of slow light [28, 29], development of delay lines [30, 31], and the study of optical analogues to electromagnetically induced transparency in atomic systems [32–34]. Furthermore, high-Q ring and disk microcavities have proven useful in the fundamental study of nonlinear optical processes, where the large resonant enhancement of the electromagnetic field within the cavity has enabled observation of numerous stimulated nonlinearities at low threshold pump powers, including Raman scattering and Kerr-induced parametric oscillation [35–37].

The body of this thesis is split into the study and demonstration of two classes of novel optical microcavities. The first type of resonator treated is a new ring microcavity geometry, in which cylindrical Bragg reflectors provide radial optical confinement as opposed to TIR. The second class of device investigated is an index guided ring resonator architecture with applications to low power optical modulation and switching, using electrical control of waveguide-resonator coupling. This work continues the effort to explore new optoelectronic geometries for confining and manipulating light.

1.2 Choice of material system

While the microcavity systems introduced below can be realized in a number of different dielectric materials, the work presented here focuses upon the $In_{1-x}Ga_xAs_yP_{1-y}$-InP III-V semiconductor alloy system. Compositional tuning of the bandgap wavelength can be achieved through manipulation of the atomic ratios x and y during the semiconductor growth process. For material lattice matched to InP, bandgap wavelengths in the range of 1.0-1.65 μm are available [38]. Through appropriate design and material growth, the semiconductor substrates used for the devices presented here make use of the InGaAsP quaternary system to achieve either absorptive/emissive or transparent properties within the spectral region near 1.55 μm technologically relevant to modern fiber optic communication systems.

1.3 Annular Bragg resonators (ABRs)

For many of the optoelectronic technological applications mentioned above, it is desirable to obtain high-Q microring and microdisk cavities having a large free spectral range (FSR). For example, a large FSR will prevent an add/drop filter or switch used in a multi-channel wavelength division multiplexed (WDM) system from inducing cross-talk between several different wavelength channels. Increasing the FSR of ring and disk microcavities requires reduction of the cavity round-trip time, and thus, necessitates reduction of the bend radius. However, as the bend radius of microring and microdisk resonators continues to decrease, the TIR confinement mechanism becomes increasingly inefficient, leading to substantial radiative bend losses even for resonators employing high index contrast materials. Therefore, an improvement in the cavity FSR generally comes at the expense of degradation of the cavity Q.

Alternatively, Bragg reflection may be employed for in-plane radial optical confinement, as opposed to TIR. Previous theoretical and experimental studies of cylindrical microcavities making use of Bragg reflectors have treated circular distributed feedback (DFB) resonators [39–44], and disk resonators surrounded by a cylindrical Bragg

reflector [45–49]. The first portion of this thesis presents work on a novel microring cavity geometry, in which light is confined to propagate azimuthally at a radial defect layer within a cylindrical Bragg grating. This class of microcavities are collectively referred to as annular Bragg resonators (ABRs), and have been analyzed using transfer matrix, conformal transformation, and coupled mode techniques [50–52]. Microcavities of this sort are analogous to the distributed Bragg reflector (DBR) geometry in the Cartesian coordinate system [53], where light is confined within a defect layer positioned between two high-reflectivity Bragg mirrors. However, whereas the Bragg mirrors in a typical DBR provide feedback along the longitudinal axis of the cavity, the Bragg mirrors in the ABR structure are intended for optical confinement transverse to the direction of power flow within the cavity. Again in similar fashion to Cartesian Bragg gratings, the reflectivity of cylindrical Bragg mirrors can be increased by adding more grating periods. Therefore, by increasing the number of layers in the Bragg reflectors, the bend radius of an ABR microcavity can be decreased without increasing the bend losses, thus breaking the link between the bend losses and the FSR.

An overview of the subsequent chapters pertaining to ABR microcavities proceeds as follows. In Chapter 2, a transfer matrix formalism is derived for the purpose of analyzing the electromagnetic fields within cylindrical multi-layer optical structures, such as ABR microcavities. Chapter 3 makes use of this formalism to illustrate the numerical design of appropriate dielectric structures and optical mode profiles for ABR microcavities. A set of design rules for generating optimal first-order and higher-order cylindrical Bragg reflectors is outlined, and various properties of radial defect ABR guided modes are described. The fabrication of ABR devices using a thin InGaAsP quantum well membrane is described in Chapter 4, outlining the development of an epitaxial membrane transfer process required for achieving out-of-plane optical confinement. Chapter 5 presents the characterization of optically pumped low-threshold ABR lasers making use of a second-order Bragg grating design to induce vertical emission. Several properties of the laser emission are discussed, including polarization, spectral linewidth, and infrared near field intensity profiles. The influence of fabrica-

tion process variations upon the ABR emission spectrum and laser threshold is also evaluated. Furthermore, the design and lasing properties of another distinct resonator geometry are discussed, in which light is confined within a sub-micron semiconductor pillar surrounded by a cylindrical Bragg reflector.

1.4 Optical modulation and switching using controlled waveguide-resonator coupling

In addition to being useful in a multitude of static applications, coupled waveguide-resonator systems can also be operated dynamically, for example, as optical switches or amplitude modulators. For instance, by tuning an input laser into resonance with one of the longitudinal modes supported by the ring or disk cavity, and simultaneously modulating the refractive index of the resonator, the transmitted power can also be modulated. This amplitude modulation is accomplished by altering the round-trip phase condition in the cavity, thereby shifting the spectral positions of the microcavity resonances, and causing the (approximately) Lorentzian cavity transmission lineshape to scan across the stationary input laser wavelength. Several devices based upon this switching mechanism have been reported, using electrooptic polymer [54] and InP semiconductor materials [55].

In the latter portion of this document, a TIR-guided device architecture employing controlled waveguide-resonator coupling for optical modulation and switching, as opposed to tuning of the optical path length, will be discussed. This geometry can be described as a hybrid integration of a Mach-Zehnder interferometer (MZI) with a racetrack resonator, in which the MZI is used as a variable coupler. Using coupling control, amplitude modulation of an input laser tuned into resonance is accomplished by means of altering the depth of the cavity transmission lineshape, as opposed to its wavelength. Controlled waveguide-resonator coupling is advantageous with regard to modulation and switching applications, owing to the high ON-OFF contrast achievable when operating near the critical coupling point. In comparison,

achieving comparable ON-OFF contrast in switch geometries operated by tuning the resonator optical path length requires very stringent fabrication tolerances, with post-fabrication trimming [56] likely being necessary to reach the critical coupling condition. Furthermore, in comparison with a conventional MZI device, the hybrid MZI/racetrack resonator geometry requires the application of less electrical power for ON-OFF switching. Applications for which low power optical switching can be beneficial include enabling the use of low power drive electronics to reduce power consumption in an optical transmitter, and improving the link gain in analog fiber optic photonic systems [57, 58].

In Chapter 6, several techniques useful for the design and fabrication of index guided coupled waveguide-resonator systems will be presented. Two-dimensional finite-difference techniques for the modeling of optical waveguides, as well as a method for the analysis of multi-mode interference couplers, will be discussed. These techniques are then applied in Chapter 7, where the transmission characteristics of the hybrid MZI/racetrack resonator switch are analyzed. The static and dynamic performance of an InGaAsP-InP switch device, fabricated using the hybrid geometry and actuated using thermooptic effects, is subsequently characterized and compared to that of a conventional MZI switch. A set of measurements for evaluating the thermooptic coefficients in planar integrated optical waveguides is also described.

Finally, in Chapter 8, the ABR microcavities and hybrid switch geometry are related in the common application of chemical and biological sensing. Both microcavity devices are shown to possess unique characteristics enabling sensitive monitoring of small changes in the refractive index of a chemical or biological analyte.

Chapter 2

Transfer matrix formalism for multi-layer cylindrical optical structures

2.1 Introduction

The transfer matrix method [53] is a straightforward yet powerful method for analyzing optical structures composed of an arbitrary number of dielectric layers. In general terms, a transfer matrix can be used to relate the electromagnetic fields on either side of a general optical interface or region, by accounting for its dielectric properties, and by ensuring that the appropriate boundary conditions are satisfied. Therefore, transfer matrices can be used as lumped element representations of several optical building blocks, including interfaces between heterogeneous dielectrics, and propagation through transparent, lossy, or amplifying media. More complex structures can be modeled by simple matrix multiplication of these basic subcomponents. For example, the axial structures for various resonant optical cavities, including multi-section Fabry-Perot, DBR, DFB, and VCSEL geometries [53, 59–61], are particularly well suited to analysis using the transfer matrix formalism.

While the above optical resonator geometries are most often based upon a Cartesian coordinate system (i.e., axial confinement along the z-axis, transverse confinement within the x-y plane), the transfer matrix approach is equally suited to analysis of structures possessing cylindrical symmetry. For example, Yeh, Yariv, and

Marom [62] have used this method to study a multi-layer axisymmetric structure referred to as Bragg fiber, illustrated in Fig. 2.1. This geometry utilizes cylindrical Bragg mirrors to confine light within the transverse ρ-θ plane, rather than total internal reflection (TIR) as in conventional step-index fiber [63, 64]. For the Bragg fiber geometry, Yeh, Yariv, and Marom were primarily interested in optical modes confined to propagate axially within the central hollow core region, for which the axial component of the propagation constant k_z is much larger than the azimuthal component k_θ, i.e. $k_z \gg k_\theta$. The radial component k_ρ is determined by the Bragg grating.

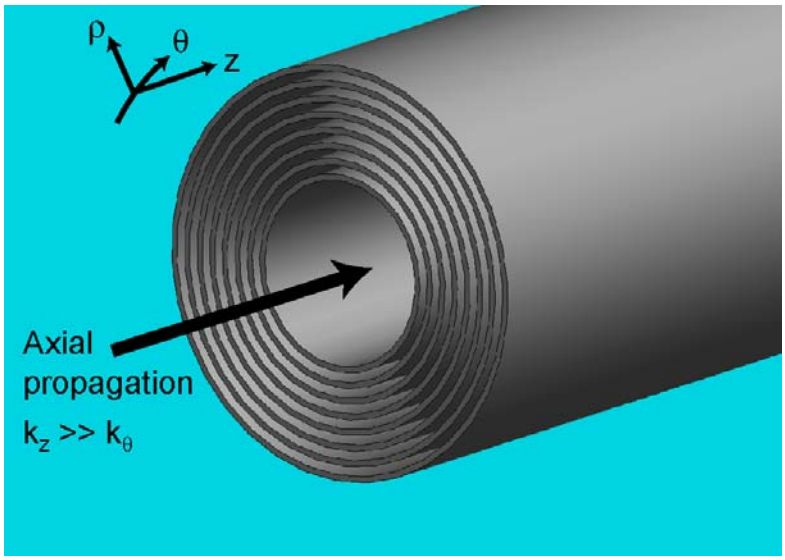

Figure 2.1: Schematic of optical Bragg fiber, in which the axially propagating light is confined to the hollow core region by Bragg reflection from the alternating high and low index cladding layers.

Figure 2.2 shows a cross-sectional view of a typical ABR geometry with a radial defect layer. In this unique structure, we are primarily interested in optical modes for which light propagates azimuthally within the wider defect layer, and is radially confined by the inner and outer cylindrical Bragg reflectors. In this case, the azimuthal component of the propagation constant is much larger than the vertical component, i.e. $k_\theta \gg k_z$. Again, the radial component of the propagation constant k_ρ is de-

termined by the inner and outer gratings. Vertical confinement along the z-axis is generally provided by total internal reflection (TIR) in practical ABR structures.

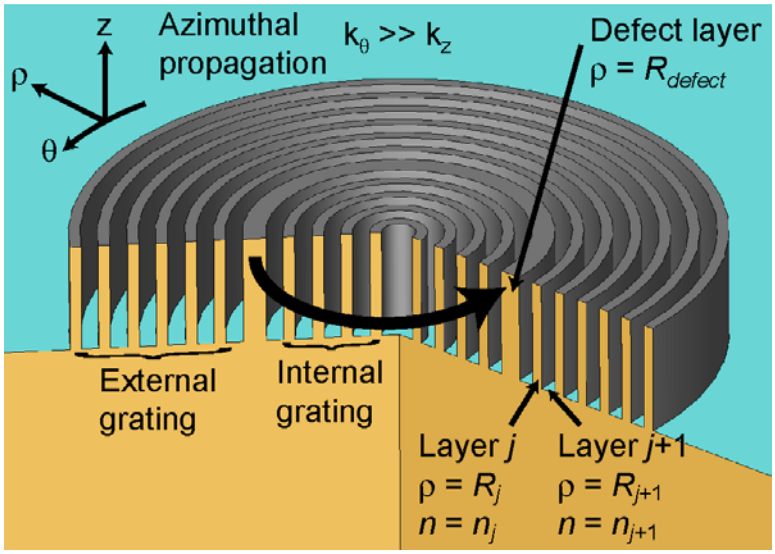

Figure 2.2: General annular Bragg resonator geometry, shown in cross-section. Light is confined to the wider defect layer and propagates azimuthally, while being reflected from the radial Bragg layers.

In this chapter, a transfer matrix formalism appropriate for description of the optical modes of cylindrical Bragg reflectors and ABR microcavities is derived. The electromagnetic modes of cylindrical multi-layer structures are analyzed both in terms of cylindrical standing waves, i.e. Bessel functions [50], and in terms of propagating waves, i.e. Hankel functions [44, 49, 52].

2.2 Transfer matrix analysis in the basis of standing waves

The vector electric and magnetic fields $\overrightarrow{E}(\overrightarrow{r},t)$ and $\overrightarrow{H}(\overrightarrow{r},t)$ within the j^{th} layer of the cylindrical ABR structure shown in Fig. 2.2 are found by solving the wave

equation. Using Maxwell's equations,

$$\begin{aligned}
\overrightarrow{\nabla} \cdot \overrightarrow{D}(\overrightarrow{r},t) &= \rho(\overrightarrow{r},t) && (2.1)\\
\overrightarrow{\nabla} \cdot \overrightarrow{B}(\overrightarrow{r},t) &= 0 && (2.2)\\
\overrightarrow{\nabla} \times \overrightarrow{E}(\overrightarrow{r},t) &= -\frac{\partial \overrightarrow{B}(\overrightarrow{r},t)}{\partial t} && (2.3)\\
\overrightarrow{\nabla} \times \overrightarrow{H}(\overrightarrow{r},t) &= \overrightarrow{J}(\overrightarrow{r},t) + \frac{\partial \overrightarrow{D}(\overrightarrow{r},t)}{\partial t}, && (2.4)
\end{aligned}$$

the constitutive relations between the electric/magnetic field vectors and the electric/magnetic displacement vectors,

$$\begin{aligned}
\overrightarrow{D}(\overrightarrow{r},t) &= \varepsilon \overrightarrow{E}(\overrightarrow{r},t) = \varepsilon_0 \overrightarrow{E}(\overrightarrow{r},t) + \overrightarrow{P}(\overrightarrow{r},t) && (2.5)\\
\overrightarrow{B}(\overrightarrow{r},t) &= \mu \overrightarrow{H}(\overrightarrow{r},t) = \mu_0(\overrightarrow{H}(\overrightarrow{r},t) + \overrightarrow{M}(\overrightarrow{r},t)), && (2.6)
\end{aligned}$$

and assuming a current-free region (i.e. $\overrightarrow{J}(\overrightarrow{r},t) = 0$), the wave equation is given by

$$\left[\overrightarrow{\nabla}^2 - \mu\varepsilon\frac{\partial^2}{\partial t^2}\right]\begin{bmatrix}\overrightarrow{E}(\overrightarrow{r},t)\\ \overrightarrow{H}(\overrightarrow{r},t)\end{bmatrix} = 0. \qquad (2.7)$$

Taking a time harmonic form for the fields, $\overrightarrow{E}(\overrightarrow{r},t) = \overrightarrow{E}(\overrightarrow{r})\exp(i\omega t)$ and $\overrightarrow{H}(\overrightarrow{r},t) = \overrightarrow{H}(\overrightarrow{r})\exp(i\omega t)$, the complex amplitudes $\overrightarrow{E}(\overrightarrow{r})$ and $\overrightarrow{H}(\overrightarrow{r})$ must satisfy the Helmholtz equation,

$$\left[\nabla^2 + k_j^2\right]\begin{bmatrix}\overrightarrow{E}(\overrightarrow{r})\\ \overrightarrow{H}(\overrightarrow{r})\end{bmatrix} = 0 \qquad (2.8)$$

where

$$\begin{aligned}
k_j^2 &= \omega^2\mu\varepsilon_j && (2.9)\\
\varepsilon_j &= \varepsilon_0 n_j^2. && (2.10)
\end{aligned}$$

Above, k_j is the wavenumber in the j^{th} layer, ω is the angular frequency, and μ, ε_j, and n_j are the magnetic permittivity, dielectric permeability, and refractive index of

the of the j^{th} layer. Since we assume the material is non-magnetic, μ is a constant for all layers. Equation 2.8 must be satisfied by all six field components, namely $E_\rho\,(\overrightarrow{r})$, $E_\theta\,(\overrightarrow{r})$, $E_z\,(\overrightarrow{r})$, $H_\rho\,(\overrightarrow{r})$, $H_\theta\,(\overrightarrow{r})$, and $H_z\,(\overrightarrow{r})$. However, if $E_z(\overrightarrow{r})$ and $H_z(\overrightarrow{r})$ are known, it is possible to obtain the other four field components [65]. Thus, Eq. 2.8 reduces to two equations. Expressing the Laplacian in cylindrical coordinates, the Helmholz equation for $E_z\,(\overrightarrow{r})$, $H_z\,(\overrightarrow{r})$ becomes

$$\left[\frac{1}{\rho}\frac{\partial}{\partial\rho}\left(\rho\frac{\partial}{\partial\rho}\right)+\frac{1}{\rho^2}\frac{\partial^2}{\partial\theta^2}+\frac{\partial^2}{\partial z^2}+k_j^2\right]\begin{bmatrix}E_z(\overrightarrow{r})\\H_z(\overrightarrow{r})\end{bmatrix}=0. \tag{2.11}$$

We now look for separable solutions to Eq. 2.11. The cylindrical symmetry of the structure suggests that the solution must be periodic in the azimuthal direction. In addition, since we wish to focus upon optical modes which propagate primarily in the azimuthal direction, we can assume a solution with a standing wave form along the z-axis. Therefore, we seek solutions of the form

$$E_z(\overrightarrow{r}) = E_z\,(\rho)\cos(\beta z+\phi)e^{im\theta} \tag{2.12}$$

$$H_z(\overrightarrow{r}) = H_z\,(\rho)\cos(\beta z+\varphi)e^{im\theta}. \tag{2.13}$$

In Eqs. 2.12-2.13, $\beta = k_z$ is the component of the propagation constant directed along the z-axis, and ϕ, φ are arbitrary phases to be determined. The azimuthal number m can take on only integer values for closed cylindrical geometries such as the ABR microcavity, i.e. $m = 0, \pm1, \pm2....$ However, for more general cylindrical reflectors, bends, and ABR waveguides, non-integral values of m are permitted. Substituting these solutions into Eq. 2.11, we obtain Eq. 2.14 for the radial part of the fields.

$$\left[\rho^2\frac{\partial^2}{\partial\rho^2}+\rho\frac{\partial}{\partial\rho}+(k_j^2-\beta^2)\rho^2-m^2\right]\begin{bmatrix}E_z(\rho)\\H_z(\rho)\end{bmatrix}=0 \tag{2.14}$$

Equation 2.14 has the form of Bessel's equation, given by

$$\left[x^2\frac{\partial^2}{\partial x^2}+x\frac{\partial}{\partial x}+x^2-m^2\right]y(x)=0. \tag{2.15}$$

The general solution is a linear superposition of Bessel functions the first and second kind having order m. Therefore, within the j^{th} layer, the solutions take the form

$$E_z(\overrightarrow{r}) = \left[A_jJ_m(\gamma_j\rho)+B_jY_m(\gamma_j\rho)\right]\cos(\beta z+\phi_j)e^{im\theta} \tag{2.16}$$

$$H_z(\overrightarrow{r}) = \left[C_jJ_m(\gamma_j\rho)+D_jY_m(\gamma_j\rho)\right]\cos(\beta z+\varphi_j)e^{im\theta}, \tag{2.17}$$

where

$$\gamma_j^2=k_j^2-\beta^2. \tag{2.18}$$

The complete solution requires that the constants A_j, B_j, C_j, and D_j must be determined in each layer.

The other four field components can be expressed in terms of $E_z(\overrightarrow{r})$ and $H_z(\overrightarrow{r})$ by making use of Maxwell's curl equations, Eq. 2.3-2.4. Equating terms for each vector component, one obtains

$$E_\theta(\overrightarrow{r}) = \frac{i}{\gamma_j^2}\left[\omega\mu\frac{\partial H_z(\overrightarrow{r})}{\partial\rho}+\frac{m}{\rho}\frac{\partial E_z(\overrightarrow{r})}{\partial z}\right] \tag{2.19}$$

$$E_\rho(\overrightarrow{r}) = \frac{1}{\gamma_j^2}\left[\frac{m\omega\mu}{\rho}H_z(\overrightarrow{r})+\frac{\partial^2E_z(\overrightarrow{r})}{\partial z\partial\rho}\right] \tag{2.20}$$

$$H_\theta(\overrightarrow{r}) = \frac{i}{\gamma_j^2}\left[\frac{m}{\rho}\frac{\partial H_z(\overrightarrow{r})}{\partial z}-\omega\varepsilon_j\frac{\partial E_z(\overrightarrow{r})}{\partial\rho}\right] \tag{2.21}$$

$$H_\rho(\overrightarrow{r}) = \frac{1}{\gamma_j^2}\left[\frac{\partial^2H_z(\overrightarrow{r})}{\partial z\partial\rho}-\frac{m\omega\varepsilon_j}{\rho}E_z(\overrightarrow{r})\right]. \tag{2.22}$$

The boundary condition at the interface between the j^{th} and $(j+1)^{\text{th}}$ layers at a radius $\rho=R_j$ requires that the tangential field components $E_z(\overrightarrow{r})$, $E_\theta(\overrightarrow{r})$, $H_z(\overrightarrow{r})$,

$H_\theta(\overrightarrow{r})$ be continuous across the interface. Using Eq. 2.16 continuity of $E_z(\overrightarrow{r})$ gives

$$\begin{aligned}&\left[A_j J_m(\gamma_j R_j) + B_j Y_m(\gamma_j R_j)\right]\cos(\beta z + \phi_j) \\ &= \left[A_{j+1} J_m(\gamma_{j+1} R_j) + B_{j+1} Y_m(\gamma_{j+1} R_j)\right]\cos(\beta z + \phi_{j+1}).\end{aligned} \tag{2.23}$$

Since this equation needs to be satisfied for all z, this implies that $\phi_j = \phi_{j+1} = \phi$. Likewise, enforcing continuity of $H_z(\overrightarrow{r})$ using Eq. 2.17 implies that $\varphi_j = \varphi_{j+1} = \varphi$. Therefore, continuity of $E_z(\overrightarrow{r})$ and $H_z(\overrightarrow{r})$ gives

$$A_j J_m(\gamma_j R_j) + B_j Y_m(\gamma_j R_j) = A_{j+1} J_m(\gamma_{j+1} R_j) + B_{j+1} Y_m(\gamma_{j+1} R_j) \tag{2.24}$$

$$C_j J_m(\gamma_j R_j) + D_j Y_m(\gamma_j R_j) = C_{j+1} J_m(\gamma_{j+1} R_j) + D_{j+1} Y_m(\gamma_{j+1} R_j). \tag{2.25}$$

Furthermore, using Eqs. 2.19, 2.16, and 2.17, the continuity of $E_\theta(\overrightarrow{r})$ gives

$$\begin{aligned}&\frac{1}{\gamma_j^2}\{\omega\mu\gamma_j[C_j J'_m(\gamma_j R_j) + D_j Y'_m(\gamma_j R_j)]\cos(\beta z + \varphi) \\ &-\frac{m\beta}{\rho}\left[A_j J_m(\gamma_j R_j) + B_j Y_m(\gamma_j R_j)\right]\sin(\beta z + \phi)\} \\ = \;&\frac{1}{\gamma_{j+1}^2}\{\omega\mu\gamma_{j+1}[C_{j+1} J'_m(\gamma_{j+1} R_j) + D_{j+1} Y'_m(\gamma_{j+1} R_j)]\cos(\beta z + \varphi) \\ &-\frac{m\beta}{\rho}\left[A_{j+1} J_m(\gamma_{j+1} R_j) + B_{j+1} Y_m(\gamma_{j+1} R_j)\right]\sin(\beta z + \phi)\},\end{aligned} \tag{2.26}$$

where $J'_m(\gamma_j R_j)$ and $Y'_m(\gamma_j R_j)$ are derivatives of the Bessel functions with respect to their own argument. From Eq. 2.24 and the derivative of Eq. 2.25 with respect to its argument, we know that

$$\begin{aligned}&\frac{1}{\gamma_j^2}\left[A_j J_m(\gamma_j R_j) + B_j Y_m(\gamma_j R_j)\right] \\ &\neq \frac{1}{\gamma_{j+1}^2}\left[A_{j+1} J_m(\gamma_{j+1} R_j) + B_{j+1} Y_m(\gamma_{j+1} R_j)\right],\end{aligned} \tag{2.27}$$

$$\begin{aligned}&\frac{1}{\gamma_j}[C_j J'_m(\gamma_j R_j) + D_j Y'_m(\gamma_j R_j)] \\ &\neq \frac{1}{\gamma_{j+1}}[C_{j+1} J'_m(\gamma_{j+1} R_j) + D_{j+1} Y'_m(\gamma_{j+1} R_j)],\end{aligned} \tag{2.28}$$

so long as $\gamma_j \neq \gamma_{j+1}$. Since Eq. 2.26 must hold for all z, this implies that

$$\cos(\beta z + \varphi) = \pm \sin(\beta z + \phi), \tag{2.29}$$

and thus,

$$\varphi = \phi \pm \frac{\pi}{2}. \tag{2.30}$$

For cylindrical structures having finite extent along the z-axis, for example, ABR devices employing a thin single-moded semiconductor membrane for vertical optical confinement, we expect from waveguide theory that $E_z(\overrightarrow{r})$ will have an extremum at the center of the membrane, i.e. located at $z = 0$, for an appropriate choice of ϕ. Therefore, we take $\varphi = \phi - \pi/2$, giving the expected z dependence for $\phi = 0$, which leads to

$$E_z(\overrightarrow{r}) = \left[A_j J_m(\gamma_j \rho) + B_j Y_m(\gamma_j \rho)\right] \cos(\beta z + \phi) e^{im\theta} \tag{2.31}$$

$$H_z(\overrightarrow{r}) = \left[C_j J_m(\gamma_j \rho) + D_j Y_m(\gamma_j \rho)\right] \sin(\beta z + \phi) e^{im\theta}. \tag{2.32}$$

The continuity of $E_\theta(\overrightarrow{r})$ can now be expressed as

$$\begin{aligned} & \frac{1}{\gamma_j^2}\{\omega\mu\gamma_j[C_j J'_m(\gamma_j R_j) + D_j Y'_m(\gamma_j R_j)] \\ & -\frac{m\beta}{\rho}\left[A_j J_m(\gamma_j R_j) + B_j Y_m(\gamma_j R_j)\right]\} \\ = \; & \frac{1}{\gamma_{j+1}^2}\{\omega\mu\gamma_{j+1}[C_{j+1} J'_m(\gamma_{j+1} R_j) + D_{j+1} Y'_m(\gamma_{j+1} R_j)] \\ & -\frac{m\beta}{\rho}\left[A_{j+1} J_m(\gamma_{j+1} R_j) + B_{j+1} Y_m(\gamma_{j+1} R_j)\right]\}. \end{aligned} \tag{2.33}$$

Similarly, using 2.21 for continuity of $H_\theta(\overrightarrow{r})$, we have

$$\begin{aligned} & \frac{1}{\gamma_j^2}\{\frac{m\beta}{\rho}[C_j J_m(\gamma_j R_j) + D_j Y_m(\gamma_j R_j)] \\ & -\omega\varepsilon_j\gamma_j\left[A_j J'_m(\gamma_j R_j) + B_j Y'_m(\gamma_j R_j)\right]\} \\ = \; & \frac{1}{\gamma_{j+1}^2}\{\frac{m\beta}{\rho}[C_{j+1} J_m(\gamma_{j+1} R_j) + D_{j+1} Y_m(\gamma_{j+1} R_j)] \\ & -\omega\varepsilon_j\gamma_{j+1}\left[A_{j+1} J'_m(\gamma_{j+1} R_j) + B_{j+1} Y'_m(\gamma_{j+1} R_j)\right]\}. \end{aligned} \tag{2.34}$$

The constants A_j, B_j, C_j, D_j satisfying the boundary conditions for the tangential field components can be expressed in matrix form [50, 66]. Writing the equations in the order of $E_z(\overrightarrow{r})$, $H_\theta(\overrightarrow{r})$, $H_z(\overrightarrow{r})$, $E_\theta(\overrightarrow{r})$, i.e. using Eqs. 2.24, 2.34, 2.25, 2.33, the matrix equation is given by

$$M_{j+1}\begin{bmatrix} A \\ B \\ C \\ D \end{bmatrix}_{j+1} = M_j \begin{bmatrix} A \\ B \\ C \\ D \end{bmatrix}_j , \tag{2.35}$$

where

$$M_j = \begin{bmatrix} J_m(\gamma_j R_j) & Y_m(\gamma_j R_j) & 0 & 0 \\ -\frac{n_j^2}{\gamma_j} J'_m(\gamma_j R_j) & -\frac{n_j^2}{\gamma_j} Y'_m(\gamma_j R_j) & \frac{m\beta}{\rho\omega\varepsilon_0\gamma_j^2} J_m(\gamma_j R_j) & \frac{m\beta}{\rho\omega\varepsilon_0\gamma_j^2} Y_m(\gamma_j R_j) \\ 0 & 0 & J_m(\gamma_j R_j) & Y_m(\gamma_j R_j) \\ -\frac{m\beta}{\rho\omega\mu\gamma_j^2} J_m(\gamma_j R_j) & -\frac{m\beta}{\rho\omega\mu\gamma_j^2} Y_m(\gamma_j R_j) & \frac{1}{\gamma_j} J'_m(\gamma_j R_j) & \frac{1}{\gamma_j} Y'_m(\gamma_j R_j) \end{bmatrix}. \tag{2.36}$$

In Eq. 2.36, we have used $\varepsilon_j = \varepsilon_0 n_j^2$, where ε_0 is the permeability of free space, and n_j is the refractive index of the j^{th} layer. Therefore, given the vector of constants

$[A\ B\ C\ D]_j$ in the j^{th} layer, the constants in the $(j+1)^{\text{th}}$ layer are given by

$$\begin{bmatrix} A \\ B \\ C \\ D \end{bmatrix}_{j+1} = M_{j+1}^{-1} M_j \begin{bmatrix} A \\ B \\ C \\ D \end{bmatrix}_j = T_j \begin{bmatrix} A \\ B \\ C \\ D \end{bmatrix}_j . \tag{2.37}$$

Repeated application of the transfer matrix T_j allows one to "propagate" the tangential field components from the innermost $j = 1$ layer to the outermost $j = N$ layer, or vice-versa, providing that $E_z(\overrightarrow{r})$ and $H_z(\overrightarrow{r})$ are known at either the innermost or outermost layer.

If $\beta = 0$, for example, when the cylindrical structure has infinite extent along the z-axis and $\partial/\partial z = 0$, the matrix M_j becomes block diagonal, indicating that there are two independent polarizations which can exist in the cylindrical structure. These polarizations are labeled as TM (transverse magnetic), with field components $E_z(\overrightarrow{r})$, $H_\theta(\overrightarrow{r})$, and $H_\rho(\overrightarrow{r})$, and TE (transverse electric), with field components $H_z(\overrightarrow{r})$, $E_\theta(\overrightarrow{r})$, and $E_\rho(\overrightarrow{r})$. The boundary condition matrices applicable to each of these decoupled polarizations are as follows.

$$M_j^{TM} = \begin{bmatrix} J_m(\gamma_j R_j) & Y_m(\gamma_j R_j) \\ \dfrac{-n_j^2}{\gamma_j} J'_m(\gamma_j R_j) & \dfrac{-n_j^2}{\gamma_j} Y'_m(\gamma_j R_j) \end{bmatrix} \tag{2.38}$$

$$M_j^{TE} = \begin{bmatrix} J_m(\gamma_j R_j) & Y_m(\gamma_j R_j) \\ \dfrac{1}{\gamma_j} J'_m(\gamma_j R_j) & \dfrac{1}{\gamma_j} Y'_m(\gamma_j R_j) \end{bmatrix} \tag{2.39}$$

Note that the labeling of polarization used here has been made in accordance with the common convention used by the planar integrated optics community [67], rather than that typically used in the description of photonic crystal devices [68].

Alternatively, a non-zero value of β can be incorporated by means of the effective index method [69]. In this method, a fully 3D structure is approximated by an "effective" 2D structure, by calculating a modal effective index n_{eff} for propagation

within the ρ-θ plane. Equations are then applied along with the definition

$$\gamma_j^2 = k_j^2 - \beta^2 = \frac{2\pi n_{eff}}{\lambda}. \tag{2.40}$$

The inner boundary condition at the axis of radial symmetry ($\rho = 0$) in layer $j = 1$ requires that the fields be finite, resulting in

$$B_1 = 0 \tag{2.41}$$

$$D_1 = 0, \tag{2.42}$$

owing to the fact that $Y_m(\gamma_j\rho)$ diverges as ρ approaches zero. In addition, the outer boundary condition requires that there be no inward propagating wave beyond the outermost layer of the cylindrical structure. An inward propagating wave can be expressed as a Hankel function of the second kind,

$$H_m^{(2)}(\gamma_j\rho) = J_m(\gamma_j\rho) - iY_m(\gamma_j\rho), \tag{2.43}$$

for which the asymptotic limit of large argument has the form [70]

$$H_m^{(2)}(\gamma_j\rho) \propto e^{-i\gamma_j\rho}. \tag{2.44}$$

If we label $j = N$ as the final layer of the cylindrical structure, then in the $j = N+1$ layer, i.e. in the homogeneous medium surrounding the structure, $E_z(\overrightarrow{r})$ and $H_z(\overrightarrow{r})$ can be cast into the form of Eq. 2.43 if

$$B_{N+1} = -iA_{N+1} \tag{2.45}$$

$$D_{N+1} = -iC_{N+1}. \tag{2.46}$$

While strict enforcement of the condition that there be no inward propagating wave in the $(N+1)^{\text{th}}$ layer then requires that $A_{N+1} = C_{N+1} = 0$, when structures of finite extent are considered, we will in fact have $A_{N+1} = C_{N+1} \neq 0$. However, A_{N+1}, C_{N+1}

will have local minima when all other boundary conditions are appropriately satisfied. For example, when analyzing typical radial defect ABR structures, resonant modes confined to the defect layer are found to exist at discrete wavelengths (values of γ_j) for which m takes on integer values, and A_{N+1}, C_{N+1} have local minima. Therefore, assessment of the wavelength-dependent boundary condition in the $(N+1)^{\text{th}}$ layer forms the basis of a numerical search criteria in the design and analysis of the optical modes of ABR microcavities. The results of this numerical analysis are presented in greater detail in Chapter 3.

2.3 Transmission matrix analysis in the basis of propagating waves

The general solution to Eq. 2.14 can also be expressed as a superposition of Hankel functions of the first and second kind [44, 49]. The Hankel functions of the first and second kind are themselves superpositions of Bessel functions of the first and second kind [70], and are given by

$$H_m^{(1)}(x) = J_m(x) + iY_m(x) \tag{2.47}$$

$$H_m^{(2)}(x) = J_m(x) - iY_m(x). \tag{2.48}$$

The Hankel functions are the cylindrical analogues of propagating plane wave solutions $\exp(\pm ix)$ found when solving the Helmholtz equation in the Cartesian coordinate system. For large argument $x >> 1$, the Hankel functions take the form

$$H_m^{(1)}(x) \rightarrow \sqrt{\frac{2}{\pi x}}\left[\cos(x - \frac{m\pi}{2} - \frac{\pi}{4}) + i\sin(x - \frac{m\pi}{2} - \frac{\pi}{4})\right] \propto e^{ix} \tag{2.49}$$

$$H_m^{(2)}(x) \rightarrow \sqrt{\frac{2}{\pi x}}\left[\cos(x - \frac{m\pi}{2} - \frac{\pi}{4}) - i\sin(x - \frac{m\pi}{2} - \frac{\pi}{4})\right] \propto e^{-ix}, \tag{2.50}$$

and thus behave like cylindrical plane waves, propagating radially outward or inward, respectively. Therefore, is possible to write $E_z(\overrightarrow{r})$ and $H_z(\overrightarrow{r})$ within the j^{th} layer of

a general cylindrical structure as a sum of outgoing and incoming waves, as

$$\begin{aligned} E_z(\overrightarrow{r}) &= E_z^+(\overrightarrow{r}) + E_z^-(\overrightarrow{r}) \\ &= \left[\widetilde{A}_j H_m^{(1)}(\gamma_j\rho) + \widetilde{B}_j H_m^{(2)}(\gamma_j\rho)\right] e^{im\theta} \qquad (2.51) \\ H_z(\overrightarrow{r}) &= H_z^+(\overrightarrow{r}) + H_z^-(\overrightarrow{r}) \\ &= \left[\widetilde{C}_j H_m^{(1)}(\gamma_j\rho) + \widetilde{D}_j H_m^{(2)}(\gamma_j\rho)\right] e^{im\theta}. \qquad (2.52) \end{aligned}$$

In the above, the existence of independent TE and TM polarizations has been assumed.

At the interface between the j^{th} and $(j+1)^{\text{th}}$ layers, located at $\rho = R_j$, the tangential field components ($E_z(\overrightarrow{r})$, $H_\theta(\overrightarrow{r})$ for TM, $H_z(\overrightarrow{r})$, $E_\theta(\overrightarrow{r})$ for TE) must be continuous. Using Eqs. 2.19, 2.21, 2.51, 2.52, and applying a similar approach to that developed in Section 2.2, the boundary conditions at the interface can be used to relate the coefficient vectors $\left[\widetilde{A}\ \widetilde{B}\right]_j$ and $\left[\widetilde{C}\ \widetilde{D}\right]_j$ in the j^{th} layer (for TM and TE polarizations, respectively) to those in the $(j+1)^{\text{th}}$ layer. In matrix form, these relationships can be expressed by

$$\begin{aligned} \begin{bmatrix}\widetilde{A}\\ \widetilde{B}\end{bmatrix}_{j+1} &= \left(\widetilde{M}_{j+1}^{TM}\right)^{-1} \widetilde{M}_j^{TM} \begin{bmatrix}\widetilde{A}\\ \widetilde{B}\end{bmatrix}_j = \widetilde{T}_j^{TM} \begin{bmatrix}\widetilde{A}\\ \widetilde{B}\end{bmatrix}_j \qquad (2.53) \\ \begin{bmatrix}\widetilde{C}\\ \widetilde{D}\end{bmatrix}_{j+1} &= \left(\widetilde{M}_{j+1}^{TE}\right)^{-1} \widetilde{M}_j^{TE} \begin{bmatrix}\widetilde{C}\\ \widetilde{D}\end{bmatrix}_j = \widetilde{T}_j^{TE} \begin{bmatrix}\widetilde{C}\\ \widetilde{D}\end{bmatrix}_j, \qquad (2.54) \end{aligned}$$

where

$$\begin{aligned} \widetilde{M}_j^{TM} &= \begin{bmatrix} H_m^{(1)}(\gamma_j R_j) & H_m^{(2)}(\gamma_j R_j) \\ \dfrac{-n_j}{\gamma_j} H_m'^{(1)}(\gamma_j R_j) & \dfrac{-n_j}{\gamma_j} H_m'^{(2)}(\gamma_j R_j) \end{bmatrix} \qquad (2.55) \\ \widetilde{M}_j^{TE} &= \begin{bmatrix} H_m^{(1)}(\gamma_j R_j) & H_m^{(2)}(\gamma_j R_j) \\ \dfrac{1}{\gamma_j} H_m'^{(1)}(\gamma_j R_j) & \dfrac{1}{\gamma_j} H_m'^{(2)}(\gamma_j R_j) \end{bmatrix}. \qquad (2.56) \end{aligned}$$

In Eqs. 2.55 and 2.56, $H_m'^{(1,2)}(\gamma_j R_j)$ are the derivatives of $H_m^{(1,2)}(\gamma_j R_j)$ with respect

to their own argument. At $\rho = 0$ in the first layer ($j = 1$), requiring that the fields be finite gives rise to the boundary condition

$$\widetilde{A}_1 = \widetilde{B}_1 \tag{2.57}$$

$$\widetilde{C}_1 = \widetilde{D}_1. \tag{2.58}$$

Beyond the outer boundary of the structure, in the $j = (N+1)^{\text{th}}$ layer, the requirement that there be no incoming wave takes the form

$$\widetilde{B}_{N+1} = 0 \tag{2.59}$$

$$\widetilde{D}_{N+1} = 0. \tag{2.60}$$

Similarly to the transfer matrix formalism in the standing wave (Bessel function) basis, Eqs. 2.53-2.54 coupled with the boundary conditions in Eqs. 2.57-2.60 allow calculation of the z-component fields within each layer of a general cylindrical structure by "propagating" from the innermost to the outermost layer, or vice-versa.

Furthermore, expressing the fields in terms of a propagating wave basis allows for straightforward computation of the reflectivity r and transmissivity t at a cylindrical dielectric interface, by making use of the transmission matrices $\widetilde{T}_j^{TM}$ and $\widetilde{T}_j^{TE}$ shown in Eqs. 2.53 and 2.54. The transmission matrices for a cylindrical dielectric interface take the general form

$$\widetilde{T}_j^{TM,TE} = \begin{bmatrix} a_m^j & b_m^j \\ b_m^{j*} & a_m^{j*} \end{bmatrix}, \tag{2.61}$$

where a_m^{j*}, b_m^{j*} are the complex conjugates of a_m^j, b_m^j. The transmission matrix elements are given by

$$a_m^j = \frac{i\pi\gamma_{j+1}\rho}{4}\Big[H_m'^{(2)}(\gamma_{j+1}R_j)H_m^{(1)}(\gamma_j R_j) - \frac{\gamma_j}{\gamma_{j+1}}H_m^{(2)}(\gamma_{j+1}R_j)H_m'^{(1)}(\gamma_j R_j)\Big] \tag{2.62}$$

$$b_m^j = \frac{i\pi\gamma_{j+1}\rho}{4}\Big[H_m'^{(2)}(\gamma_{j+1}R_j)H_m^{(2)}(\gamma_j R_j) - \frac{\gamma_j}{\gamma_{j+1}}H_m^{(2)}(\gamma_{j+1}R_j)H_m'^{(2)}(\gamma_j R_j)\Big] \tag{2.63}$$

for TM polarization, and by

$$a_m^j = \frac{i\pi\gamma_{j+1}\rho}{4}\Big[H_m'^{(2)}(\gamma_{j+1}R_j)H_m^{(1)}(\gamma_j R_j) - \tfrac{\gamma_{j+1}}{\gamma_j}H_m^{(2)}(\gamma_{j+1}R_j)H_m'^{(1)}(\gamma_j R_j)\Big] \quad (2.64)$$

$$b_m^j = \frac{i\pi\gamma_{j+1}\rho}{4}\Big[H_m'^{(2)}(\gamma_{j+1}R_j)H_m^{(2)}(\gamma_j R_j) - \tfrac{\gamma_{j+1}}{\gamma_j}H_m^{(2)}(\gamma_{j+1}R_j)H_m'^{(2)}(\gamma_j R_j)\Big] \quad (2.65)$$

for TE polarization.

For an outgoing (incoming) cylindrical wave incident upon the interface between the j^{th} and $(j+1)^{\text{th}}$ layers, the reflectivity r_o (r_i), transmissivity t_o (t_i), power reflection coefficient R_o (R_i), and power transmission coefficient T_o (T_i) are given by Eqs. 2.66-2.71, with the help of Fig. 2.3. Note that $\phi^{+,-} = \{E_z^{+,-}(\overrightarrow{r}), H_z^{+,-}(\overrightarrow{r})\}$.

$$r_o = \left.\frac{\phi_j^-}{\phi_j^+}\right|_{\phi_{j+1}^-=0} = -\frac{b_m^{j*}}{a_m^{j*}} \quad (2.66)$$

$$t_o = \left.\frac{\phi_{j+1}^+}{\phi_j^+}\right|_{\phi_{j+1}^-=0} = -\frac{\det\left|\widetilde{T}_j^{TM,TE}\right|}{a_m^{j*}} \quad (2.67)$$

$$r_i = \left.\frac{\phi_{j+1}^+}{\phi_{j+1}^-}\right|_{\phi_j^+=0} = \frac{b_m^j}{a_m^{j*}} \quad (2.68)$$

$$t_i = \left.\frac{\phi_j^-}{\phi_{j+1}^-}\right|_{\phi_j^+=0} = \frac{1}{a_m^{j*}} \quad (2.69)$$

$$R_{o,i} = |r_{o,i}|^2 \quad (2.70)$$

$$T_{o,i} = |t_{o,i}|^2 \quad (2.71)$$

The determinants of the transmission matrices are given by

$$\det\left|\widetilde{T}_j^{TM}\right| = 1 \quad (2.72)$$

$$\det\left|\widetilde{T}_j^{TE}\right| = \left(\frac{n_{j+1}}{n_j}\right)^2. \quad (2.73)$$

The transmission matrix formalism is particularly useful for analyzing reflection

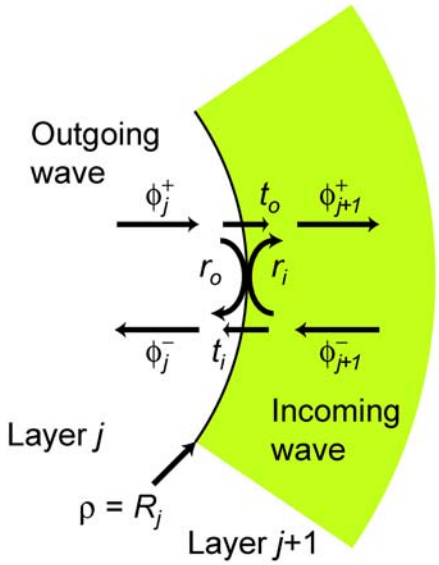

Figure 2.3: Illustration of the reflectivity $r_0(r_i)$ and transmissivity $t_0\,(t_i)$ coefficients at a cylindrical interface, for outgoing (incoming) cylindrical waves. The fields $E_z^{+,-}(\overrightarrow{r})$, $H_z^{+,-}(\overrightarrow{r})$ are represented by $\phi^{+,-}$.

from and transmission through more complex multi-layered cylindrical structures, such as Bragg reflectors or ABR defect resonators. A series of layers with arbitrary thickness and refractive index may be modeled by a single transmission matrix, formed by multiplication of the transmission matrices representing each individual layer, as

$$\widetilde{T}_{total}^{TE,TM} = \widetilde{T}_N^{TE,TM}\widetilde{T}_{N-1}^{TE,TM}...\widetilde{T}_2^{TE,TM}\widetilde{T}_1^{TE,TM}. \tag{2.74}$$

Composite transmission matrices calculated in this manner will be applied to evaluate the reflection coefficients of cylindrical Bragg reflectors in Chapter 3.

Chapter 3

Numerical design and modeling of ABR devices

3.1 Introduction

In Chapter 2, a transfer matrix approach for evaluating the TM and TE modes of a general cylindrically symmetric multi-layer structure was developed. Given *a priori* the refractive index and width of each layer, and by requiring that the fields be real and finite on the axis of symmetry at $\rho = 0$, application of the transfer matrices given by Eqs. 2.38-2.39 will yield the TM and TE fields in each layer, as per Eq. 2.37. However, when engaging in the practical design of efficient cylindrical Bragg reflectors and ABR defect resonators, we may initially know only the refractive index of the various dielectric media we have at our disposal for the high and low index layers. It remains to determine the appropriate radii R_j at which to place the interfaces between the j^{th} and $(j+1)^{\text{th}}$ layers, and thus, determine the thickness of each layer. This chapter will outline a set of design rules for placing these interfaces, and apply these rules toward generating optimal cylindrical Bragg reflectors and radial defect ABR microcavities. Comparisons between Bragg gratings designed in cylindrical and Cartesian coordinate systems will be made, illustrating the chirped structure of the ideal cylindrical Bragg reflector. Numerically evaluated designs for several types of cylindrical grating structures will be presented, and the properties of guided ABR optical modes will be discussed.

3.2 Design of radial defect ABR microcavities

3.2.1 Comparison of cylindrical and linear Bragg reflectors

The criteria for determining the thickness of each dielectric layer within a cylindrical Bragg reflector can be made in analogy to the criteria for a one-dimensional (1D) Bragg grating in Cartesian coordinates. In order to ensure that a linear multi-layer dielectric mirror has a large reflection coefficient, the dielectric interfaces must be placed such that the partial reflections of an incident wave from each successive layer all add up in phase with one another [65], as illustrated in Fig. 3.1(a). This requires

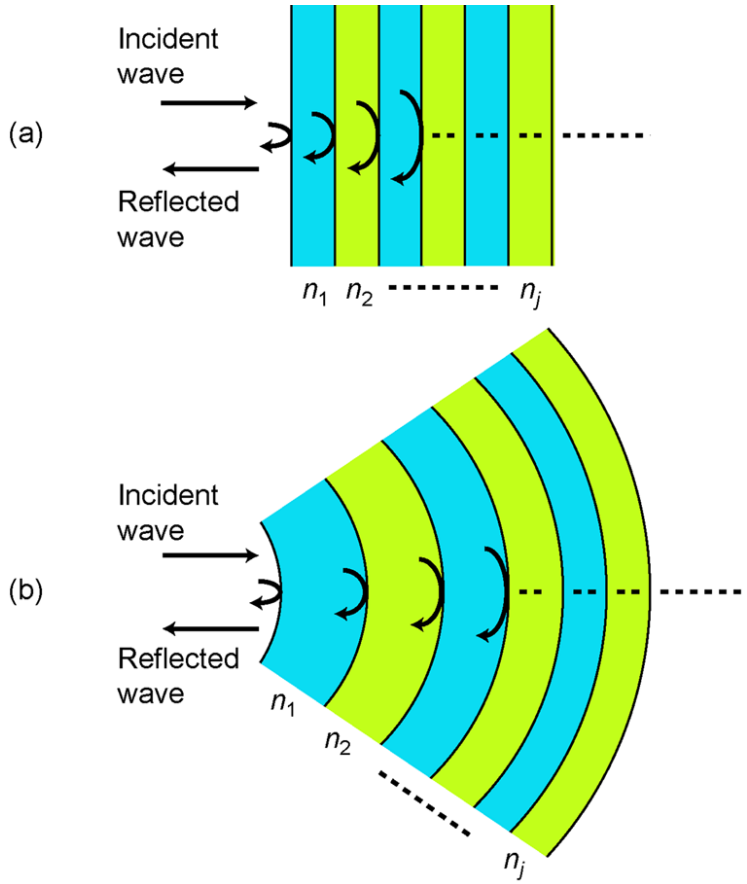

Figure 3.1: Schematics of multi-layer Bragg reflectors, showing partial reflections of an incident wave from each dielectric interface. (a) 1D linear Bragg grating. (b) Cylindrical Bragg grating.

that the total phase accumulated by the wave upon propagating through each layer

be an odd multiple of $\pi/2$. Stated mathematically,

$$\int_{layer} k_\perp dx = (2l+1)\frac{\pi}{2}, \tag{3.1}$$

where $k_\perp$ is the projection of the wavevector of the incident wave along the axis of the 1D Bragg reflector, $l = 0, 1, 2, \ldots$, and $l+1$ is the reflection order of the Bragg layer. The integration is intended to be carried out over the coordinate x between two successive dielectric interfaces. For simplicity, let us consider normal incidence upon the grating. For the Cartesian coordinate case, the wave incident upon the 1D linear Bragg reflector can be expressed as a plane wave, having the form $\exp(ik_\perp x)$, where the wavenumber $k_\perp = 2\pi n_j/\lambda_0$ is a constant within a given layer of refractive index n_j. Thus, the width w_j of the j^{th} layer is given by

$$w_j^{layer} = (2l+1)\frac{\lambda_0}{4n_j}, \tag{3.2}$$

i.e., the layer width must be an odd multiple of a quarter-wavelength in the material. The fact that the spatial period of the plane wave's oscillation is constant regardless of the longitudinal position x within a given layer therefore gives rise to the typical periodic 1D Bragg reflector design, as shown in Fig. 3.1(a).

For the case of a cylindrical Bragg reflector, the incident waves we wish to consider are no longer plane waves, but cylindrical waves. The partial reflections from each cylindrical dielectric interface must also add up in phase, and the condition of Eq. 3.1 holds equally well, where $k_\perp$ and dx are replaced by k_ρ and $d\rho$, respectively. However, in contrast to the case in Cartesian coordinates, k_ρ is not constant within a given layer of index n_j, but depends upon the radius ρ, due to the character of the Bessel function solutions of the Helmholtz equation in cylindrical coordinates. To illustrate, a comparison of the spatial oscillation of the Bessel function $J_4(x)$ with a sinusoidal function $\cos(x + 7\pi/4)$ is made in Fig. 3.2. For small argument x, the spatial period of the Bessel function is significantly larger than that of the sinusoidal function. However, at larger values of x, the spatial period decreases, and approaches

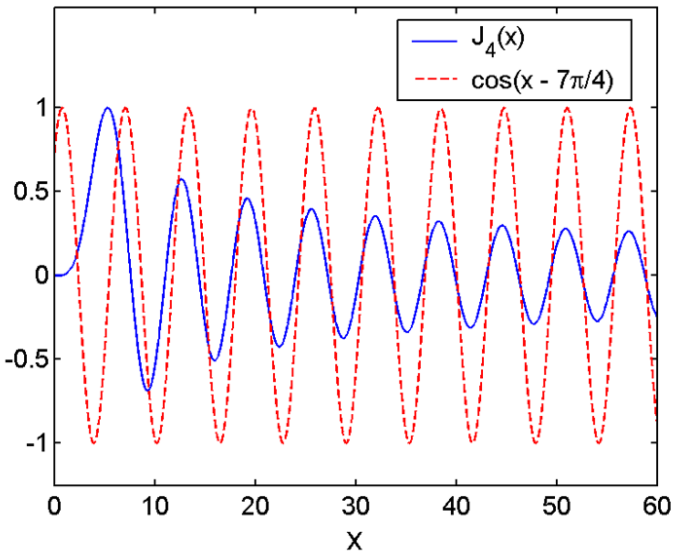

Figure 3.2: Comparison of the Bessel function $J_4(x)$ with its asymptotic sinusoidal form. The spatial period of the Bessel function is larger than that of the sinusoid for small argument x, and asymptotically approaches a constant for large argument.

a constant value. For large argument $x >> 1$, the Bessel functions of the first and second kinds have asymptotic forms [70] given by

$$J_m(x) \rightarrow \sqrt{\frac{2}{\pi x}} \cos\left(x - \frac{m\pi}{2} - \frac{\pi}{4}\right) \tag{3.3}$$

$$Y_m(x) \rightarrow \sqrt{\frac{2}{\pi x}} \sin\left(x - \frac{m\pi}{2} - \frac{\pi}{4}\right). \tag{3.4}$$

The sinusoid in Fig. 3.2 was plotted with the same phase as the asymptotic form of the $J_4(x)$ Bessel function, and the zero-crossings of both functions intersect at larger radii.

As will be discussed in greater detail below, the conditions for generating an optimal cylindrical Bragg reflector require that the interfaces between each dielectric layer be placed at the zeros or extrema of electromagnetic field profile. Therefore, because the fields within each layer are described by a superposition of Bessel functions, as shown in Eqs. 2.31-2.32, it follows that the ideal layer width will not be a uniform quarter-wavelength throughout the structure as in the Cartesian case, but will be

chirped, being thicker at small radii, and converging to a constant thickness at large radii. We can, however, consider the layers in a cylindrical Bragg reflector as being an "effective" quarter-wavelength wide, as defined by phase accumulation according to Eq. 3.1. The schematic shown in Fig. 3.1(b) clearly illustrates the chirped nature of the cylindrical Bragg grating.

3.2.2 Grating defect cavities

Bragg gratings with high reflectivity can be used to define optical resonators, in much the same way as two partially reflecting mirrors can be used to form a Fabry-Perot cavity [53]. Introducing a small separation w^{defect} between two 1D Bragg reflectors, or equivalently, creating a phase defect within a single Bragg reflector, can lead confinement of resonant modes within this defect. Such defect cavities have been used in various microresonator laser configurations, including vertical cavity surface emitting lasers (VCSELs) [61], distributed Bragg reflector (DBR) lasers [71], and quarter-wavelength shifted distributed feedback (DFB) lasers [72]. Waves traversing the cavity must acquire a net round-trip phase equal to an integer multiple of 2π in order to be resonant, i.e.

$$2\int_{defect} k_{\perp} dx + 2\phi_{mirror} = 2l\pi, \tag{3.5}$$

where ϕ_{mirror} is the phase of the reflection from the mirror, and $l = 1, 2, 3, ...$ is the defect order. The integration is carried out over the coordinate x between the two mirrors. Assuming that $|\phi_{mirror}| = \pi$ or 0, the resonance condition can be written as

$$\int k_{\perp} dx = l\pi. \tag{3.6}$$

In a 1D linear Bragg reflector where $k_{\perp}$ is a constant function of x, Eq. 3.6 states that the cavity must be an integer number of half-wavelengths wide, i.e.,

$$w^{defect} = l\frac{\lambda_0}{2n_{defect}}. \tag{3.7}$$

As discussed above, for the cylindrical Bragg reflector, $k_\perp = k_\rho$ is a function of ρ. The defect cavity width will therefore depend upon its radial position within the Bragg reflector, and this width can be designed as an integer number of "effective" half-wavelengths.

3.2.3 Design rules for placement of dielectric interfaces in optimal Bragg reflectors

If we wish to design, for example, an ABR resonator similar to that shown in Fig. 2.2, to support a mode with concentrated amplitude within the azimuthal defect layer and exponentially decaying amplitude in both the internal and external gratings, it remains to determine the appropriate radii R_j at which to place the interfaces between the j^{th} and $(j+1)^{\text{th}}$ layers. This type of ABR defect mode requires that the field increases exponentially throughout the interval $0 < \rho < R_{defect}$ (internal Bragg grating), and decreases exponentially within the interval $R_{defect} < \rho < R_N$ (external Bragg grating), where R_{defect} and R_N are taken to be the radii of the azimuthal defect and the last interface, respectively. The conditions for optimal placement of the interface between dielectric layers having refractive indexes n_j and n_{j+1} were derived by Yeh et al. [62], in the context of Bragg fiber. These conditions were found by considering the maximization/minimization of the electromagnetic flux flowing radially outward within the outermost layer of the Bragg fiber's cladding. It was shown that in order to produce the most efficient exponential increase or decrease of the fields, and thus the outgoing flux, the interfaces should be placed at radii R_j corresponding to the zeros or extrema of the z-component fields within the cylindrical structure, according to the following set of rules.

For TE modes and increasing field amplitude, the interfaces should be placed at:

$$H_z(R_j) = 0 \text{ for } n_j < n_{j+1} \tag{3.8}$$

$$H_z'(R_j) = 0 \text{ for } n_j > n_{j+1}. \tag{3.9}$$

For TE modes and decreasing field amplitude, the interfaces should be placed at:

$$H_z'(R_j) = 0 \text{ for } n_j < n_{j+1} \tag{3.10}$$

$$H_z(R_j) = 0 \text{ for } n_j > n_{j+1.} \tag{3.11}$$

For TM modes and increasing field amplitude, the interfaces should be placed at:

$$E_z'(R_j) = 0 \text{ for } n_j < n_{j+1} \tag{3.12}$$

$$E_z(R_j) = 0 \text{ for } n_j > n_{j+1}. \tag{3.13}$$

For TM modes and decreasing field amplitude, the interfaces should be placed at:

$$E_z(R_j) = 0 \text{ for } n_j < n_{j+1} \tag{3.14}$$

$$E_z'(R_j) = 0 \text{ for } n_j > n_{j+1}. \tag{3.15}$$

In the above, it is understood that the layers j, $j+1$, $j+2$, ... are labeled in order of increasing radius ρ. These conditions are equivalent to those found for Bragg reflectors in Cartesian coordinates.

3.2.4 First-order cylindrical gratings

As an example, the procedure followed to design an ABR defect resonator with first-order Bragg gratings is outlined below, in the specific case of TE polarized modes. For a given choice of the azimuthal number m and the wavelength λ_0, the width of each layer in the cylindrical structure and the TE field components can be found simultaneously using the Bessel function transfer matrix formalism described in Section 2.2. Beginning in layer $j = 1$, the boundary condition requiring finiteness of the fields at $\rho = 0$ (Eq. 2.42) dictates that the vector of constants describing the $H_z(\rho)$ field be given by

$$\begin{bmatrix} C \\ D \end{bmatrix}_1 = \begin{bmatrix} 1 \\ 0 \end{bmatrix}_1, \tag{3.16}$$

where we have taken $C_1 = 1$ for simplicity. Given a numerical value for this vector, and knowing $\gamma_1 = 2\pi n_1/\lambda_0$, the radial dependence of the field $H_z(\rho)$ within layer $j = 1$ is fixed. The field, along with the radial positions of its zeros and extrema, can be found using a numerical routine for evaluating Bessel functions, such as those included in Matlab. Since we desire to design an optical mode having a concentration of intensity at the position of the annular defect within the cylindrical Bragg reflector, the placement of the first dielectric interface, located at a radius $\rho = R_1$, is dictated by the design rules for increasing TE field amplitude, given by Eqs. 3.8-3.9. After the radial position of the first dielectric interface is known, the refractive index of the dielectric is changed. The transfer matrix T_1 enforcing the continuity of the tangential field components at the interface is then used in order to calculate the vector of constants in the $j = 2$ layer, as per Eqs. 2.37 and 2.39. After numerical evaluation of the field's zeros and/or extrema within the $j = 2$ layer, the second dielectric interface is appropriately placed, and so on. The above steps are repeated for the desired number of periods of the inner Bragg reflector. The annular defect is then introduced. The inner defect radius is again chosen according to the design rules for increasing field, however the outer radius is chosen according to the design rules for decreasing field, given by Eqs. 3.10-3.11. Finally, within the outer Bragg reflector, the radial positions of the interfaces are chosen according to decreasing field. The number of periods in the outer Bragg reflector is chosen to achieve sufficient damping of the field at large radii, in order to produce a low-loss radially confined mode.

In order to illustrate the results of this design approach, we consider the particular example of a TE polarized defect mode designed to have an azimuthal number $m = 7$ at a wavelength $\lambda_0 = 1.55$ μm, within an ABR structure having high index layers with $n = 2.8$, and low index layers with $n = 1.56$. These values of the refractive index and polarization have been chosen for their relevance toward the semiconductor ABR devices which will be discussed in greater detail in Chapters 4 and 5. The normalized $H_z(\rho)$ mode profile is plotted as a function of the radial coordinate in Fig. 3.3(a), superimposed with the designed refractive index profile. For the case shown, the $j = 1$ layer was taken to have low index, and the defect layer was taken to have high

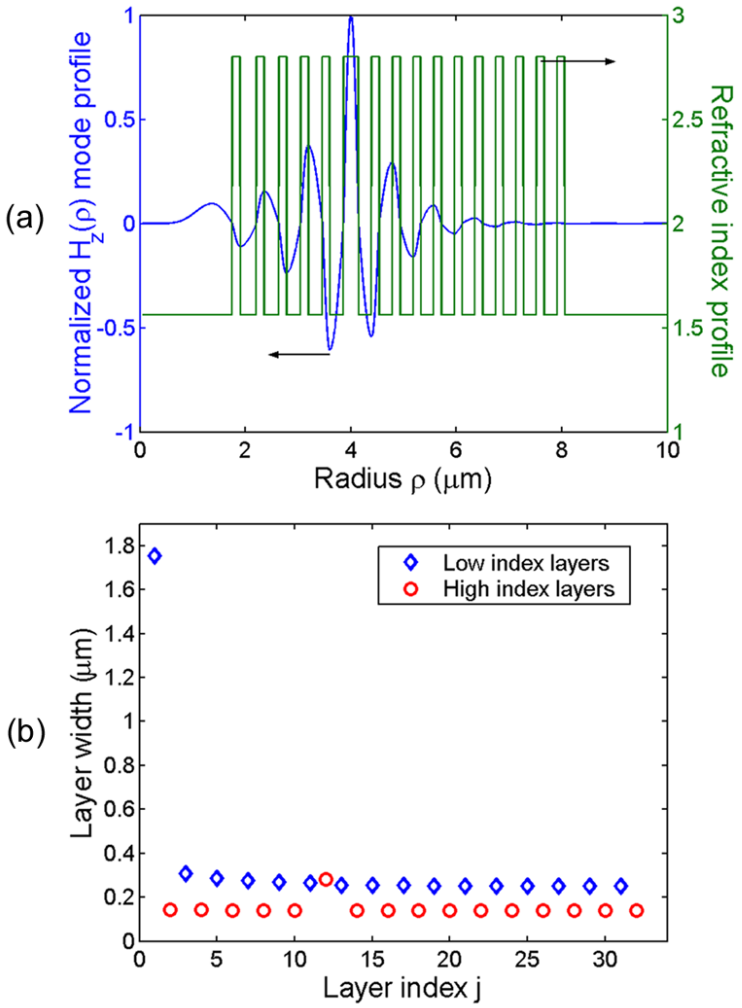

Figure 3.3: (a) TE profile $H_z(\rho)$ of an ABR defect mode having $m = 7$, $\lambda_0 = 1.55$ μm, first-order high index layers with $n = 2.8$, and first-order low index layers with $n = 1.56$. The radial refractive index profile is superimposed to illustrate the placement of the dielectric interfaces with respect to the zeros and extrema of the field. (b) Width of the low and high index layers versus layer index. The sixth high index layer is the defect layer, and has a width approximately twice that of the high index layers within the Bragg reflectors.

index. The defect is the sixth high index layer going radially outward from $\rho = 0$. The inner and outer Bragg reflectors consist of 5 and 10 periods, respectively. The field has peak amplitude within the defect layer, and decays exponentially within a relatively few number of periods of the Bragg reflectors on either side, due to the large refractive index contrast. Note that within each reflector layer, the field completes an "effective" quarter wavelength oscillation, i.e. the width of each layer is equivalent to the distance between successive zeros and extrema of the field. Furthermore, the defect layer spans the distance between two successive zeros of the field, an "effective" half wavelength. The width of each low and high index layer is plotted in Fig. 3.3(b). The layer width is seen to decrease as a function of radius, in particular for the low index layers, and approaches a constant value at large radii, equivalent to the conventional "quarter-wavelength" thickness of a 1D Bragg reflector.

It is worthwhile to note that in addition to supporting modes with peak intensity within a high index defect, the Bragg confinement mechanism also admits the possibility of guiding light within a low index defect, a scenario impossible for total-internal-reflection based devices [50].

The procedure followed for the design of ABR structures for TM polarized modes is identical to that outlined above, but makes use of the appropriate transfer matrix in Eq. 2.38 and the design rules in Eqs. 3.12-3.15.

3.2.5 Higher-order/mixed-order cylindrical gratings

Rather than placing the dielectric interfaces at consecutive zeros/extrema of the radial field profile, as was done above for the first-order grating design, an alternative design procedure would be to make use of higher order Bragg reflection by permitting the field to cycle through a larger odd multiple of "quarter-wavelengths" before placing the interface. Furthermore, the high and low index layers do not need to be of the same Bragg order. Thus, a mixed-order grating, with higher-order high-index layers and first-order low-index layers, could be employed to ease fabrication tolerances. For example, in the case of the high contrast first-order ABR structure illustrated in Fig.

3.3, the high index layers are very narrow, being approximately 140 nm wide, while the low index layers are significantly wider at approximately 250 nm. By comparison, a mixed-order grating design having second-order (three "quarter-wavelengths" wide) high index layers, and first-order low index layers, would be significantly easier to fabricate.

Such a structure, again having 5 and 10 period inner and outer Bragg reflectors, and the associated $m = 7$ TE mode profile resonant at $\lambda_0 = 1.55$ μm, are plotted in Fig. 3.4(a). Comparison with the mode profile of the ABR with first-order gratings in Fig. 3.3(a) shows that while the field is still localized at the position of the defect layer, it decays more slowly in the radial direction away from the defect. Thus, higher-order designs bear the consequence that the Bragg mirrors will in general require a larger number of periods in order to achieve adequate radial optical confinement. In addition, even for the same number of periods in the inner and outer Bragg reflectors, and the same m number, the design with second order high index layers also forces the defect layer to larger radii, resulting in an increase in the size of the resonator, and a decrease in the free spectral range (FSR), as will be discussed below. Figure 3.4(b) illustrates that the high index layers are now wider than the low index layers, and will consequently be easier to fabricate.

Furthermore, Fig. 3.4(a) illustrates that the transverse mode profile undergoes one complete oscillation between each quasi-period of the grating, and therefore, light scattered from adjacent quasi-periods will have equal phase modulo 2π. The particular mixed-order grating illustrated then acts as a second-order grating design, which not only couples counter-propagating radial waves, but also induces coupling of radially propagating waves into the direction normal to the plane of the ABR device, i.e the z-direction [47]. These properties of second-order gratings are illustrated in Fig. 3.5. The Fourier spectrum of a square wave second-order grating has components at the harmonics of the fundamental grating wavenumber k_G, given by

$$k_G = 2\pi/\Lambda = 2\pi/\lambda_\rho, \tag{3.17}$$

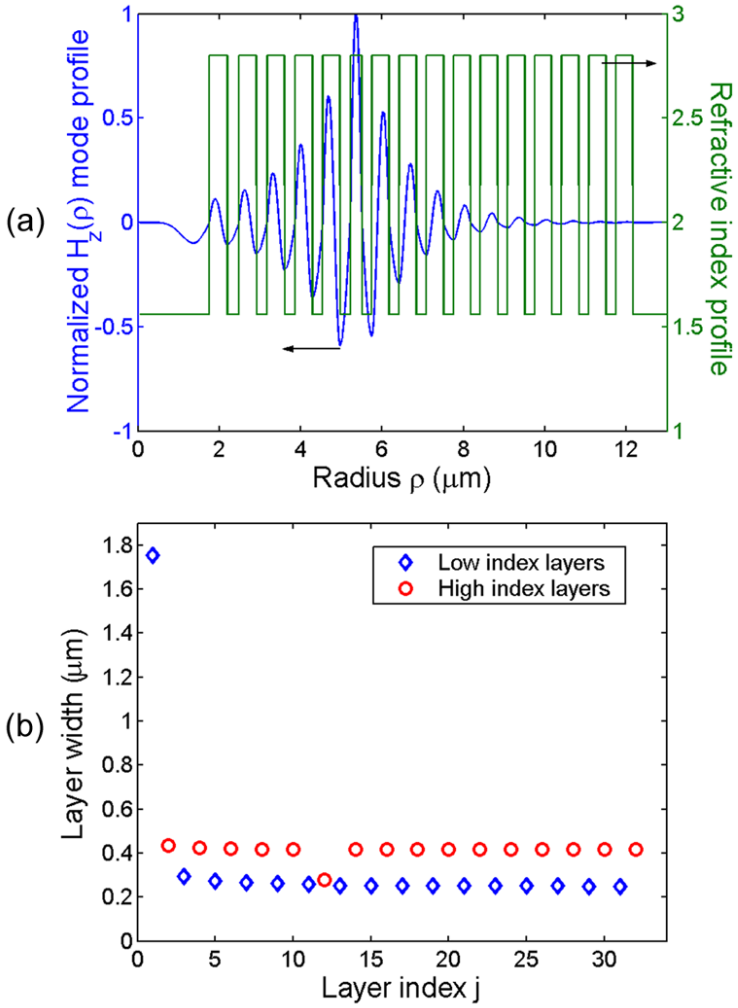

Figure 3.4: (a) TE profile $H_z(\rho)$ of an ABR defect mode having $m = 7$, $\lambda_0 = 1.55$ μm, second-order high index layers with $n = 2.8$, and first-order low index layers with $n = 1.56$. The radial refractive index profile is superimposed to illustrate the placement of the dielectric interfaces with respect to the zeros and extrema of the field. (b) Width of the low and high index layers versus layer index. The sixth high index layer is the defect layer, and has a width smaller than that of the high index layers within the Bragg reflectors.

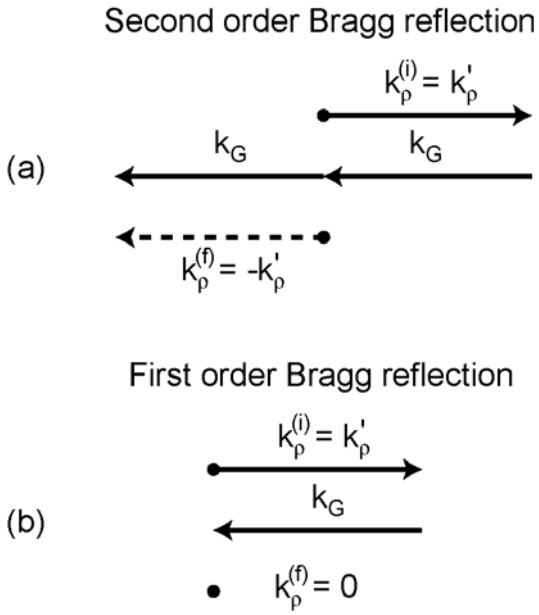

Figure 3.5: Illustration of radial wavevector components participating in resonant scattering from a second-order Bragg grating. (a) Coupling of counter-propagating radial waves via the second-order Bragg reflection. (b) Cancellation of radial wavevector component by the first-order Bragg reflection, inducing coupling to vertically propagating waves.

where Λ is the "period" of the radial grating, and λ_ρ is the "wavelength" of the oscillations in the mode profile along the radial direction. Considering a wave incident upon the grating with radial wavenumber $k_\rho^{(i)} = k'_\rho = 2\pi/\lambda_\rho$, the second-order Bragg reflection (second harmonic) gives rise to the back-reflected wave with $k_\rho^{(f)} = -k'_\rho$ desired for in-plane optical confinement, as shown in Fig. 3.5(a). Addition of the radial wavenumber components for second-order Bragg reflection can be expressed as

$$k_\rho^{(f)} = -k'_\rho = k'_\rho - 2k_G = k_\rho^{(i)} - 2k_G. \tag{3.18}$$

However, the first Fourier harmonic scatters incident waves with $k_\rho^{(i)} = k'_\rho$ into waves with no radial component, as given by the sum

$$k_\rho^{(f)} = 0 = k'_\rho - k_G = k_\rho^{(i)} - k_G. \tag{3.19}$$

Therefore, the first-order Bragg reflection from a second-order grating can phase-match radially propagating waves to vertically propagating plane waves. This property of second order gratings has been exploited previously to demonstrate vertical output coupling from in-plane DBR and DFB lasers in Cartesian coordinates [73–75], and will be discussed further in the context of ABR lasers in Chapter 5.

3.2.6 Reflection coefficients for cylindrical Bragg mirrors

The design of ABR defect resonators requires that we choose the combination of an appropriate number of periods for the inner and outer Bragg reflectors, as well as a sufficient refractive index contrast between the low and high index layers, in order to ensure that the optical mode can propagate azimuthally within the defect with relatively low in-plane losses. Leakage of power out of the defect mode can be minimized, and modal quality factor Q maximized, by design of efficient cylindrical Bragg mirrors with large reflectivity. While infinite Bragg gratings can in theory have a reflection coefficient of unity, practical designs are limited to a fairly small number of periods, and thus, an estimation of the reflection coefficient from finite gratings is

useful.

The reflection coefficients $R^{TE,TM}$ for TE and TM polarized cylindrical waves incident upon annular Bragg reflectors can be computed using the Hankel function transmission matrix formalism developed in Section 2.3. To illustrate, a series of reflectors with a number of low/high index periods varying from 1 to 10 was constructed according to the design rules described above. The design procedure was optimized for TE waves having $m = 7$ and a wavelength of $\lambda_0 = 1.55$ μm. The high index layers had second-order width and $n = 2$, and the low index layers had first-order width and $n = 1.5$. For each reflector, the innermost and outermost layers were taken to have $n = 1.5$.

The dependence of the TM and TE reflection coefficients upon the number of grating periods, evaluated at $\lambda_0 = 1.55$ μm for $m = 7$, is plotted in Fig. 3.6(a). As the number of periods is increased, constructive reflection from the multiple dielectric interfaces in the reflector leads to a rapid increase in the reflection coefficient. For 10 periods, $R^{TM} = 0.993$ and $R^{TE} = 0.978$. In general, TE polarized waves are reflected less strongly than TM waves. Figure 3.6(b) illustrates the spectral dependence of the TM and TE reflection coefficients, for a grating with 10 periods and $m = 7$. Several dominant reflection lobes are evident, with oscillatory reflection within several adjacent side-lobes. The main lobes near 1.55 μm and 1.05 μm are the second (nominal design) and third reflection orders of the grating. As in the case of linear Bragg gratings, the side-lobes are due to the finite extent of the grating, and can be damped by increasing the number of grating periods, or by an appropriate apodization scheme [65, 76]. In addition to having a slightly smaller peak reflection coefficient, the full-width-at-half-maximum (FWHM) bandwidth of the TE second-order reflection lobe is smaller than that for TM polarization.

As the refractive index contrast between the low and high index layers is increased, the number of periods required to achieve the same reflection coefficient decreases, and the bandwidth of the high reflection lobes increases. This behavior is similar to that found for Bragg reflectors in Cartesian coordinates. The magnitude of the reflection coefficients and shape of the reflection spectra for azimuthal numbers $m \neq 7$

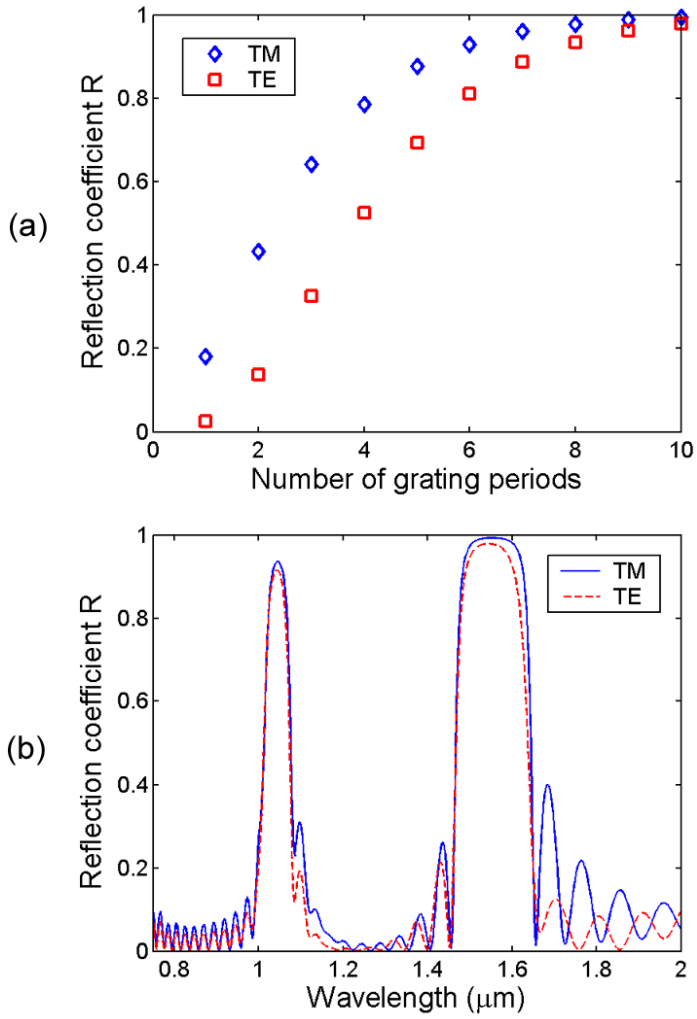

Figure 3.6: (a) Reflection coefficient R versus number of grating periods, evaluated at $\lambda_0 = 1.55$ μm and azimuthal number $m = 7$. (b) Spectral dependence of R for grating with 10 periods. High reflection lobes near 1.55 μm and 1.05 μm are the second and third reflection orders, respectively.

are found to be very similar to that shown in Fig. 3.6, particularly for reflectors with more than one or two periods. Furthermore, the reflection behavior of cylindrical gratings is in general the same regardless whether one considers outgoing or incoming cylindrical waves.

3.2.7 Dispersion of ABR defect modes

Once the radial refractive index profile of a given ABR defect resonator has been fixed for a chosen design wavelength λ_0 and azimuthal number m, the transfer matrix approach of Section 2.2 can be applied to numerically evaluate the wavelengths and m numbers of any additional modes that may be supported by the structure. These additional resonant modes exist at wavelengths for which the boundary condition that there be no inward propagating wave within the outermost layer is satisfied, as given by Eqs. 2.45-2.46. Knowing the m numbers and resonant wavelengths, the modal field profiles may then be determined.

Figure 3.7(a) plots the dispersion curve of the TE defect modes within the first-order ABR structure of Fig. 3.3. The resonant wavelength increases as the azimuthal number m decreases. The free spectral range (FSR) is approximately 11 nm near $\lambda_0 = 1.55$ μm, and increases as the wavelength becomes shorter. The $H_z(\rho)$ radial field profiles for several resonant modes near 1.55 μm are superimposed against one another in Fig. 3.7(b). All modes demonstrate a peak within the defect layer of the ABR structure, and possess very similar profiles within the inner and outer Bragg reflectors. The radial field profile is thus reasonably independent of wavelength, being determined primarily by the spatial period of the refractive index profile of the ABR.

The dispersion curve and several TE radial mode profiles belonging to the second-order ABR structure of Fig. 3.4 are plotted in Fig. 3.8. In terms of the dispersion curve, the primary difference between the first and second-order ABR devices is the smaller FSR of approximately 4 nm near 1.55 μm. As mentioned above, this is due to the larger defect radius of the second-order device. The radial mode profiles of the

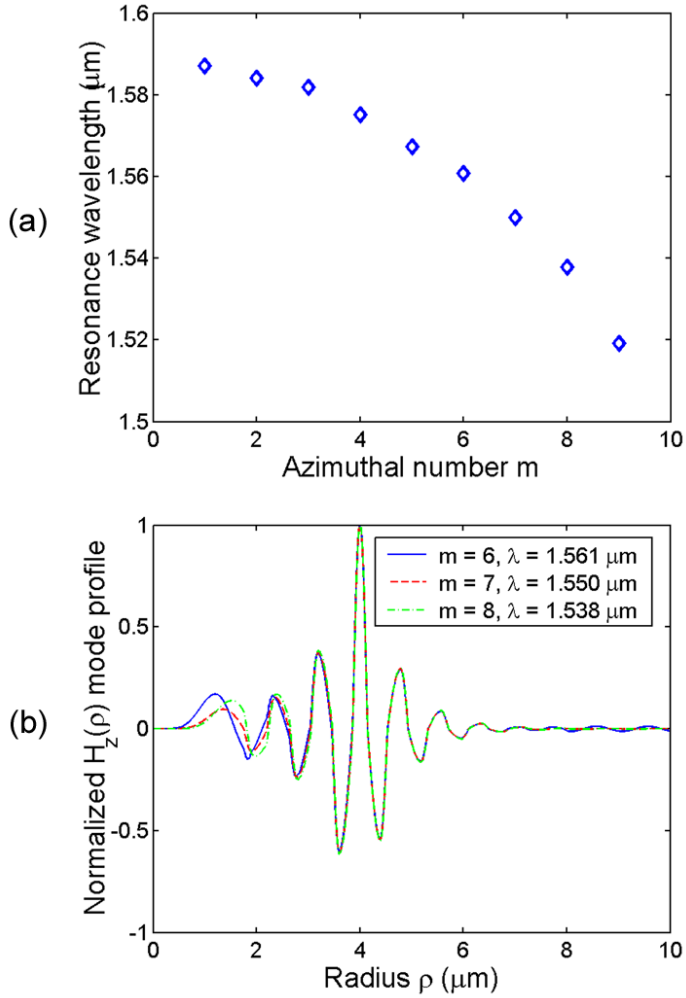

Figure 3.7: (a) Dispersion of TE defect modes with varying azimuthal number m, for the first-order ABR structure of Fig. 3.3. (b) Normalized field profile $H_z(\rho)$ for $m = 6, 7, 8$. Refractive index profile not shown for clarity.

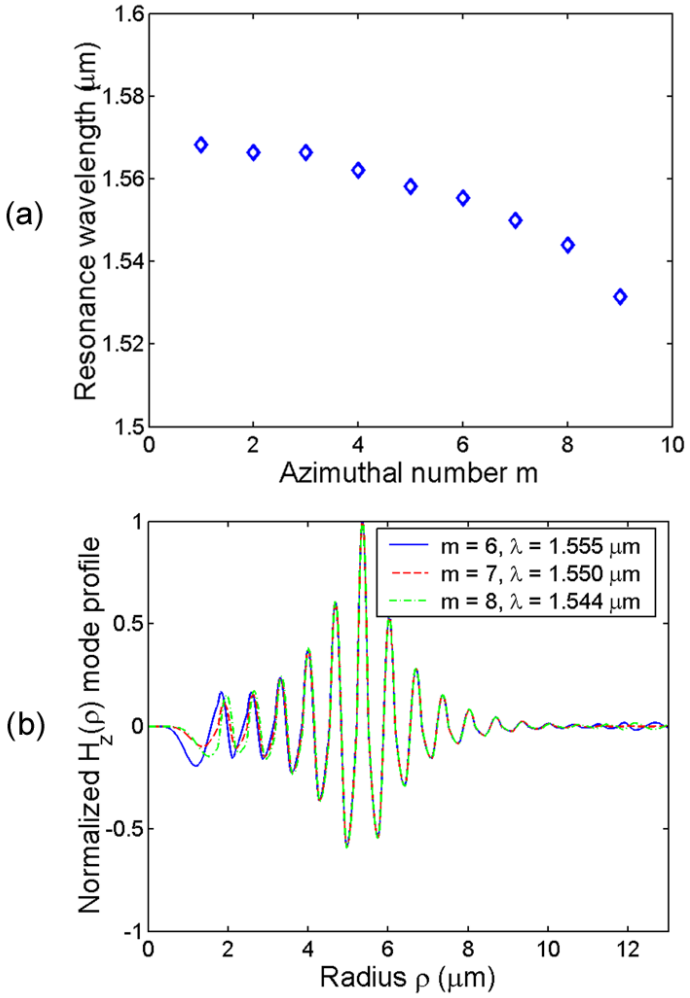

Figure 3.8: (a) Dispersion of TE defect modes with varying azimuthal number m, for the second-order ABR structure of Fig. 3.4. (b) Normalized field profile $H_z(\rho)$ for $m = 6, 7, 8$. Refractive index profile not shown for clarity.

second-order ABR again show little variation with m number and wavelength, and maintain a strong peak within the defect layer.

Chapter 4

Fabrication of InGaAsP ABR microcavities using polymer epitaxial transfer

4.1 Introduction

This chapter describes a versatile process for the fabrication of ABR devices, employing a thin semiconductor membrane for out-of-plane optical confinement by index guiding. The semiconductor substrate used is based upon the InGaAsP-InP material system, selected for its capacity as a light emitter at telecommunications wavelengths near 1.55 μm. The ABR fabrication procedure involves patterning and epitaxial transfer of a single-mode membrane to a transfer substrate, using a polymer adhesive for bonding. This method simultaneously ensures the mechanical integrity of the ABR concentric ring structure, as well as achieving the desired vertical optical confinement. The various ABR geometries discussed in subsequent chapters have all been fabricated by the methods outlined in this chapter, unless stated otherwise.

4.2 Practical structures for optical confinement along the z-axis

The transfer matrix formalism developed in Chapter 2 presents a means of analyzing the optical modes of a generalized axisymmetric cylindrical multi-layer dielectric

structure. Since we wish to consider modes which propagate azimuthally around the cylindrical structure rather than down its axis, we made the assumption that the axial (z) component of the propagation constant was zero, i.e., $\beta = 0$. This assumption intrinsically implies that the dielectric structure has translational invariance along the z-axis. Therefore, in order to have experimental access to the optical modes of devices such as the radial defect ABR microcavities discussed in Chapter 3, we are at first glance faced with the challenge of fabricating a 2D structure having extremely small in-plane dimensions and infinite extent along the z-axis, or at the very least, an extent much larger than the wavelength of interest (quasi-2D). While it may be possible to fabricate such a geometry within a configuration such as an optical fiber, i.e., Bragg/Omniguide fiber [62,77], we are then restricted to materials which are workable by extrusion. Materials in this class can include various amorphous substances, such as glasses and optical polymers. However, if we wish to make use of the desirable optical and electronic properties of semiconductors, such as their large optical gain and high refractive index, we are limited to the techniques of planar wafer processing.

Practically speaking, the fabrication of semiconductor structures with large aspect ratio, i.e. the ratio of the structure's extent along the z-axis to the critical in-plane dimension, becomes extremely difficult. Typical limits on the maximum aspect ratio achievable are on the order of 10:1 - 20:1 [78, 79], with certain exceptions depending upon the material system used [80]. Therefore, 2D or quasi-2D structures are not practically viable, and a dielectric structure providing optical confinement in three dimensions must be considered. While the in-plane optical confinement in ABR devices is provided by reflection from the annular Bragg mirrors, a means for achieving out-of-plane confinement is required.

A similar issue has been addressed during the early theoretical and experimental development of 2D photonic crystals (PCs) [81, 82] and PC defect cavities [83], and has led to the use of air-clad suspended membrane structures, such as the one shown in Fig. 4.1. In these structures, a thin dielectric membrane, most often a high index semiconductor, is perforated with a periodic lattice of holes to generate an optical bandgap for light propagating within the plane of the membrane. Creation of a lattice

defect by removing or changing the size of a single hole (or several holes) can result in trapping of light at the defect site, where in-plane optical confinement is provided by the photonic bandgap. The substrate material beneath the membrane is then selectively removed, often by wet chemical etching, to create an air gap [84–86]. Out-

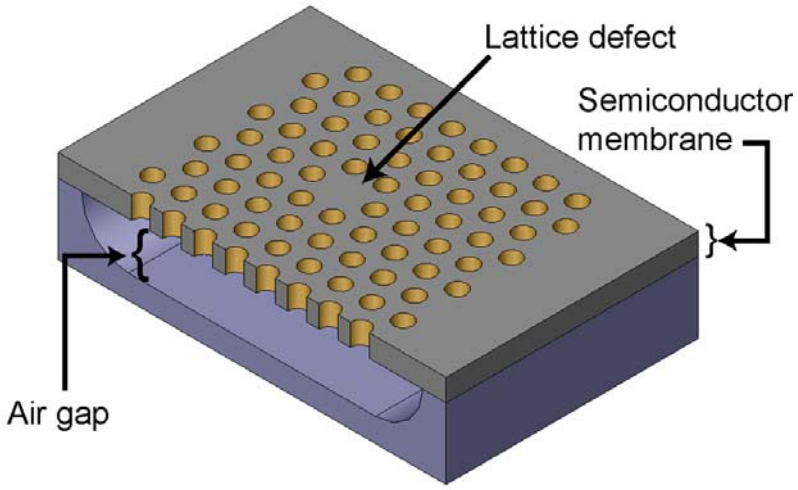

Figure 4.1: Schematic of a typical air-clad suspended semiconductor membrane 2D photonic crystal structure. A defect has been created by removing a single hole from the periodic lattice. The air gap is formed by selective chemical undercutting beneath the membrane.

of-plane optical confinement is thus provided by total internal reflection (TIR) at the horizontal air-dielectric interfaces, as in a typical slab waveguide [65]. The membrane is generally on the order of one-half a wavelength thick in the material, which ensures that it will support only a single slab mode. Other possible solutions for achieving optical confinement in all directions have included use of three-dimensional photonic crystals, such as stacked logpile [87] and angle-etched [88] structures. However, the air-clad TIR membrane structure has been the most common geometry, and is frequently adopted for its intrinsic advantages over the other 3D options in terms of fabrication simplicity.

The concept of using TIR for vertical optical confinement is equally applicable for ABR devices, and a similar thin single-mode membrane may be used. However, unlike

the typical 2D photonic crystal, the ABR structure is composed of concentric rings which are physically unconnected. If the substrate material beneath the membrane were removed, the ABR structure would collapse. Therefore, a different method for achieving strong out-of-plane optical confinement based upon epitaxial transfer has been developed, and will be discussed in detail below.

4.3 Semiconductor membrane slab mode design considerations

Annular Bragg resonators with large index contrast Bragg reflectors were realized in a membrane of active quantum well (QW) InGaAsP semiconductor material. The broadband photoluminescence from InGaAsP QWs provides a means of probing the modal properties of ABR devices at wavelengths in the near infrared relevant to optical telecommunication. In addition, optical gain within such a QW material allows for investigation of the performance of ABR microcavities as low-threshold lasers, a subject which will be explored in greater detail in Chapter 5. The semiconductor medium used is illustrated in Fig. 4.2. The 250 nm thick InGaAsP membrane consisted of 6 strained InGaAsP QWs and their barrier layers (75 Å wells, 1% compressive strain; 120 Å barriers, 0.5% tensile strain, $\lambda_g = 1.2\ \mu$m), which were sandwiched between two 605 Å InGaAsP ($\lambda_g = 1.2\ \mu$m) layers. The peak photoluminescence from the QWs occurred at $\lambda_{\text{peak}} = 1559$ nm. All epitaxial layers were grown by metal-organic chemical vapor deposition (MOCVD) on an InP substrate [89]. The 250 nm InP sacrificial layer can be selectively removed to produce an air gap below the patterned InGaAsP membrane, as in the case of the 2D photonic crystals discussed above. However, in the ABR fabrication process, the InP sacrificial layer and 50 nm InGaAsP stop etch are used to facilitate transfer of the InGaAsP QW membrane to an alternative substrate, as will be described below.

The out-of-plane optical confinement was investigated using a custom one-dimensional finite difference semi-vectorial mode solver (see [90] and Chapter 6) to analyze the

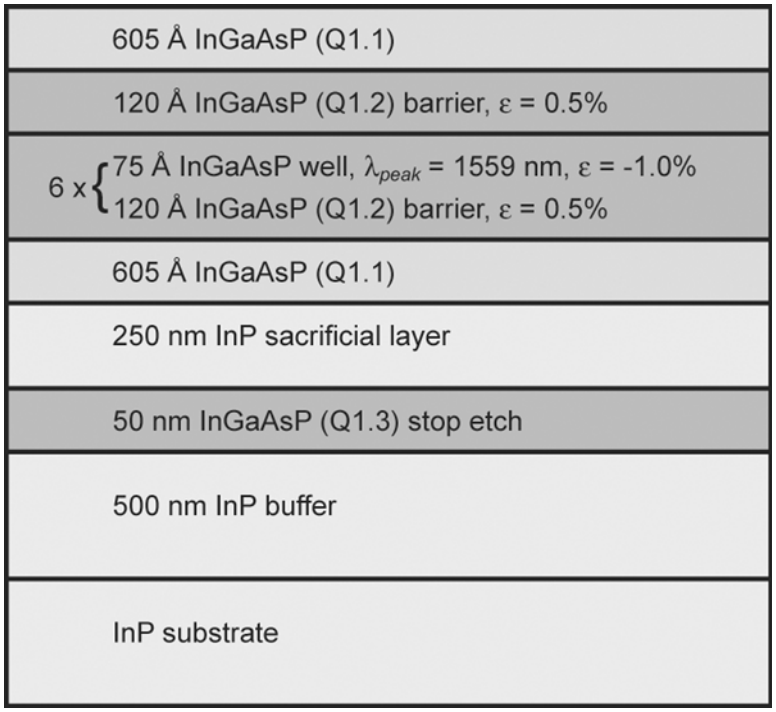

Figure 4.2: Schematic of the InGaAsP quantum well membrane epistructure used for the ABR devices. Where shown, the quantity in parentheses, i.e., (Q1.1), refers to the bandgap wavelength λ_g of the InGaAsP alloy in the given layer.

modes of the 250 nm thick InGaAsP slab. Since the optical gain in the 1% compressively strained InGaAsP quantum wells is greatest for electric fields polarized in the plane of the quantum wells [91, 92], i.e., E_r, and E_θ, the optical design focused upon the TE polarized ABR modes, which have field components H_z, E_r, and E_θ. The TE polarized modes are expected to have the lowest laser threshold, given the compressively strained quantum well design [93, 94].

The refractive index of the various quaternary alloys in the epitaxial structure of Fig. 4.2 were calculated using the empirical formula in reference [95], assuming a wavelength of $\lambda = 1.55$ μm. Figure 4.3 plots the refractive index profile of the as-grown InGaAsP membrane structure along the growth axis (z-axis), superimposed with the transverse electric field profile $E_x(z)$ of the fundamental TE polarized slab mode (electric field and x-axis parallel to the plane of the membrane). With the membrane in contact with the high-index ($n \sim 3.17$ at $\lambda = 1.55$ μm) InP substrate, the fundamental slab mode exists at the cut-off condition [65], where the modal effective index n_{eff} equals the refractive index of the substrate, i.e. $n_{eff} \sim n_{substrate} = 3.17$. As a result, the mode is broadly distributed and extends deep into the InP substrate. Furthermore, the mode has peak amplitude at the depth of the InGaAsP stop etch layer, and thus possesses a small overlap with the quantum wells in the center of the membrane. These factors predict that the while the InGaAsP semiconductor membrane remains clad from below by the high-index InP substrate, the optical modes of ABR structures patterned into the membrane will suffer from large substrate radiation losses and low optical gain.

In order to achieve strong out-of-plane optical confinement, the InGaAsP membrane must be clad by low-index material both above and below. As discussed above, the ABR geometry prohibits use of the suspended membrane configuration. Therefore, an epitaxial layer transfer technique [96, 97], using UV-curable Norland optical adhesive NOA 73 (Norland Products, $n \sim 1.56$ at $\lambda = 1.55$ μm), was adopted to facilitate transfer of the InGaAsP membrane to a transparent sapphire substrate. Figure 4.4 shows the fundamental TE polarized mode supported when the InGaAsP membrane is clad below by the NOA 73 adhesive and above by air. In comparison with

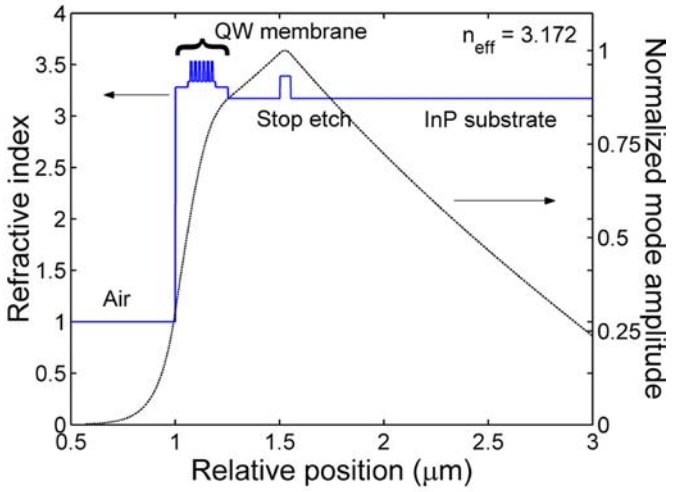

Figure 4.3: Fundamental TE polarized slab mode profile $E_x(z)$ supported by the as-grown InGaAsP-InP epistructure, superimposed against the refractive index profile, evaluated at $\lambda = 1.55$ μm. The mode is nearly cut off, and extends deep into the high-index InP substrate.

Fig. 4.3, the optical mode is far more confined within the membrane, and has a peak amplitude overlapping with the quantum wells, as desired for maximizing the optical gain. The peak is shifted slightly towards the NOA 73 layer, due to the asymmetry in refractive index between the air and NOA 73 claddings. Numerical calculations confirmed that the transferred membrane supported only a single TE transverse mode, with $n_{eff} = 2.822$. Therefore, an effective index of 2.8 has been assumed for the majority of the ABR numerical designs and experimentally demonstrated devices presented in Chapters 3 and 5, respectively.

4.4 ABR fabrication

The ABR fabrication process flow is illustrated in Fig. 4.5 [97, 98]. The lower case letters in parentheses (a-h) included in the following description refer to the corresponding cross-sectional schematic in Fig. 4.5.

First, a 120 nm SiO_2 etch mask layer was deposited on top of the InGaAsP-InP semiconductor substrate by plasma enhanced chemical vapor deposition (PECVD)

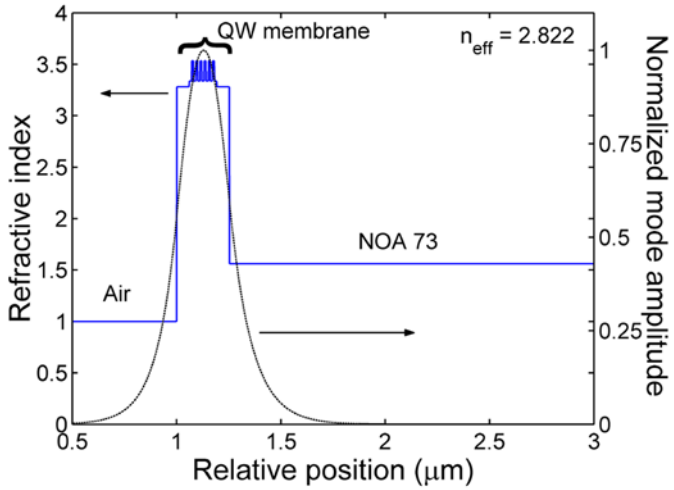

Figure 4.4: Fundamental TE polarized slab mode profile $E_x(z)$ supported by the InGaAsP membrane after epitaxial transfer using Norland optical adhesive NOA 73, evaluated at $\lambda = 1.55$ μm. The mode is well confined to the InGaAsP membrane, and has a large overlap with the quantum wells.

(a). Approximately 550 nm of poly(methyl methacrylate) (PMMA) electron beam resist was then applied by spin-coating and baked to drive off solvents (b). Several ABR geometries were patterned into the PMMA layer using a Leica Microsystems EBPG 5000+ direct electron beam writer operating at 100 kV accelerating voltage. Development of the patterned PMMA film was carried out in a solution of 1:3 methyl isobutyl ketone:isopropyl alcohol (MIBK:IPA) for 60 seconds (c). The SEM cross-section through a typical PMMA pattern shown in Fig. 4.6 illustrates a characteristic result from this high-resolution lithography.

Subsequently, the PMMA patterns were transferred into the SiO_2 etch mask layer by inductively coupled plasma reactive ion etching (ICP-RIE) using C_4F_8 plasma, in an Oxford Instruments Plasmalab System100 tool (d). The remaining PMMA was removed with a gentle O_2 plasma ashing step. The patterned SiO_2 layer then served as a hard mask for transfer into the active InGaAsP membrane, using a low-voltage ICP-RIE etch employing HI/Ar chemistry (e) [99]. The HI/Ar system has two significant advantages over more common alternative chemical systems for etching InP-based semiconductors, such as $CH_4/H_2/Ar$ and Cl_2/Ar. First, no polymeric deposits form

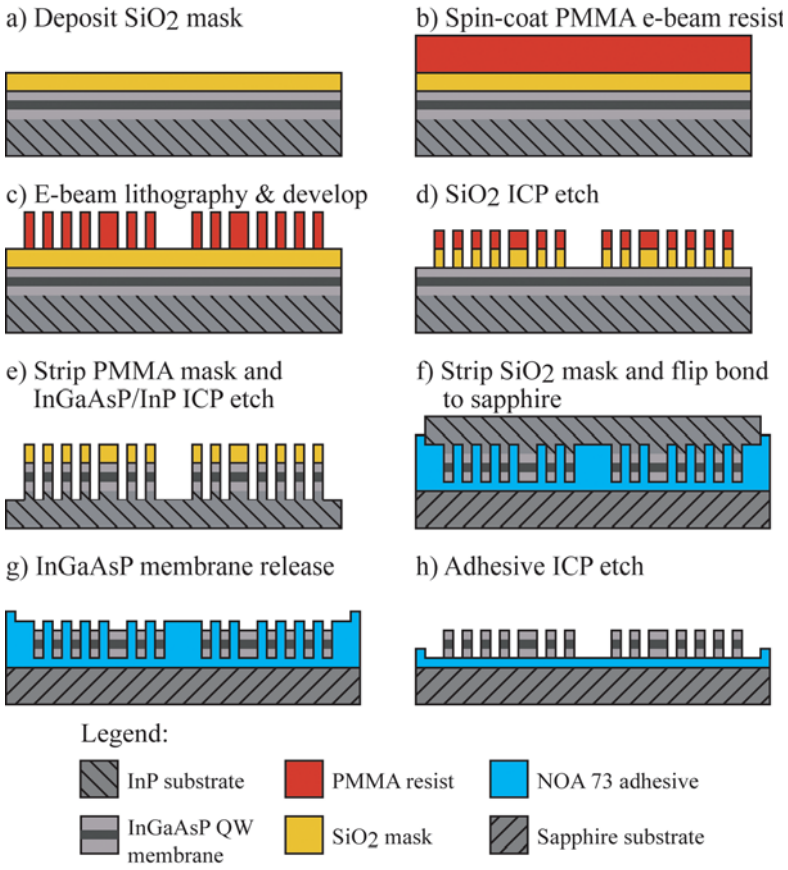

Figure 4.5: Flow diagram for the ABR fabrication and polymer bonding process. The dark region in the middle of the InGaAsP QW membrane is intended to represent the location of the quantum wells.

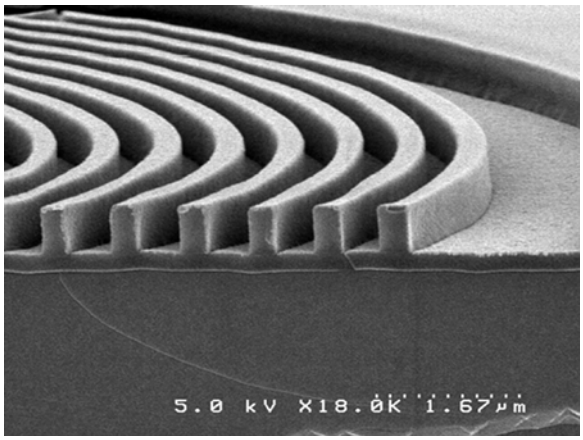

Figure 4.6: Cross-section of PMMA pattern after electron beam lithography and development. The thin horizontal SiO_2 mask layer can be seen between the PMMA and the substrate. The sample was coated with a thin layer of gold to prevent charging during imaging.

on the sample or chamber walls during etching, as is typical with the frequently used $CH_4/H_2/Ar$ gas chemistry [100]. Second, the InI_x etch products generated at the exposed semiconductor surfaces are quite volatile at room temperature. Therefore, sample heating is not needed to enhance etch product desorption, as is generally required in the case of the rather involatile $InCl_x$ etch products formed on the semiconductor surfaces when using Cl_2/Ar reactive gas mixtures [101]. In the etch recipe typically used, the HI/Ar gas flow was 10/6 sccm, the chamber pressure was 5 mTorr, and the ICP and RF electrodes were driven with 950 W and 30 W, respectively. The plasma DC self-bias was ∼100 V, and the etch rate was ∼325 nm/min. The SiO_2-masked ABR samples were etched for 1 minute, to a depth penetrating completely through the InGaAsP membrane and partially into the InP sacrificial layer. The remaining SiO_2 hard mask was then stripped in a buffered hydrofluoric acid solution.

Several SEM images of a typical ABR device at this stage in the fabrication process are shown in Figs. 4.7, 4.8, and 4.9. Figure 4.7 provides a view of the entire ABR resonator. Figure 4.8 shows a magnified view of the annular Bragg layers after SiO_2 removal. Figure 4.9 is a cross-section through the etched ABR structure, with the SiO_2 etch mask still remaining. These SEM images illustrate the smooth

anisotropic features generated by the HI/Ar etch used to define the Bragg reflectors. The vertical striations visible on the etched sidewalls in Figs. 4.8-4.9 originate from the 10 nm resolution with which the ABR patterns were fractured prior to electron beam lithography.

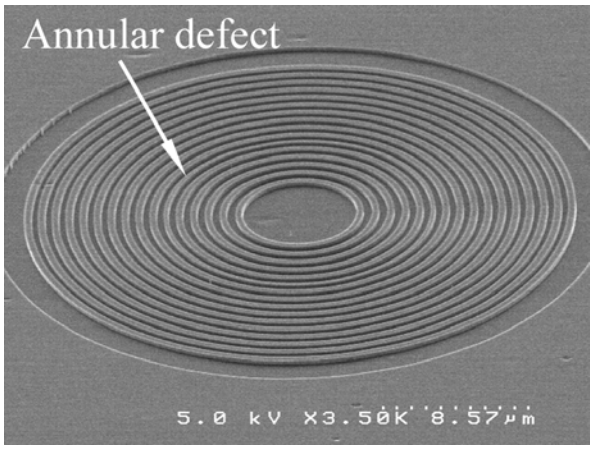

Figure 4.7: SEM image taken after HI/Ar ICP-RIE etch and SiO_2 mask removal, with the ABR sample tilted at approximately 40° with respect to the electron beam. The annular defect is the (slightly narrower) sixth ring from the center.

Next, the epitaxial layer transfer technique was begun by applying the NOA 73 optical adhesive to the patterned InGaAsP surface by spin-coating, and the entire sample was flip-bonded to a crystalline sapphire substrate (f). The adhesive was then cured by illumination with an ultraviolet lamp through the sapphire. Subsequently, the InP substrate was removed by a combination of mechanical polishing and selective wet chemical etching. Mechanical polishing was performed using a slurry of water and aluminum oxide powder with 5 μm particle size. A chemical etchant consisting of 3:1 HCl:H_2O was used to remove the InP, and a mixture of 1:1:4 H_2SO_4:H_2O_2:H_2O was used to remove the 50 nm InGaAsP stop etch layer. This procedure left only the 250 nm thick patterned active InGaAsP membrane encapsulated within the cured optical adhesive film (g). The transferred ABR devices demonstrated excellent adhesion over the entire sample. Finally, the adhesive filling the trenches was removed with a selective isotropic NF_3/O_2 ICP-RIE etch, to improve the lateral refractive

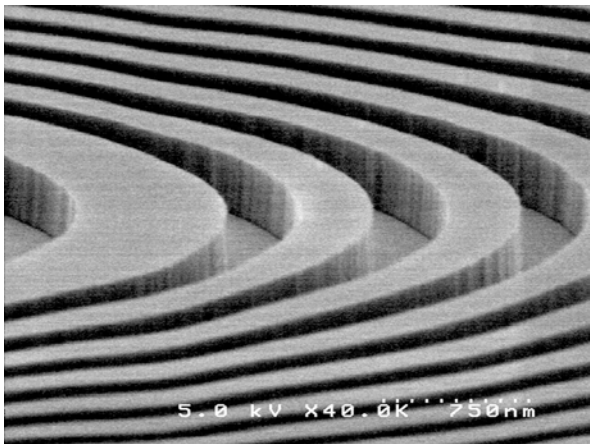

Figure 4.8: Magnified SEM image of etched semiconductor grating, angled to illustrate vertical and smooth sidewalls produced by HI/Ar etch process. The SiO_2 mask has been removed at this stage.

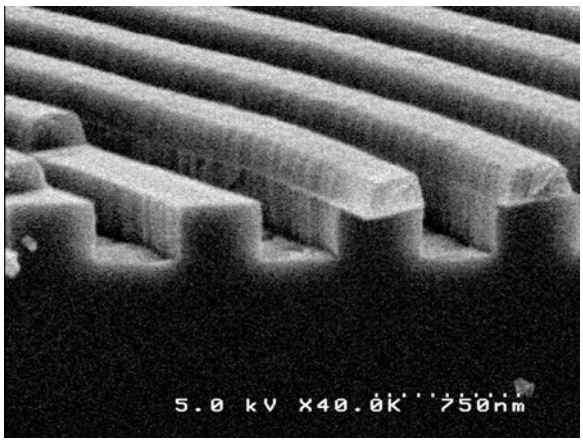

Figure 4.9: Cross section through ABR after HI/Ar etch, showing excellent anisotropic profile. The SiO_2 mask still remains on top of the semiconductor membrane.

index contrast (h). The SEM image in Fig. 4.10 shows a magnified view of several transferred annular rings taken after adhesive removal. This image was obtained using an environmental SEM (ESEM) operating at a water vapor pressure of 0.45 Torr in the chamber, and an accelerating potential of 5 kV, in order to mitigate charging effects from the non-conductive sapphire substrate and optical adhesive. Comparison of Fig. 4.8 with Fig. 4.10 shows no obvious roughening or milling of the semiconductor surfaces, suggesting that exposure to the NF_3/O_2 plasma process is not expected to generate any additional sources of optical scattering loss.

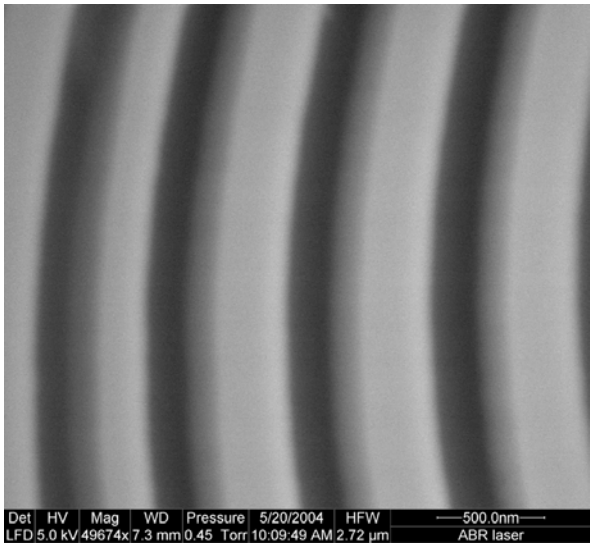

Figure 4.10: Magnified ESEM image of semiconductor rings, taken after epitaxial transfer to the sapphire substrate and optical adhesive etching. Brighter regions are the top and side surfaces of the semiconductor rings, dark regions are the trenches from which the adhesive was removed.

An atomic force microscope (AFM) can be used as an alternative means of imaging the transferred InGaAsP membrane. Several contact mode AFM images obtained within a small region of a typical transferred ABR device are shown in Fig. 4.11. Figure 4.11(a) contains the three-dimensional surface profile of the ABR taken before ICP-RIE etching of the NOA 73 adhesive (i.e., between fabrication steps (g) and (h)). Because the semiconductor substrate was etched through the 250 nm membrane to a depth of $\sim$325 nm, the profile of the cured NOA 73 adhesive (light regions) is raised

above the height of the semiconductor rings (dark regions). A cross-section of the 3D profile taken at $y = 2$ μm is plotted in Fig. 4.11(b). The raised ridges of cured adhesive between the flat semiconductor regions are clearly visible. A similar image taken after etching the adhesive (from a slightly different ABR device having narrower trenches) and an associated cross-section trace are shown in Figs. 4.11(c)-(d). In this case, the profile of the semiconductor rings (light regions) is raised above the areas in which the adhesive has been removed (dark regions). The cross-section shows narrow trenches between the protruding semiconductor ridges. The triangular shape of the trenches is an imaging artifact due to convolution of the AFM probe tip with the sharp edges of the semiconductor rings. The sloping tops of the semiconductor ridges are due to an artifact produced by an improperly functioning scan stage on the AFM used.

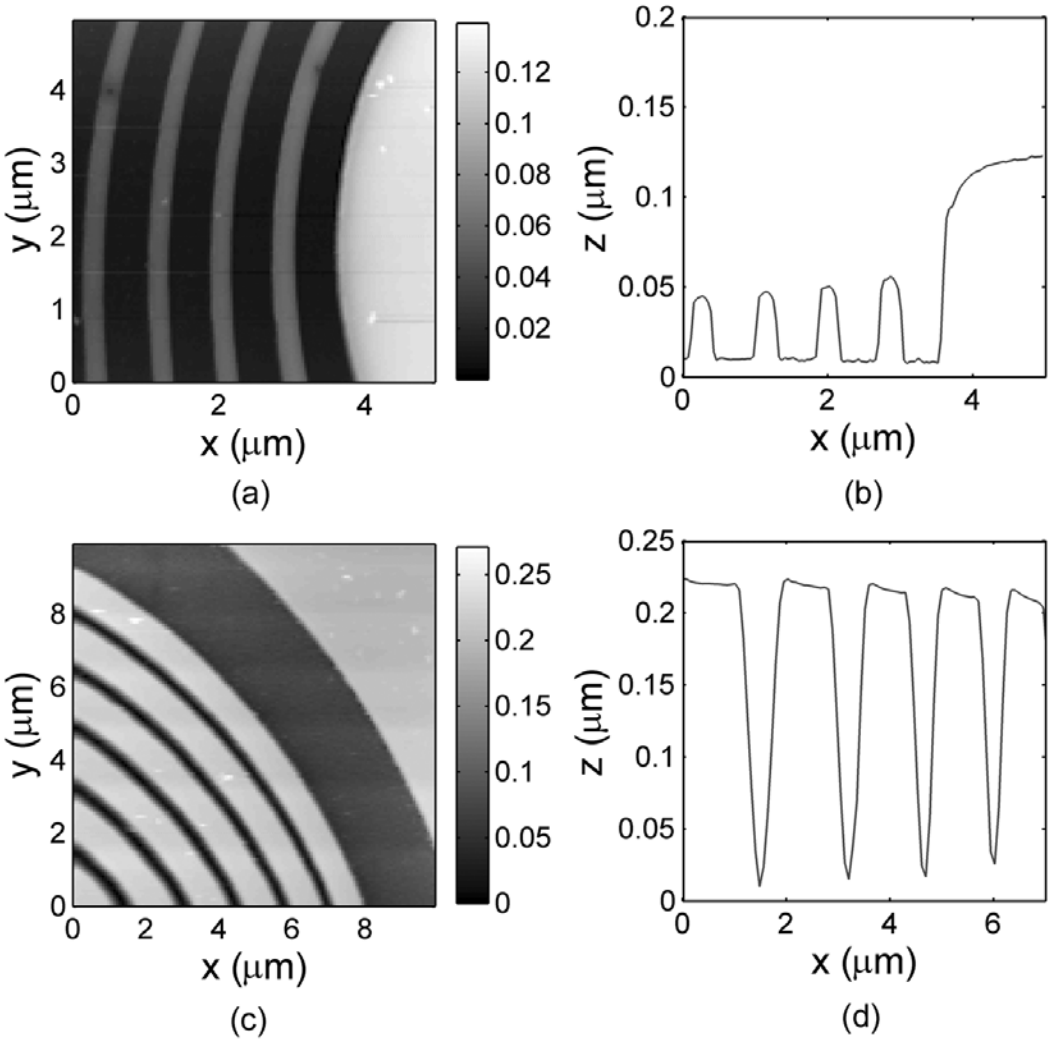

Figure 4.11: (a) AFM image showing surface profile of a small region of an ABR membrane after epitaxial transfer to a sapphire substrate, taken before adhesive etching. (b) Cross section of the image in (a) (through $y = 2$ μm), showing cured adhesive ridges (high points) raised above level of semiconductor rings (low points). (c) AFM surface profile taken after adhesive etching. The device imaged here is not the same as the one shown in (a)-(b). (d) Cross-section of the image in (c) (through $y = 2$ μm), illustrating the trenches where the adhesive has been removed.

Chapter 5

Vertically emitting radial defect and nanocavity ABR lasers

5.1 Introduction

Applying the theoretical and practical frameworks developed in the previous chapters for the design and fabrication of cylindrical Bragg microcavities, this chapter presents the experimental characterization of several vertically emitting ABR laser geometries. First, the apparatus used for pulsed optical excitation of the ABR devices will be described, along with the optical components used for collection of the photoluminescence signal and imaging of the ABR near field emission patterns. Subsequently, data demonstrating low threshold lasing from radial defect ABR microcavities will be presented, and various characteristics of the observed ABR laser emission, including polarization and linewidth, will be discussed. Images of the near field emission patterns from several ABR devices, obtained with an infrared camera above laser threshold, will then be presented, serving to illustrate that laser action occurs in spatial modes having low azimuthal number guided within the ABR defect layer. Next, the emission spectra observed from the radial defect ABR lasers will be further characterized, by comparison with a numerically predicted spectrum calculated using the finite-difference time-domain algorithm. The sensitivity of ABR microcavities to electron beam lithography process variations will then be evaluated, with applications to lithographic tuning. Finally, an alternative Bragg nanocavity

design, in which a small central semiconductor pillar is surrounded by a cylindrical Bragg reflector, will be presented. This resonator geometry is optimally designed to support the non-degenerate $m = 0$ mode, and is theoretically predicted to have ultra-small mode volume. Characteristic low threshold single-mode lasing spectra obtained from this Bragg nanocavity will be presented and discussed.

5.2 Apparatus for optical excitation

The optical apparatus for characterizing the ABR laser devices was assembled as shown in Fig. 5.1. The ABR resonators were pumped by pulsed optical excitation, using a mode-locked Ti:sapphire laser emitting ∼100 fs FWHM pulses at a repetition rate of 78 MHz, with a center wavelength of $\lambda_p = 890$ nm. A 50/50 non-polarizing beamsplitter was used to direct 50% of the pump power to a wavemeter/calibrated optical power meter for monitoring of the pump power directed at the ABR devices. The pump beam was incident normal to the plane of the ABR devices, and focused through the transparent sapphire substrate with a 50x (NA = 0.42) microscope objective. The vertically emitted photoluminescence (PL) signal was collected from the side of the device opposite to the pump beam, using a 20x (NA = 0.42) microscope objective. The collected PL was then focused into a multimode optical fiber and fed into an optical spectrum analyzer (OSA). The OSA wavelength resolution was 1 nm. Alternatively, the emitted PL could be directed to an infrared (IR) vidicon camera, for imaging of the ABR near field intensity profile. The white light source and CCD camera were used to image the position and diameter of the focused Ti:sapphire pump spot, relative to the ABR resonator under test. The pump spot size was manipulated by changing the position of the pump objective's focal plane with respect to the plane of the ABR, as shown in the lower right corner of Fig. 5.1. The ABR sample was aligned to the pump spot using a precise 3 axis translation stage with piezoelectric motion control, permitting careful positioning at the sub-micron scale. Measurements were performed at room temperature.

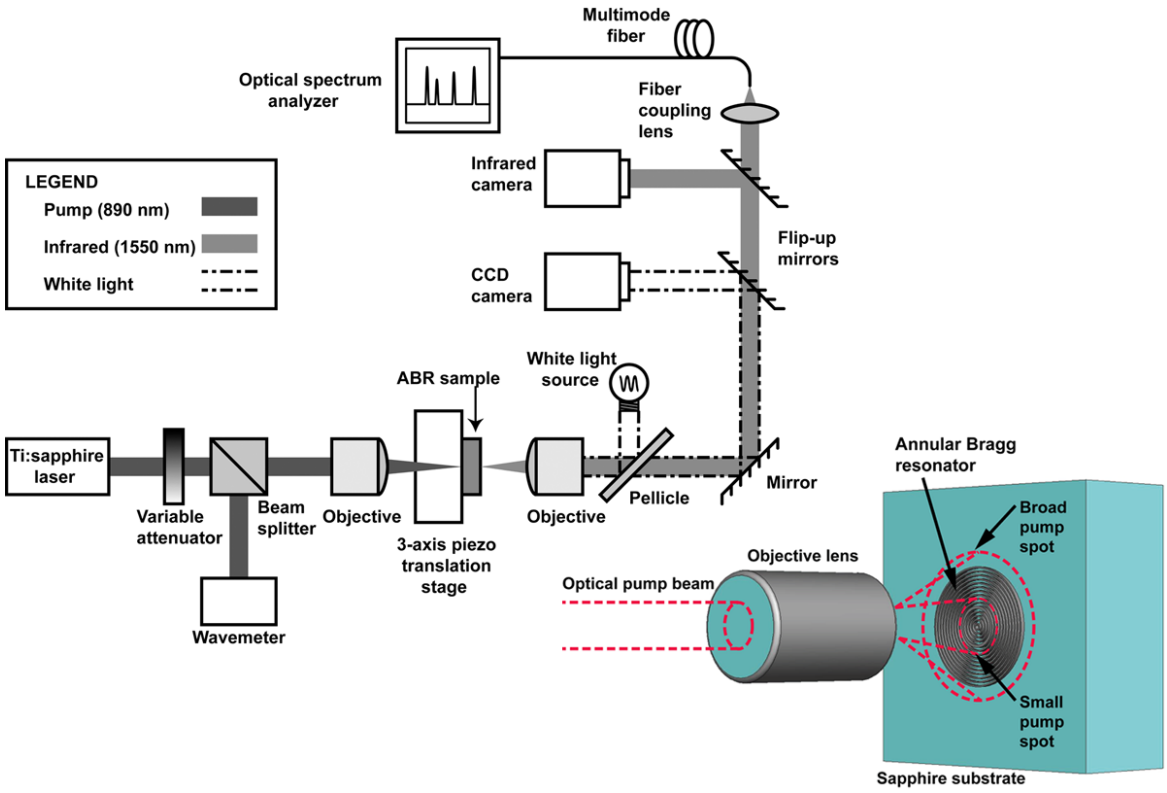

Figure 5.1: Schematic of the measurement apparatus used to optically pump the semiconductor ABR lasers, and to image the vertically emitted photoluminescence. The legend shows the paths followed by the pump, infrared photoluminescence, and white light beams. The positioning of the pump spot with respect to the ABR device is illustrated in the magnified view in the lower right corner.

5.3 Characterization of radial defect ABR emission spectra and near field emission profiles

5.3.1 Description of ABR structure parameters

Figure 5.2 shows an SEM image of the ABR geometry for which the optical emission characteristics are evaluated below. The Bragg reflectors were of mixed order, with second-order high-index and first-order low-index layers. The grating pitch was chirped from 0.91 μm to 0.81 μm from the inner to the outer perimeter. The width of the high-index semiconductor defect was 0.28 μm, chosen for a first-order defect ("effective" $\lambda/2n$ wide), and the defect radius was 7.72 μm. The defect layer and cylindrical reflectors were together designed to support an azimuthally propagating mode with $m = 7$ at a wavelength of $\lambda = 1550$ nm. The Bragg reflectors were composed of 5 periods to the inside of the radial defect, and 10 periods to the outside. The radius of the innermost and outermost semiconductor layers were 3.5 μm and 16 μm, respectively. As discussed in Chapter 3, the radial component of a wave resonant with the cylindrical grating completes a full optical cycle between successive grating "periods," owing to the mixed-order design. Thus, waves diffracted vertically from consecutive periods have phase differences of 2π and interfere constructively [48], leading to efficient vertical emission into the collection objective normal to the plane of the ABR.

5.3.2 Below threshold quantum well spontaneous emission

When an unpatterned region of the epitaxially transferred InGaAsP QW membrane was illuminated with a focused pump beam having $\sim$3 μm spot diameter, broadband spontaneous emission was observed. This emission originates from optical transitions between the lowest energy confined electron (e1) and heavy hole (hh1) states within the QWs [102]. Figure 5.3(a) contains a series of PL spectra obtained as a function of the pump power incident upon the membrane. At a pump power of 1 mW, the peak PL occurs at a wavelength of 1559 nm, with a FWHM of approximately 70

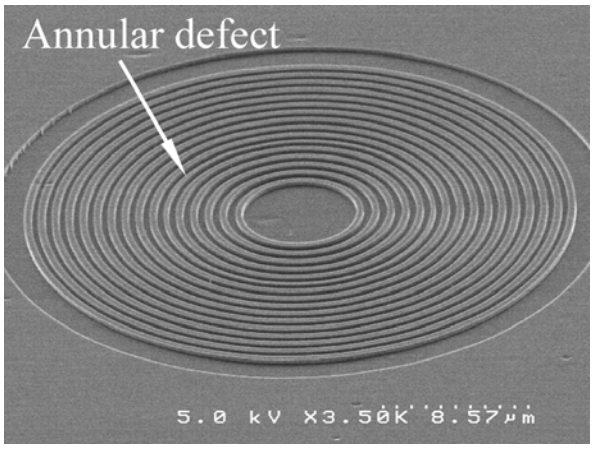

Figure 5.2: SEM image of the radial defect ABR geometry described and tested. The annular defect layer is the sixth ring from the center.

nm. As the pump power is increased to 20 mW, the emitted PL intensity increases, the FWHM peak width broadens to ∼120 nm, and the PL peak is redshifted to a wavelength of 1575 nm. Heating of the membrane due to hot carrier intraband relaxation and non-radiative interband recombination of photogenerated electron-hole pairs results in broadening of the energy distribution of electrons and holes within the QW subbands [103], and is thus responsible for the observed peak broadening. Redshifting of the peak is again due to thermal effects, due to the typical reduction of the semiconductor bandgap energy with increasing temperature [104].

When an ABR defect resonator such as the one shown in Fig. 5.2 is optically pumped, the PL spectrum observed is substantially different. For these measurements, the pump spot was defocused to a diameter of ∼16 μm and centered over the resonator, to ensure even illumination of the radial defect. For incident pump powers significantly below 1 mW, the observed spontaneous emission spectrum generally consists of one or more narrow peaks with spectral widths on the order of a few nanometers, superimposed upon a typical broadband QW PL background. The narrow peaks occur at the wavelengths λ of the resonant modes of the ABR device. For example, Fig. 5.3(b) plots a restricted spectral region in which one such peak is found. The low signal-to-noise ratio in the experimental data is due to the weak

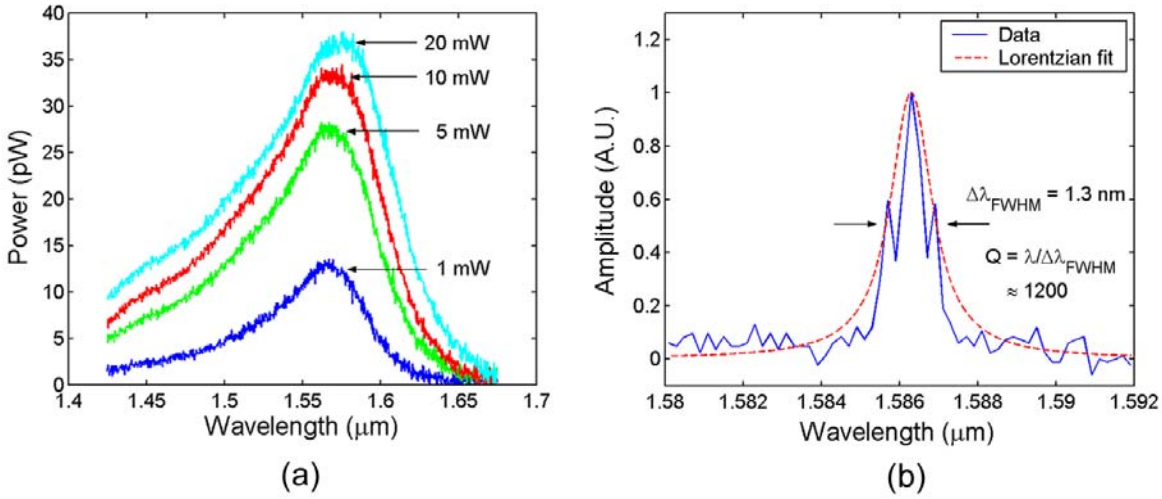

Figure 5.3: (a) Quantum well photoluminescence spectra from an unpatterned region of the transferred InGaAsP membrane, as a function of incident pump power. As the pump power is increased, the PL peak is slighly redshifted, and the spectral FWHM broadens, due to membrane heating. (b) Below threshold photoluminescence from an ABR device. The Lorentzian lineshape fitted to the spontaneous emission peak suggests a quality factor $Q \sim 1200$.

intensity of light emitted from the ABR modes at low pump power, requiring measurement near the noise floor of the OSA. The linewidth $\Delta\lambda_{FWHM}$ of the ABR PL peak, measured at a pump power just below laser threshold where the QW material is approximately transparent, can be used to provide an estimate of the quality factor Q of the resonant mode [105, 106], given by $Q = \lambda/\Delta\lambda_{FWHM}$. Numerically fitting a Lorentzian lineshape to the data, the linewidth was found to be $\Delta\lambda_{FWHM} = 1.3$ nm, giving $Q \sim 1200$. Peaks in the ABR spontaneous emission from optical modes at several wavelengths and various different ABR devices were found to suggest similar values of Q, all on the order of 10^3.

The limited quality factors observed below threshold originate from various contributions to the unsaturable optical losses within the ABR microcavity. Sources of material-related optical losses can include scattering from the interfaces between the numerous epitaxial layers within the InGaAsP membrane [107], which depends upon the quality of the crystal growth. In addition, although the entire 250 nm InGaAsP

membrane was grown nominally undoped, the typical background doping for such III-V semiconductor alloys is n-type with a concentration of approximately 1×10^{15} cm^{-3} [108], giving rise to a loss contribution from free carrier absorption [109–111]. Additional sources of scattering and absorption loss can be introduced during the course of the ABR fabrication process. For example, roughness on the etched sidewalls of the membrane originates from the finite resolution of electron beam lithography (roughness in the PMMA patterns) and ultimately transfers into the InGaAsP semiconductor. The semiconductor reactive ion etching step itself can generate some additional intrinsic sidewall roughness. This sidewall roughness can give rise to significant scattering [112–114], particularly because of the large refractive index contrast between the semiconductor layers and low-index trenches, and the large total number of sidewalls intersecting the ABR optical modes. Furthermore, the semiconductor reactive ion etching step leaves behind an unterminated semiconductor surface with dangling bonds, and also generates ion damage proportional to the energy of ions bombarding the surface. Both these processes can lead to generation of a large density of surface states within the semiconductor bandgap, giving rise to a degree of optical absorption [115,116]. Finally, although the in-plane radiative losses are rendered very small by the high-reflectivity cylindrical Bragg reflectors, out-of-plane radiative losses may contribute to limit the Q. Using a symmetrical slab structure, with material of the same refractive index both above and below the semiconductor membrane, would help to reduce the vertical losses. Further reduction of vertical radiation could be obtained by increasing the thickness of the semiconductor membrane [117].

5.3.3 Onset of laser oscillation and characteristics of laser spectra

As the optical pump power was increased, a sharp increase in the emitted IR power was observed due to the onset of laser oscillation, occurring at the same wavelengths at which narrow peaks were found in the spontaneous emission spectrum [97]. The integrated power collected from the ABR within the spectral range from 1500 nm

- 1660 nm is plotted in Fig. 5.4(a). Evidence for laser action from this device is given by a clear threshold occurring at a pump power of $P_{th} \sim 860$ μW. Emission spectra obtained under several pump intensities are illustrated in Fig. 5.4(b), showing multiple lasing modes. Under these measurement conditions, two separate groups of lasing modes were observed, each with a distinct free spectral range (FSR) and laser threshold behavior. At low pump power ($P_p = 1.17$ mW, $P_p = 1.52$ mW), resonances at $\lambda_1 = 1588.7$ nm, $\lambda_2 = 1614.0$ nm, and $\lambda_3 = 1562.6$ nm, dominated the spectrum. The FSR of this first group of modes was ~25.5 nm. At an increased pump power of 1.77 mW, an additional mode at $\lambda_4 = 1622.2$ nm appeared, and at $P_p = 2.06$ mW, a mode at $\lambda_5 = 1601.4$ nm appeared. These new modes were attributed to a second group, owing to their narrower linewidth and smaller FSR of ~20.8 nm. Further increase in pump intensity resulted in increased emission from this second group of modes, with emission from the first group showing saturation. A weak feature at $\lambda_6 = 1538.0$ nm, belonging to the first group, appeared at the highest pump powers.

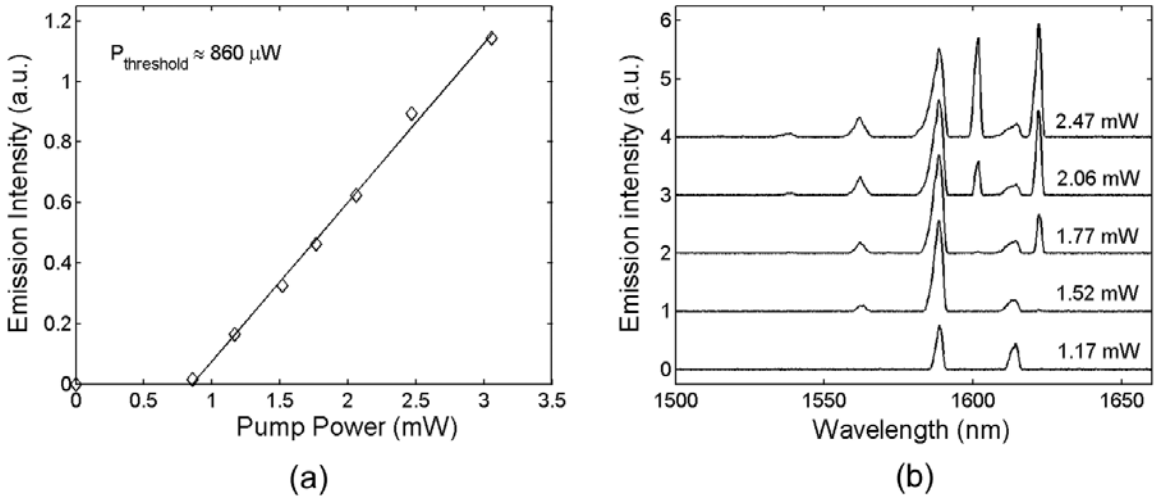

Figure 5.4: (a) L-L curve of integrated ABR emission vs. pump power, showing laser threshold at $P_{th} \sim 860$ μW. (b) Optical spectra collected from lasing ABR cavity. Spectra are vertically offset to illustrate the effects of increasing pump power.

The multiple modes belonging to each group are likely to posses a similar radial profile, with consecutive azimuthal numbers (m, $m+1$, $m+2$, etc.). Dissimilarities

in the threshold and FSR between the two groups of modes suggest they may possess slightly different radial profiles and/or different overlap with the pump spot. Differences such as these could arise from multiple transverse modes within the radial defect, and/or localization at different radii within the ABR structure.

Further insight into the origin of the observed lasing modes can be obtained by considering the limited numerical aperture of the collection optics. For the measurement configuration used here, in which the collection objective positioned normal to the plane of the ABR device, the dependence of the vertical diffraction angle in air upon the modal azimuthal number m influences the collection efficiency for light diffracting from the cylindrical Bragg grating [47]. Azimuthally propagating modes in the ABR structure contain $\exp(im\theta)$ dependence. Upon circulating around a loop of radius R, the mode advances in phase by $\exp(ik_\theta L) = \exp(i2k_\theta \pi R) = \exp(i2m\pi)$, resulting in $k_\theta = m/R$. Given that the first harmonic of the mixed order grating's crystal momentum, k_G, cancels the radial component of the modal wavevector, k_ρ (i.e. $k_\rho = -k_G$), it is possible to use Snell's law to estimate the air diffraction angle θ_0 in the azimuthal direction, as illustrated in Fig. 5.5. Recalling that the numerical aperture of the 20x collection objective is 0.42, one finds that a mode must satisfy the criteria

$$\sin(\theta_0) = \frac{k_\theta}{k_0} = \frac{m\lambda}{2\pi R} < 0.42 \tag{5.1}$$

in order to enter the finite numerical aperture of the collection optics. At $\lambda = 1.59$ μm (near the middle of the spectral region plotted in Fig. 5.4(b)), Eq. 5.1 is satisfied only for $m \lesssim 26$, where $R = 16$ μm has been assumed, corresponding to the outer radius of the ABR device. While the semiconductor rings in the mixed-order Bragg reflectors are wide enough ($\sim$0.43 μm) to support relatively low loss whispering gallery modes (WGMs) by index guiding (when considered in isolation from the rest of the grating), these modes are expected to have $38 \lesssim m \lesssim 187$, estimated using

$$m\lambda \approx 2\pi R n_{eff}, \tag{5.2}$$

where 3.5 μm $\leq R \leq$ 16 μm and $n_{eff} = 2.8$ were assumed. Therefore, the vertically

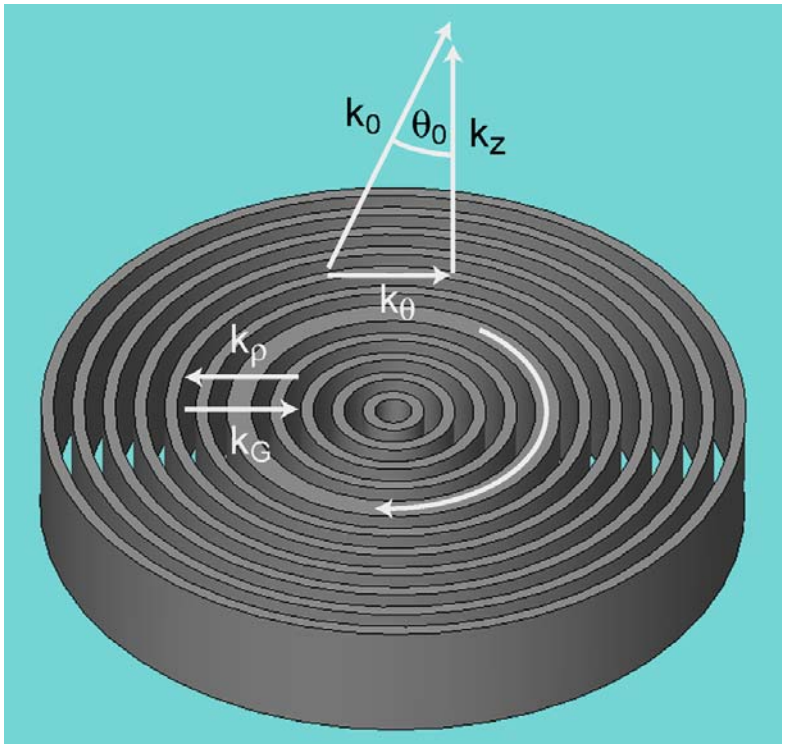

Figure 5.5: Illustration of wavevector components contributing to vertical diffraction within an ABR with a mixed order grating. The radial component k_ρ is cancelled by the first harmonic of the grating vector k_G, while the azimuthal and vertical components k_θ and k_z sum to give a wavevector k_0 in air.

collected ABR emission leading to the observed spectral features in Fig. 5.4(b) can be attributed to Bragg-guided low-order azimuthal modes, for example, modes localized within the ABR radial defect, as opposed to TIR-guided WGMs.

It should be noted that a small amount of blueshifting of all the lasing peaks in Fig. 5.4(b) was observed as the pump power was increased. This spectral shift was attributed to free carrier dispersion effects caused by the high density of photo-generated electron-hole pairs, and the associated reduction of the refractive index of the InGaAsP semiconductor membrane [109, 111]. This implies that for the range of incident optical pump powers used, generally < 4 mW, any membrane heating effects present were dominated by free carrier dispersion effects. If significant membrane heating was occurring, redshifting of the laser spectra with increasing pump power would be expected, owing to the positive sign of the thermooptic coefficient dn/dT for InGaAsP, and the associated increase in the index of refraction [38]. However, it was observed that at pump powers in the range of ∼6-10 mW (depending upon the pump focal spot size), optical heating of the ABR semiconductor membrane and the NOA 73 adhesive led to reflow of the adhesive, as the glassy temperature of the UV cured polymer material was exceeded. Adhesive reflow and subsequent re-solidification led to small shifts in the relative positions of the semiconductor rings, and altered the local planarity of the membrane, resulting in permanent damage to the ABR device.

5.3.4 Polarization of ABR defect modes

The polarization characteristics of the various lasing modes shown in Fig. 5.4(b) were investigated by introducing a linear polarizer into the PL collection path, between the ABR laser and the multimode fiber in Fig. 5.1. The pump power used was ∼2.5 mW, such that modes belonging to both the first and second groups discussed above had reached laser threshold. A series of spectra were obtained for various rotation angles of the polarization axis. Plotting the integrated power within a narrow spectral band encompassing each individual lasing peak against the polarization angle, the modes of two distinct groups of lasing modes were found to exhibit different po-

larization characteristics [97]. Figure 5.6 plots two polarization characteristics which are representative of the modes in each group.

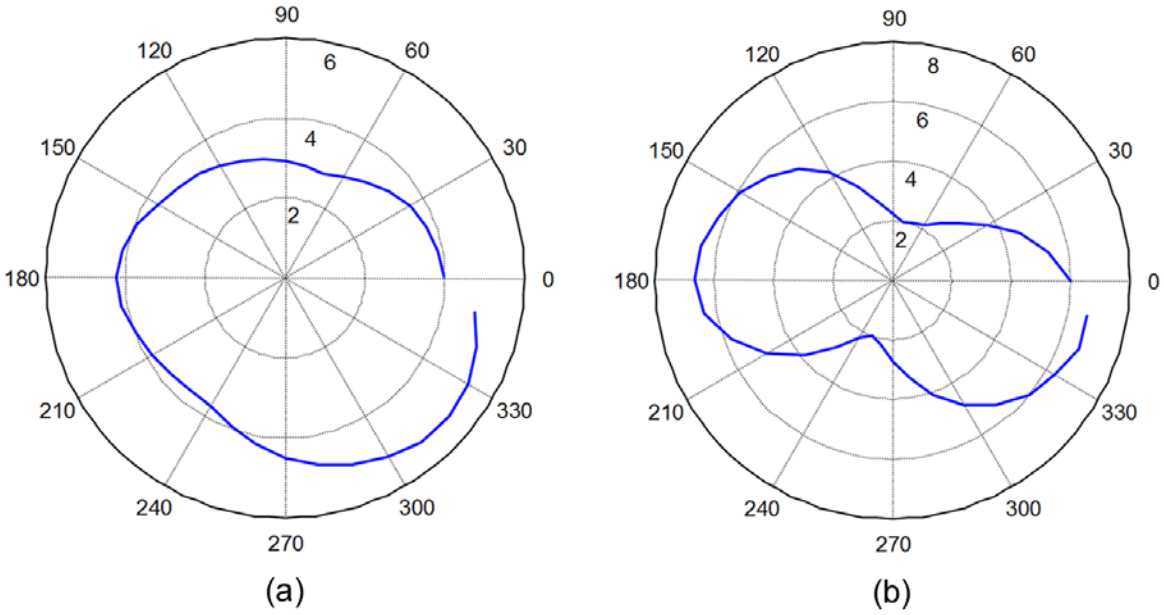

Figure 5.6: Integrated power versus polarizer angle for ABR laser modes belonging to the first and second groups. (a) Modes of the first group exhibit approximately unpolarized emission. (b) Modes of the second group exhibit partially polarized emission.

The emission from the modes of the first group is relatively unpolarized, as shown in Fig. 5.6(a). The egg-shaped deformity of the polarization characteristic and the offset between the start and end of the curve near 0° are due to drift in the intensity of the optical pump beam during the time taken to acquire the data. On the other hand, Fig. 5.6(b) shows that the emission from the modes of the second group is partially polarized.

Figure 5.7(a) plots the theoretical $H_z(\overrightarrow{r})$ spatial field distribution of the $m = 7$ TE mode within an ABR defect resonator similar to the device tested. The outlines of the high index rings are overlaid for clarity. Figure 5.7(b) plots an enlarged view of the fields within the boxed region in Fig. 5.7(a), showing a quiver plot of the in-plane electric fields $E_\rho(\overrightarrow{r})$ and $E_\theta(\overrightarrow{r})$, in addition to the $H_z(\overrightarrow{r})$ distribution in color. For the magnified region shown, the arrow directions illustrate that within

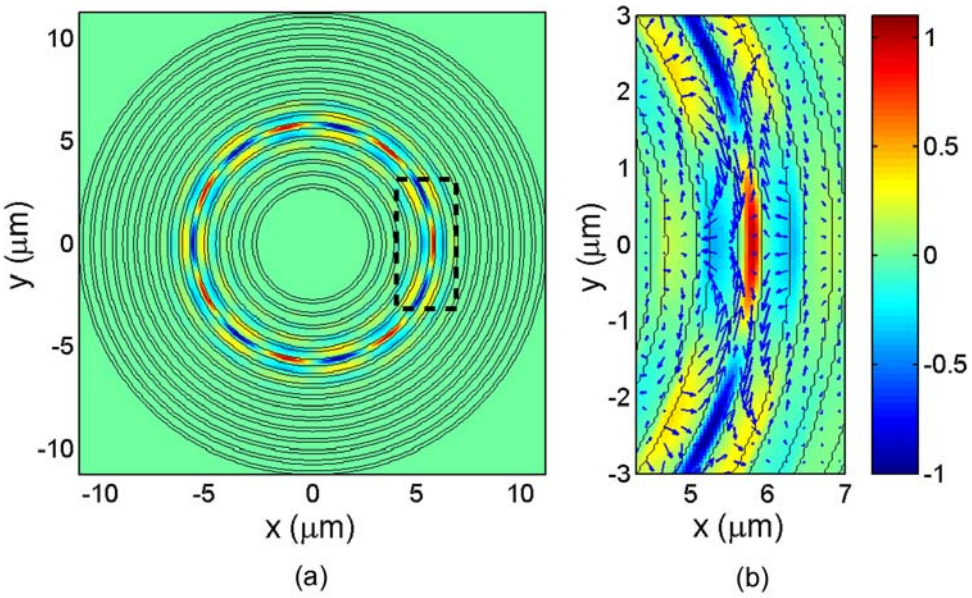

Figure 5.7: (a) Spatial field distribution $H_z(\overrightarrow{r})$ for a typical ABR radial defect mode having $m = 7$. (b) Field distribution within the boxed region from (a). Color plot corresponds to $H_z(\overrightarrow{r})$. Quiver plot shows the in-plane electric field components $E_\rho(\overrightarrow{r})$ and $E_\theta(\overrightarrow{r})$ vectorially.

each angular slice $\Delta\theta = 2\pi/m$ of the ABR defect mode, the direction of the in-plane field alternates between predominantly azimuthal and radial polarizations. Averaging over the entire radial defect mode, this complex polarization state will be indistinguishable from unpolarized light at a linear polarizer, thus explaining the polarization plot in Fig. 5.6(a). However, slight deviations from the ideal cylindrically symmetric structure, which can occur during the electron beam lithography fabrication step for example, may cause departures from the theoretically predicted modal field profiles and polarization state. For example, a slight ellipticity could cause enhanced output coupling of light linearly polarized along the long axis of the distorted ABR microcavity [118, 119]. Therefore, the partially polarized emission observed from modes belonging to the second group, as shown in Fig. 5.6(b), suggests a small degree of spatially localized emission of linearly polarized light, superimposed upon a weaker unpolarized background, and is attributed to fabrication errors that break the radial symmetry of the device.

5.3.5 ABR laser linewidth broadening

The spectra in Fig. 5.4(b) show that the FWHM linewidths $\Delta\lambda_{laser}$ of the various ABR lasing modes are in the range of 2-5 nm, with wider linewidths occurring for larger values of the incident pump power. With typical linewidths for standard commercial edge emitting Fabry-Perot semiconductor lasers being on the order of $\Delta\lambda_{laser} \sim 1$ pm (below the resolution limit of the OSA; also $\Delta\nu_{laser} \sim 100$ MHz), it is interesting to examine the possible factors contributing to the broad observed linewidth for the ABR laser.

First, the relationship between the linewidth and the cavity Q is illustrated by the expression for the modified Schawlow-Townes linewidth, including the broadening factor $(1 + \alpha^2)$ found to be important in semiconductor lasers [120, 121]. Stated in

terms of frequency, the laser linewidth $\Delta\nu_{laser}$ is given by

$$\begin{aligned}\Delta\nu_{laser} &= \frac{2\pi h\nu_0(\Delta\nu_{FWHM})^2}{P_0}\frac{N_2}{N_2-N_1}(1+\alpha^2) \\ &= \frac{2\pi h\nu_0^3}{Q^2P_0}\frac{N_2}{N_2-N_1}(1+\alpha^2),\end{aligned} \tag{5.3}$$

where ν_0 is the laser frequency, $\Delta\nu_{FWHM}$ is the linewidth of the passive cavity resonance, P_0 is the power coupled out of the cavity, and N_1 and N_2 are respectively the total number of atoms in the lower and upper laser levels. The quantity α is known as the linewidth enhancement factor, and is defined as the ratio of the differential change in the real and imaginary parts of the complex refractive index $n = n' - in''$, giving $\alpha = \Delta n'/\Delta n''$. Equation 5.3 predicts that the linewidth scales inversely with the square of the cold-cavity Q, making the quality factor a critical parameter for the realization of narrow linewidth laser sources.

Since we do not necessarily have reliable estimates for the Q or the output power P_0, it is more convenient to use a different form of Eq. 5.3, given by

$$\Delta\nu_{laser} = \frac{R}{4\pi\overline{n}_p}(1+\alpha^2) = \frac{R}{4\pi\rho_p V_m}(1+\alpha^2), \tag{5.4}$$

where R is the average spontaneous emission rate, $\overline{n}_p$ is the average number of photons in the lasing mode, ρ_p is the average photon density, and V_m is the cavity mode volume. The above expression can be used to facilitate the comparison of ABR and edge emitting laser linewidths on the basis of their mode volume. Assuming similar spontaneous emission rates, photon densities, and chirp parameters for each type of resonator, an order-of-magnitude estimate for the ABR laser linewidth $\Delta\nu_{laser,ABR}$ is given by

$$\Delta\nu_{laser,ABR} = \Delta\nu_{laser,FP}\frac{V_{m,FP}}{V_{m,ABR}}, \tag{5.5}$$

where $\Delta\nu_{laser,FP}$ is the linewidth of the edge emitting Fabry-Perot laser, and $V_{m,FP}$ and $V_{m,ABR}$ are the mode volumes of the Fabry-Perot and ABR geometries, respectively. As mentioned above, edge emitting semiconductor lasers operating continuous

wave typically have fundamental linewidths on the order of 100 MHz [122,123]. While the mode volume for a typical Fabry-Perot mode is on the order of several thousand cubic wavelengths in the semiconductor material ($V_{m,FP} \sim 10^3(\lambda/n)^3$), the mode volume for a radial defect ABR mode is much smaller, on the order of several tens of cubic wavelengths ($V_{m,ABR} \sim 10(\lambda/n)^3$). Therefore, the number of photons in the ABR mode is much smaller than that for the edge emitter, and broader linewidth of $\Delta\nu_{laser,ABR} \sim 10$ GHz can be expected. At wavelengths near 1.55 μm, where a spectral bandwidth of 1 nm converts to a frequency bandwidth of 125 GHz, the estimated linewidth translates to $\Delta\lambda_{laser} \sim 0.08$ nm. However, in comparison with the measured ABR laser linewidths, the above estimation falls short by a factor of ~25-60.

The discrepancy between the observed and measured linewidths can be accounted for by additional sources of broadening induced by the pulsed manner in which the ABR devices are excited. For most semiconductor lasers, the fundamental linewidth originates predominantly from the term multiplying α^2, which describes the coupling of the carrier density to the cavity field's amplitude and phase fluctuations due to spontaneous emission events. The expressions for the laser linewidth in Eqs. 5.3-5.4 were derived assuming steady state operating conditions, where spontaneous emission and the resulting carrier density fluctuations amount to only a small signal. However, the use of extremely short pulses approximately 100 fs in duration for optical excitation naturally prohibits laser action from reaching steady state operation. Typical semiconductor lasers require on the order of several nanoseconds for turn-on transients in the injected carrier density and cavity power to stabilize [124]. Therefore, the linewidth estimates given above cannot be expected to hold under such dynamic large-signal excitation conditions, but can at best be used to predict the fundamental ABR laser linewidth which would be observed if the device were excited continuous wave, or at least with longer pulses on the order of 100 ns - 1 μs.

Nevertheless, the enhanced broadening observed in the ABR laser linewidth is also likely due to the dynamic coupling of the free carrier density to the field's amplitude and phase during the transient excitation and emission occurring with each incident

pump pulse. A large density of electron-hole pairs is photogenerated within the semiconductor membrane upon absorption of a pump pulse. When sufficient carriers have diffused or been swept into the QWs to reach the threshold gain condition, the laser will turn on. At this point, the density of free carriers within the QWs is rapidly depleted as the stimulated power in the cavity grows. Eventually the carrier density will be reduced to the point that the ABR laser pulse will cease. The depletion of the carrier density results in an increase of the semiconductor refractive index during the ABR laser pulse. This increase in refractive index in turn chirps the optical carrier to longer wavelengths throughout the duration of the pulse, contributing to the observed degree of linewidth broadening.

There are two mechanisms contributing to the carrier dependent refractive index, these being free carrier plasma effects [111], and band-filling effects [109, 110], which result from the shift in the semiconductor bandgap with carrier concentration, and which change the refractive index through the Kramers-Kronig relations. These mechanisms have been used to explain similar laser linewidth broadening observed upon the onset of noise-induced self-pulsation in edge emitting semiconductor lasers operating under cw electrical excitation conditions [125, 126]. Asymmetric lineshapes for which the peaks were skewed towards the red end of the spectrum were observed for these pulsating lasers, and are very similar in appearance to those shown for the radial defect ABR lasers in Fig. 5.4(b). Although the excitation conditions differ from those used here for ABR lasers, the dynamic mechanisms responsible for linewidth broadening should be similar in both cases.

5.3.6 Images of infrared near field emission profiles

Additional information regarding the optical characteristics of ABR defect resonators can obtained by imaging the near field standing wave intensity profile at the ABR surface. The vertically collected emission can be focused onto an IR vidicon camera for this purpose, as shown in Fig. 5.1. Not shown in Fig. 5.1 are a double-side polished Si wafer and a long-pass filter transparent for wavelengths longer than 1500 nm, which

were placed in the infrared PL collection path and used to filter the residual 890 nm pump beam transmitted through the ABR semiconductor membrane. When pumped above laser threshold, efficient vertical emission induced by the mixed-order grating, in addition to surface scattering, permits imaging of the structure's lasing spatial mode profiles. For example, Figs. 5.8(b)-(c) contain a pair of IR images obtained from two ABR devices with slightly different designs, each having a geometry similar to the ABR device in Fig. 5.8(a). Each of the devices shown has a fifth-order defect layer, i.e. an "effective" $5\lambda/2n$ wide. Specifically, the devices producing the images in Figs. 5.8(b)-(c) were designed for operation at $\lambda = 1550$ nm with $m = 9$ and $m = 7$, respectively. The superimposed outlines, corresponding to the edges of the semiconductor rings in each structure, show that the $m = 9$ design has a slightly larger defect radius that that of the $m = 7$ design.

Using the IR images, several important observations can be made. First, the emission is localized within an annular region coincident with the wide radial defect layer. In addition, the emission intensity decays rapidly within the first two periods of the cylindrical Bragg reflectors on either side of the defect. Both these features occur as expected from numerical calculations of ABR defect mode profiles, as discussed in Chapter 3. Furthermore, the spatial emission profiles show multiple lobes of high intensity around the circumference of the defect layer, separated by regions of reduced emission. Although some estimation is involved, the emission pattern appears to possess 14 bright lobes in Fig. 5.8(b), and 12 bright lobes in Fig. 5.8(c), suggesting that the patterns correspond to modes with azimuthal numbers of $m = 7$ and $m = 6$, respectively. The differences between the designed and observed m numbers can be due to uncertainty and/or dispersion in the membrane slab effective index n_{eff} used in the design calculations, or deviations of the defect radius from the desired nominal value occurring during the ABR fabrication process. The observed azimuthal numbers $m = 7$ and $m = 6$ correspond to azimuthal effective indexes $n_{eff,\theta}$ of 0.21 and 0.19, respectively, as given by $n_{eff,\theta} = m\lambda/2\pi R_{eff}$, where R_{eff} is the effective radius at which the mode travels. The effective radii were taken as 8.3 μm and 7.7 μm for the devices in Fig. 5.8(b) and Fig. 5.8(c), respectively. These values of $n_{eff,\theta}$ are lower

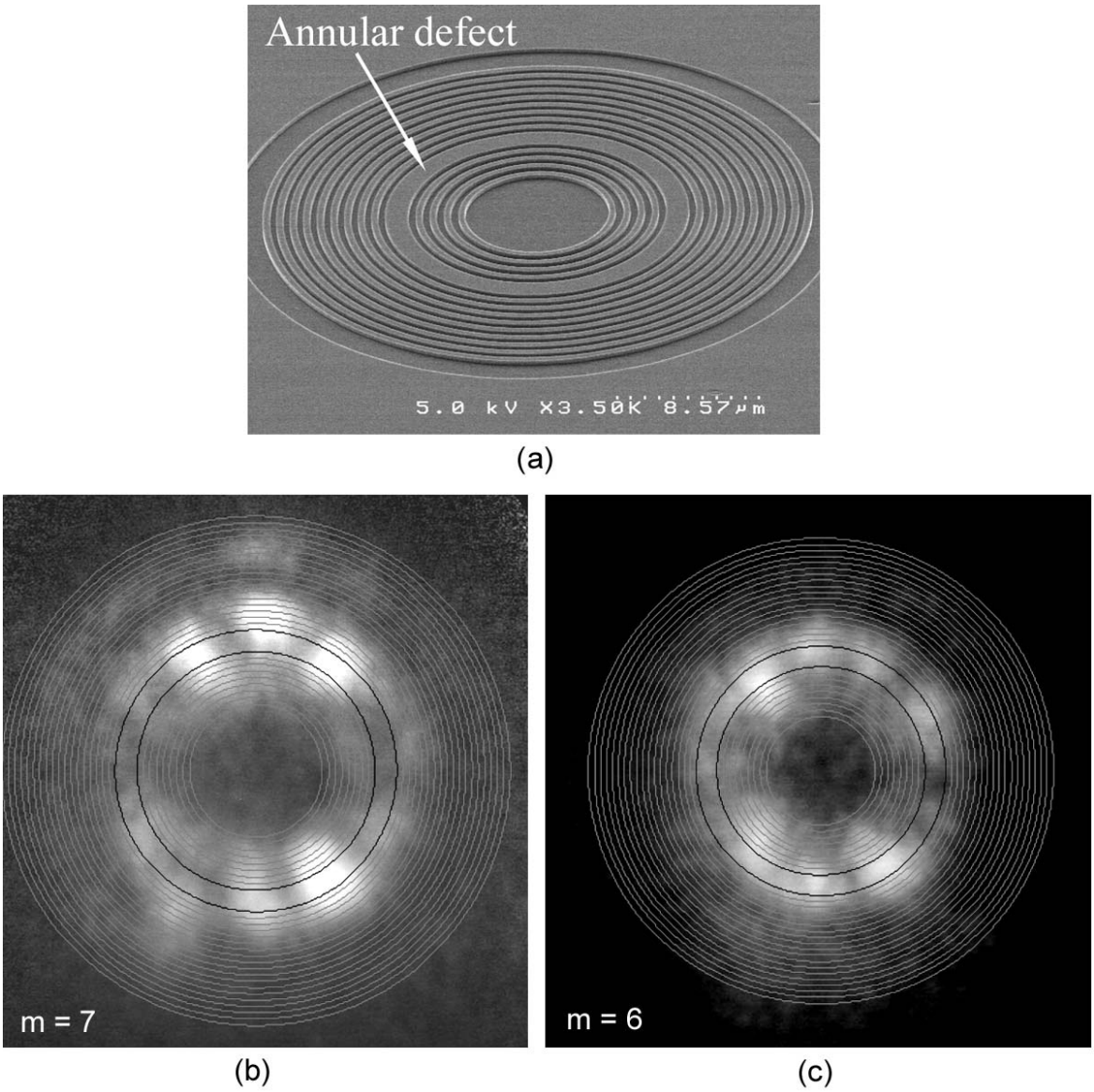

Figure 5.8: (a) SEM image of an ABR having a higher order defect with an "effective" width of $5\lambda/2n$. The device geometry shown here is representative of the devices producing the subsequent IR images. The IR near field emission patterns corresponding to $m = 7$ and $m = 6$ ABR defect modes are shown in (b) and (c), respectively, superimposed against outlines locating the edges of the semiconductor rings.

than the refractive index of air as well as the NOA 73 adhesive layer forming the lower cladding layer ($n = 1.56$), confirming that the IR patterns observed are due to modes guided by Bragg reflection.

The slow azimuthal modulation of the IR pattern intensity, particularly visible in Fig. 5.8(b) where the lobes possess higher intensity in two main clusters along the y-axis of the image, is likely due to some small ellipticity in the ideally circular ABR structure. Such ellipticity could lead to slightly different widths or spacings of the high and low index layers in the Bragg reflectors along the x and y directions, resulting in different in-plane defect mode confinement efficiency, vertical diffraction angle, and vertical collection efficiency along each of these axes [48,118]. These effects can combine to produce enhanced directional emission from ABR regions with higher curvature, giving rise to the intensity non-uniformities of the sort seen in Fig. 5.8(b).

Although ABR devices with a first order defect layer such as that shown in Fig. 5.2 were found to produce IR emission patterns with similar features, the images themselves were not as clear due to a poor signal-to-noise ratio. Therefore, the images from the higher order defect ABR microcavities are shown here for the purpose of illustrating the optical confinement within the defect layer.

5.4 Comparison of ABR lasing spectra with FDTD simulations

In Section 5.3, the above threshold lasing spectra from ABR defect lasers was shown to be composed of multiple modes. Measurements on a number of similar ABR devices illustrated a common trend; as the optical pump power was increased, a larger number of modes reached laser threshold. For pump powers greater than approximately 3 mW (roughly three times the threshold pump power of $\sim$1 mW), the lasing spectra typically became quite complex, as is illustrated in the experimental spectrum in Fig. 5.9(a), for which the incident pump power was $\sim$3.2 mW. The ABR device producing this spectrum was similar to that discussed in Section 5.3,

having a first-order semiconductor defect, and mixed-order Bragg reflectors composed of second-order high-index and first-order low-index layers. However, the Norland optical adhesive filling the low index layers was not removed in the present case, giving these layers a refractive index of $n = 1.56$ rather than $n = 1$.

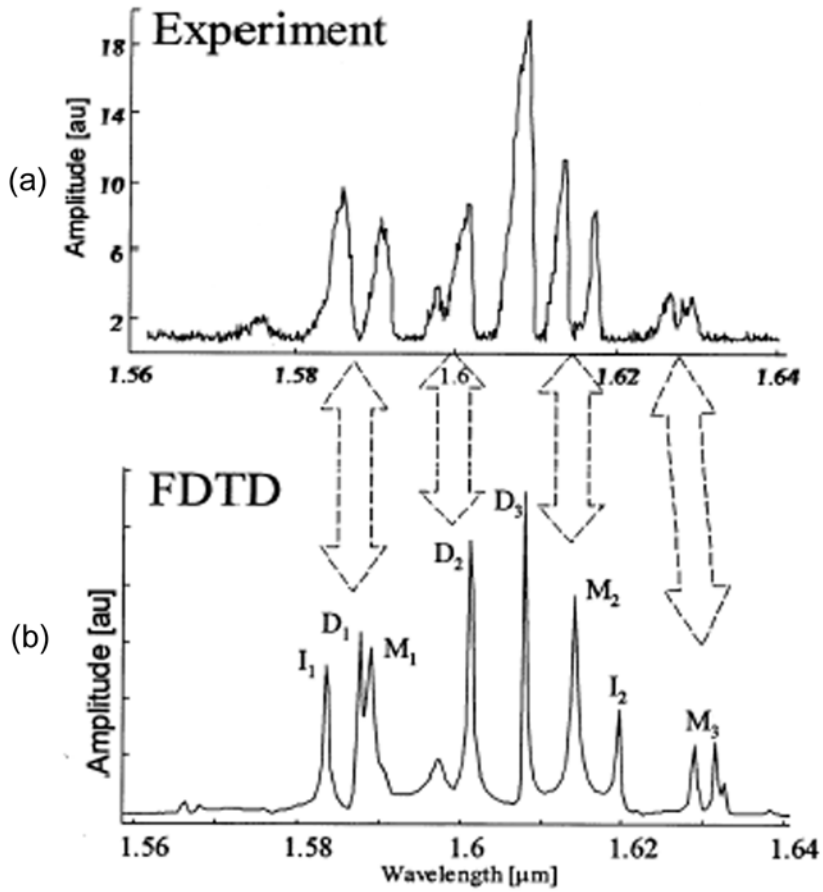

Figure 5.9: Comparison of experimental laser spectrum at $P_p \sim 3.2$ mW (a) with numerically derived FDTD spectrum (b). Modes labeled D are confined within the ABR defect. Modes labeled I are confined within one of the semiconductor rings of the inner Bragg reflector. The modes labeled M are not confined to a single ring, but overlap with multiple rings.

In an effort to explain the complicated spectral characteristics shown in Fig. 5.9(a), the ABR device was modeled using a finite-difference time-domain (FDTD) numerical simulation tool [127,128]. By exciting the simulated ABR structure with a very short temporal pulse, all optical modes within a broad frequency band about the

center frequency of the pulse were excited. Time evolution of this initial excitation allows non-resonant frequency components to dissipate or "leak" from the ABR structure, while the resonant frequencies of interest continue to propagate within the ABR. Subsequent analysis of the Fourier spectrum of the resonant optical fields reveals a series of spectral peaks corresponding to the resonant wavelengths of the structure, as shown in Fig. 5.9(b) [129].

Comparison of Figs. 5.9(a)-(b) illustrates that the modal spectrum computed by FDTD agrees quite well with the experimental spectrum, both in terms of the resonant wavelengths as well as their relative amplitudes. As a guide to the eye, common groups of resonant modes are connected by dashed arrows between the two spectra. However, the wavelength axis of the FDTD spectrum is slightly "stretched" with respect to that of the experimental spectrum. This effect can be attributed to the fact that the FDTD simulation does not take into account the material dispersion of the ABR semiconductor membrane or the Norland optical adhesive. The material contribution to the group index is therefore not captured by the FDTD simulation, leading to a slightly larger wavelength spacing between the resonant modes.

The FDTD spatial field profiles corresponding to the resonant modes were found to be well classified into three separate types, labeled by the letters D, I, and M in Fig. 5.9(b). The modes belonging to the D class are confined within the ABR defect layer, as expected from the device design. The subscripts D_1, D_2, and D_3 label defect-confined modes with different azimuthal number m. The modes of class I are confined within the semiconductor ring closest to the radial defect within the inner Bragg reflector. These modes are in fact guided by total internal reflection, and are supported because of the use of wider second-order semiconductor layers within the mixed-order Bragg mirror design. The modes belonging to class M are not localized to a single layer as are the D and I modes, but are more broadly distributed over several grating periods, having significant amplitude within both the high and low-index layers.

5.5 Effects of electron beam lithography process variations and lithographic tuning of ABR lasers

The lasing wavelength of the ABR radial defect modes is very sensitive to the modal effective index, or equivalently, the optical path length traversed by a given mode per revolution around the cylindrical structure. One means by which the ABR lasing wavelength may be controlled is by "lithographic tuning" [130,131], for example, fine tuning of the optical path length via the dimensions of the annular Bragg reflectors and the defect layer, during the initial ABR transfer matrix design process. However, additional sources of lithographic tuning can originate from the device fabrication process itself, particularly during electron beam lithography [98]. For a given thickness of PMMA resist, there exists a finite range of electron doses for which the PMMA resist is fully exposed, leaving no residues on the substrate, and does not yet suffer from a reduction in contrast due to overexposure. Within this range of doses, however, the lateral pattern dimensions may experience subtle changes from the nominal design on the order of only several nanometers. Such small deviations can be difficult to detect, even using scanning electron microscopy. Nevertheless, the optical properties of the resulting ABR structure, specifically the lasing wavelengths, provide a sensitive probe of lithographic process variations, and can give an indication of the electron beam lithography process latitude [132].

A series of ABR devices were prepared to evaluate the effects of varying the electron dose D applied during electron beam lithography. These devices all had first order radial defects and mixed order cylindrical Bragg reflectors, very similar to the device shown in Fig. 5.2. The overall range of doses for which the PMMA patterns were adequately exposed was experimentally determined to be 600-725 μC/cm^2. Four different doses interior to this range, specifically 625, 650, 675, and 700 μC/cm^2, were investigated.

Near infrared spectra obtained while pumping this set of devices above laser threshold are shown in Fig. 5.10. The pump objective lens was defocused such that the pump spot diameter was $\sim$16 μm, in order to ensure reasonable overlap between

the pump and the ABR defect. The time averaged pump power incident upon each device was 1.4 mW. While devices given the same dose exhibited almost identical spectra, comparison of the spectra from devices with D = 700 μC/cm^2, 675 μC/cm^2, and 650 μC/cm^2 shows successive shifts of the lasing modes to longer wavelengths as the electron dose decreases. The position of a pair of closely spaced modes in each spectrum was used to track the redshift, as indicated by the arrows. The wavelengths of these modes were 1581 nm/1589 nm for D = 700 μC/cm^2, 1588 nm/1596 nm for D = 675 μC/cm^2, and 1608 nm/1615 nm for D = 650 μC/cm^2. The observed redshifts are approximately 7 nm between D = 700 μC/cm^2 and 675 μC/cm^2, and 20 nm between D = 675 μC/cm^2 and 650 μC/cm^2.

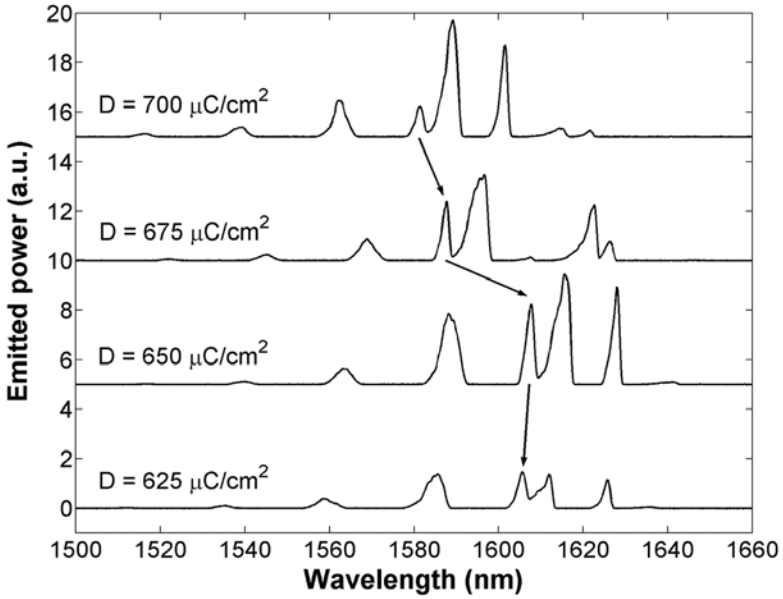

Figure 5.10: Illustration of lithographic process variation effects upon ABR lasing mode wavelengths. Emission spectra shown were taken from four different ABR lasers fabricated with varying electron dose D. The arrows follow the spectral redshift of a particular pair of optical modes resulting from the increasing semiconductor filling fraction with decreasing electron dose, for D = 700, 675, and 650 μC/cm^2. The slight blueshift observed for the D = 625 μC/cm^2 spectrum departs from this trend. Optical pump power was 1.4 mW for all spectra.

The redshift can be understood by noting that as the exposure dose is decreased, the widths of the PMMA rings remaining after development of the ABR pattern

(Fig. 4.6) are slightly increased, ultimately resulting in wider semiconductor rings in the Bragg reflectors and ABR defect. The resulting increase in the semiconductor filling fraction raises the effective index n_{eff} (and increases the optical path length) of the guided optical modes, which in turn causes a redshift. The percent change in n_{eff} and optical path length is estimated to be 0.44% between D = 700 μC/cm^2 and 675 μC/cm^2, and 1.26% between D = 675 μC/cm^2 and 650 μC/cm^2. In contrast, the spectrum from the device patterned with D = 625 μC/cm^2, in which the two closely spaced modes were located at 1605 nm and 1612 nm, appears to be slightly blueshifted with respect to the D = 650 μC/cm^2 spectrum. This departure from the trend observed for the larger electron doses is likely due to some additional non-systematic source of fabrication process drift.

The numerically estimated shift in the resonance wavelength as a function of the lithography-induced adjustment in the width of each semiconductor ring in the ABR structure is plotted in Fig. 5.11. The nominal resonance wavelength at zero width adjustment was taken to be 1580 nm. Dispersion of the refractive index has been neglected. The wavelength shift is linear in the layer width adjustment, and the slope of the relationship indicates an expected shift of 5.79 nm per 1 nm change in the layer width. As expected, a very small change in the ABR device dimensions (in fact smaller than both the pattern fracture resolution limit of the electron beam lithography and the sidewall roughness after reactive ion etching), results in a significant change in the operating wavelength. Using Fig. 5.11, it is estimated that the semiconductor ring widths across the ABR structure have changed by less than 4.7 nm each, within the dose range from 650 - 700 μC/cm^2.

Plots of the integrated ABR emission versus optical pump power for each of the four devices are given in the L-L curves of Fig. 5.12. As the electron dose is decreased, a decrease in the pump power P_{th} required to reach laser threshold is observed. Threshold occurred at P_{th} = 0.39 mW, 0.33 mW, and 0.30 mW for D = 700 μC/cm^2, 675 μC/cm^2, and 650 μC/cm^2 respectively. The dosage-dependent increase in the semiconductor filling fraction also results in a larger overlap of the ABR modes with the amplifying quantum wells. The corresponding increase in the optical gain

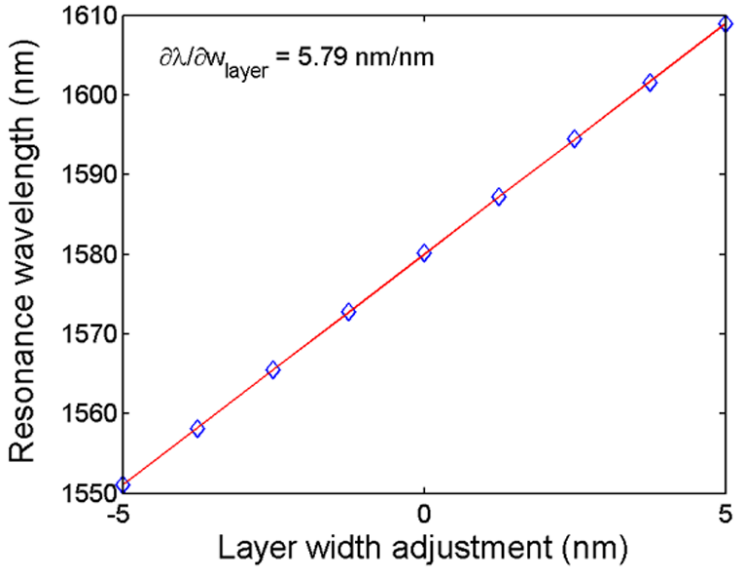

Figure 5.11: Numerically estimated resonance wavelength shift versus electron beam lithography dose induced adjustment in the semiconductor ring layer widths throughout the ABR structure.

experienced by the ABR modes gives rise to a reduction in threshold pump power. Again, the L-L curve for the device patterned with D = 625 μC/cm^2 departs from the observed trend, demonstrating a larger threshold pump power of 0.36 mW, and also having poor slope efficiency above threshold compared with devices given a larger dose. The higher value of P_{th} and the degraded efficiency lend further evidence for the degradation of this device by a non-systematic fabrication error.

The large sensitivity of the operating wavelength to small changes in the modal effective index, as observed during the course of lithographic process variations, suggests that ABR devices can be used as high responsivity optical sensors. For example, in cases where the sensing mechanism involves a change in the refractive index of the local medium surrounding and/or infiltrating the ABR, the spectral shift associated with the change in the modal effective index can be monitored, leading to applications in chemical and biological sensing. Making use of ABR devices in such applications will be the subject of Chapter 8.

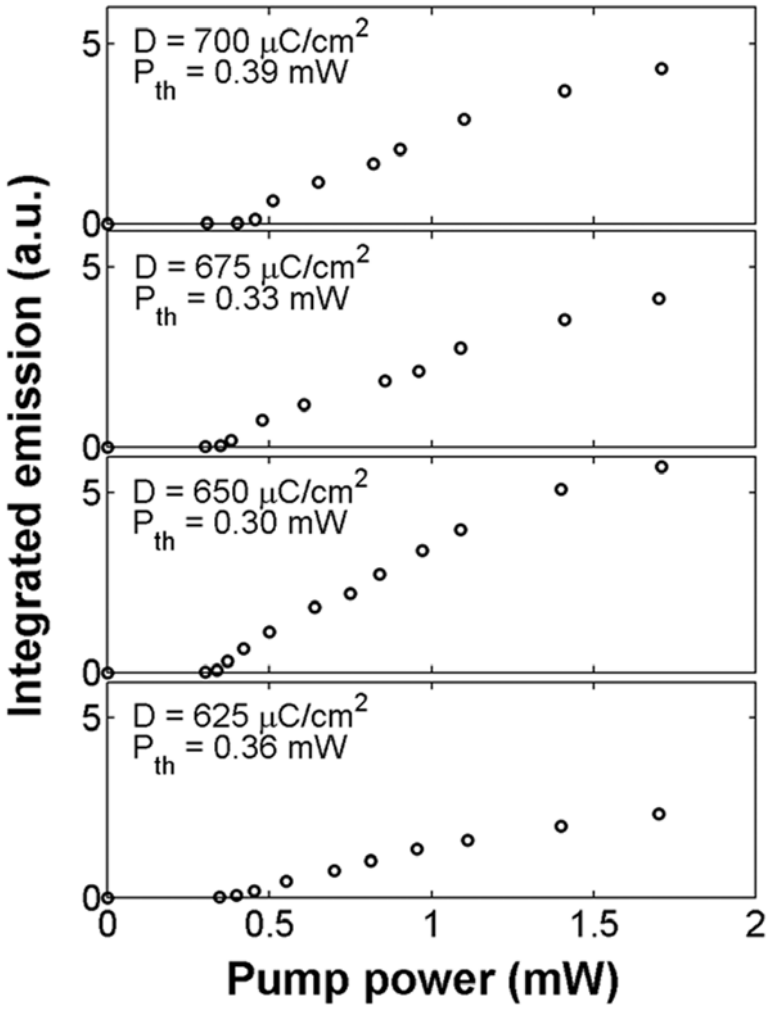

Figure 5.12: L-L plots from four ABR lasers fabricated with varying electron dose D. The increase in modal gain with decreasing dose leads to sucessively lower threshold pump powers P_{th} for D = 700, 675, and 650 μC/cm^2. The higher threshold pump power and poor efficiency of the D = 625 μC/cm^2 device departs from this trend.

5.6 Circular nanocavity lasers with ultra-small mode volume

The radial defect ABR microcavity geometry discussed above was shown to lase at multiple frequencies above threshold. However, for many applications, such as telecommunications and spectroscopy, single mode lasers are far more desirable. As illustrated in Chapter 3, a radial defect ABR structure designed to support a mode with azimuthal number m at a nominal wavelength of λ_m can also support several other modes with adjacent azimuthal numbers $..., m-1, m+1, ...$, at wavelengths near λ_m. Owing to the relative similarity of the spatial field profiles of these modes, they are all likely to possess similar modal gain within the active InGaAsP QW membrane, and thus have similar laser thresholds, provided that these modes have resonant wavelengths lying within the gain spectrum.

In general, single mode laser oscillation can be obtained by designing the microcavity such that the free spectral range between the resonant wavelengths of the designed mode and the nearest adjacent mode is large enough to push all but the designed mode outside of the semiconductor gain bandwidth. This goal may be accomplished by substantially reducing the size, or optical path length, of the resonant cavity in which the light is guided, for example, by reducing the radius of the ABR defect layer. Continuing to make use of cylindrical Bragg reflectors for radial optical confinement, the limit of this approach leads to the geometry shown in the SEM image of Fig. 5.13(a), in which the resonant cavity is no longer an annular defect, but rather a small pillar or disk placed at the center of a radial Bragg mirror [133, 134]. This Bragg pillar geometry can be used to realize compact sub-micron microcavities with very small mode volume, particularly when they are designed for the $m = 0$ cylindrical mode. Whereas the radial defect ABR modes with $m \neq 0$ considered previously propagate azimuthally and are doubly degenerate with $\pm m$ modes propagating clockwise and counter-clockwise, the $m = 0$ mode supported by the Bragg pillar structure is non-degenerate, and has the form of a radial standing wave with maximum intensity located at the center of the device.

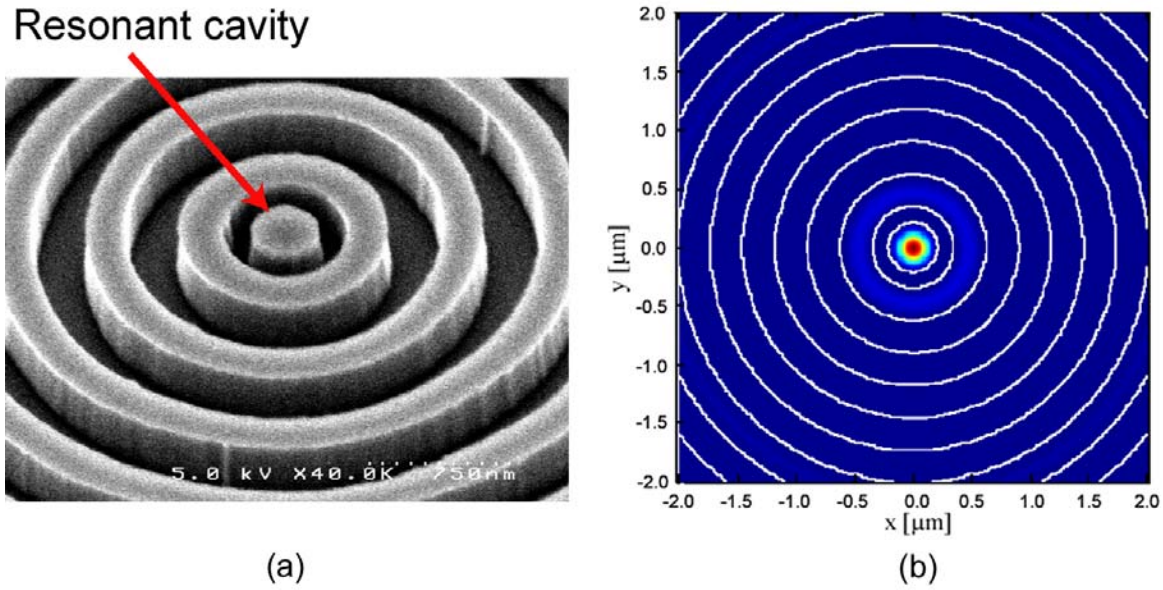

Figure 5.13: (a) SEM image of a Bragg pillar resonator designed to support the $m = 0$ mode. The cavity is composed of a 400 nm diameter central disk surrounded by a cylindrical Bragg reflector. (b) Calculated modal intensity pattern of the resonator shown in (a). The intensity is highly confined within the central pillar, as illustrated by the superimposed Bragg reflector outline.

The design of the Bragg pillar resonator shown in Fig. 5.13(a) was performed using a coupled mode approach for cylindrical structures [52, 135]. In this technique, the inward and outward propagating wave solutions in cylindrical coordinates (Hankel functions of the first and second kind, $H_m^{(1,2)}(k_0 n_{eff}\rho)$), are coupled by a radial perturbation profile $\Delta\varepsilon(\rho)$ which describes the Bragg reflector. For the structure to support a resonant TE mode with azimuthal number m, the radius ρ_0 of the central pillar must fulfil the condition

$$J_m(k_0 n_{eff}\rho_0) = 0, \tag{5.6}$$

where $k_0 = 2\pi/\lambda$ is the wavenumber in free space at the resonant wavelength. In addition, the grating profile $\Delta\varepsilon(\rho)$ must satisfy

$$\Delta\varepsilon(\rho) = \begin{cases} -2\,|\alpha| \\ 0 \end{cases} \quad \text{for} \quad \begin{cases} \sin\left\{2\text{phase}\left[H_m^{(1)}(k_0 n_{eff}\rho)\right]\right\} < 0 \\ \sin\left\{2\text{phase}\left[H_m^{(1)}(k_0 n_{eff}\rho)\right]\right\} \geq 0 \end{cases}, \tag{5.7}$$

where α is a perturbation strength parameter related to the grating contrast. By Eq. 5.6, the smallest Bragg pillar resonator having $m = 0$ can be designed by choosing the pillar radius to coincide with the first zero of the Bessel function $J_0(k_0 n_{eff}\rho_0)$. Using a slab effective index $n_{eff} = 2.8$ and a wavelength $\lambda = 1550$ nm gives a pillar radius of approximately 200 nm for the structure in Fig. 5.13(a). The external Bragg reflector consisted of 35 quasi-periods of the mixed-order optimally chirped design similar to those used in the radial defect ABR devices discussed previously, and was fabricated using the active InGaAsP QW membrane by the same procedure as outlined in Chapter 4.

Figure 5.13(b) contains a theoretical plot of the $m = 0$ modal intensity profile. The superimposed outlines, corresponding to the edges of the semiconductor rings in the structure, illustrate that the modal intensity is confined almost completely within the 400 nm diameter central pillar. A compact mode volume V_m of 0.213 $(\lambda/n)^3$, or 0.024 μm^3, is estimated for this $m = 0$ mode, which is only 1.75 times the theoretically

predicted limit of a cubic half-wavelength. The mode volume is defined as

$$V_m = \frac{\int \varepsilon(\overrightarrow{r}) \left|E(\overrightarrow{r})\right|^2 d\overrightarrow{r}}{\left[\varepsilon(\overrightarrow{r}) \left|E(\overrightarrow{r})\right|^2\right]_{\max}}.$$

In comparison with several demonstrated photonic crystal defect cavity designs [83, 136], the Bragg pillar mode volume is approximately 30% smaller. This feature again illustrates one of the intrinsic advantages of ABR microcavity geometries. On one hand, photonic crystal defect microcavities require extensive numerical simulation to investigate the effects of a large space of parameters upon the modal characteristics. In contrast, the cylindrical symmetry of Bragg pillar devices permits an analytical description of their electromagnetic properties, enabling straightforward evaluation of the optimum cavity and Bragg reflector configuration for obtaining ultra-small mode volume. The estimated mode volume could be further reduced by using a more symmetric scheme for vertical optical confinement, i.e. using material of the same refractive index (preferably less than the current $n = 1.56$ NOA 73 polymer) both above and below the InGaAsP membrane.

The Bragg pillar nanocavity in Fig. 5.13(a) was excited by pulsed optical pumping as described previously. The pump beam was focused to a spot $\sim$3 μm in diameter and was aligned with the central disk. The L-L curve in Fig. 5.14(a) shows that laser threshold was reached at an incident pump power of $P_{th} \sim 900$ μW. Several spectra measured as a function of pump power are depicted in Fig. 5.14(b). As anticipated, the emission consists primarily of a single mode at $\lambda = 1561$ nm, very close to the design wavelength. At higher pump levels of approximately $1.5 \times P_{th}$, two additional low-intensity peaks appear in the spectra at longer wavelengths near 1585 nm. These additional modes are attributed to emission from the surrounding cylindrical Bragg grating, which is optically pumped through overlap with the tails of the pump spot. This conclusion was reached by correlating the observed spectral features with both the diameter and position of the pump spot with respect to the central pillar of current device [66].

Although it was pointed out for the radial defect ABR microcavities above that

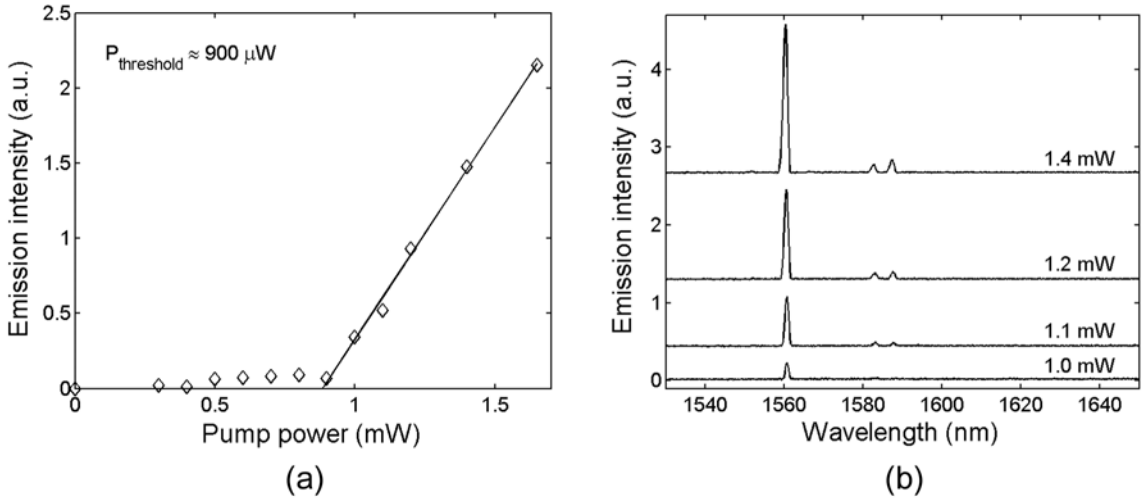

Figure 5.14: (a) L-L curve of integrated Bragg pillar nanocavity emission vs. pump power, showing laser threshold at $P_{th} \sim 900$ μW. (b) Optical spectra measured above laser threshold. Spectra are vertically offset to illustrate the effects of increasing pump power.

the individual second-order high-index semiconductor layers Bragg gratings are sufficiently wide to support undesirable index guided microring modes, in the case of the Bragg pillar cavity, the net reduction in the size of the cavity acts to suppress these modes. By shrinking the radii of the high-index layers of the cylindrical Bragg reflector to correctly surround the $m = 0$ central pillar, the radiative bend and scattering losses for TIR microring modes within the smallest rings will be strongly increased, resulting in lower Q factors and much higher thresholds for laser oscillation. Since the pump spot only overlaps with high-index rings having very small radii, the emission from these undesirable microring modes is strongly reduced.

Chapter 6

Design and fabrication of InGaAsP-InP integrated planar coupled waveguide-resonator systems

6.1 Introduction

This chapter presents a discussion of several aspects relevant to the design and realization of InGaAsP-InP coupled waveguide-resonator systems. First, the numerical finite difference (FD) technique for solving the Helmholtz equation will be described, with applications to computing the transverse electromagnetic mode profiles and modal propagation constants of 2D dielectric waveguides. Next, the design of a particular type optical coupler device, known as a multimode interference (MMI) coupler, will be outlined, and some examples of the theoretically predicted coupler performance will be illustrated. Finally, a fabrication process for electrically actuated InGaAsP-InP planar photonic integrated circuits will be described. The fabrication process and design techniques for optical waveguides and MMI couplers discussed in this chapter are applied to demonstrate a novel InGaAsP-InP thermooptic switch geometry in Chapter 7.

6.2 Numerical finite-difference eigenmode solver

The design of functional photonic devices depends heavily upon manipulation of the manner in which light propagates along various types of waveguide structures, and thus, accurate techniques for evaluating the electromagnetic properties of such structures are required. Assuming translational invariance along the axis of the waveguide, taken as the z-axis, the dielectric properties (refractive index, material loss/gain, etc.) of the waveguide cross-section in the $x-y$ plane will determine the relevant parameters describing the waveguide. These include, for example, the optical mode profiles, propagation constants, polarizations, and cut-off conditions. For simple slab waveguides in which the cross-section only varies along one axis, say, the y-axis, straightforward analytical methods for finding the eigenmodes and eigenfrequencies exist [65]. Furthermore, by using the effective index approximation [69], it is also possible to generalize the one-dimensional slab waveguide solutions to structures with two-dimensional optical confinement, along both the x- and y-axes. The effective index approach is most accurate for waveguides having low refractive index contrast between the core and cladding regions, and much larger spatial extent of the waveguide core along the x-axis than the y-axis, or vice-versa. Analytical methods for finding the modes of such structures often solve the scalar Helmholtz equation within each of the homogeneous, isotropic dielectric layers comprising the waveguide, and apply the appropriate boundary conditions for the electric and magnetic fields along the dielectric interfaces to match the solutions within each layer.

However, for more complicated two-dimensional waveguide cross-sections, particularly those with high index contrast such as the channel waveguide shown in Fig. 6.1, the approximations used in the application of purely analytical methods break down. In these cases, numerical methods must be applied to obtain the most accurate predictions of the waveguide modal properties. Several numerical techniques have been applied to the problem of waveguides with arbitrary refractive index profiles, with two of the most common being the finite element [137] and finite difference [90, 138] methods. Finite element methods do not directly solve the Helmholtz equation, but

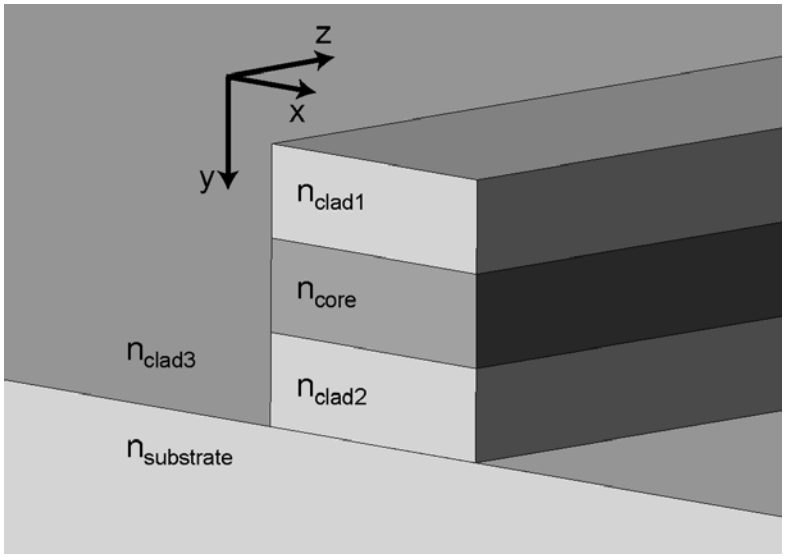

Figure 6.1: Cross-section of a typical channel waveguide structure, labeling refractive index in each region/layer.

rather make use of the variational principle to minimize a functional derived from the Helmholtz equation. The finite difference method approaches the problem in a more direct fashion, by discretizing the waveguide cross-section over a fine grid, and approximating the partial derivatives in the Helmholtz equation by numerical difference equations. Ultimately, this approach leads to a set of algebraic equations which is cast in the form of a matrix eigenvalue problem. Standard numerical methods for finding the eigenvalues and eigenvectors of the matrix can then be applied [139].

6.2.1 Finite difference approximations

Consider a general continuous and smooth function of one variable $f(x)$. When numerical techniques are employed, the x-axis is discretized to take on the values $\{..., x_{i-1}, x_i, x_{i+1}, ...\}$, and the function $f(x)$ is represented by discrete values at these points, as shown in Fig. 6.2. Expanding $f(x_{i-1})$ and $f(x_{i+1})$ in Taylor series about

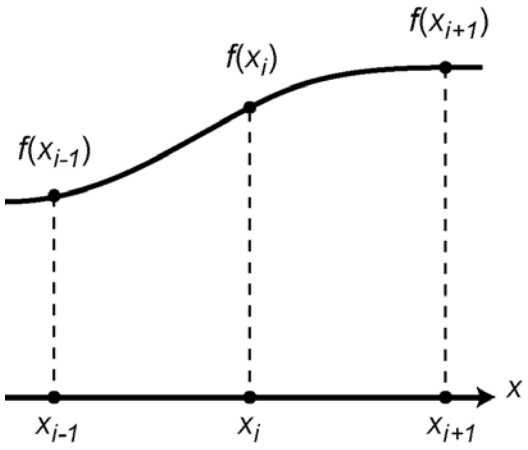

Figure 6.2: Discretization of a one-dimensional function $f(x)$, illustrating the finite difference method.

$x = x_i$ gives

$$\begin{aligned} f(x_{i-1}) &= f(x_i) - (x_i - x_{i-1})f^{(1)}(x_i) + \frac{(x_i - x_{i-1})^2}{2} f^{(2)}(x_i) \\ &\quad - \frac{(x_i - x_{i-1})^3}{6} f^{(3)}(x_i) + O((x_i - x_{i-1})^4) \qquad (6.1) \\ f(x_{i+1}) &= f(x_i) + (x_{i+1} - x_i)f^{(1)}(x_i) + \frac{(x_{i+1} - x_i)^2}{2} f^{(2)}(x_i) \\ &\quad + \frac{(x_{i+1} - x_i)^3}{6} f^{(3)}(x_i) + O((x_{i+1} - x_i)^4), \qquad (6.2) \end{aligned}$$

where $f^{(n)}(x)$ are the n^{th} derivatives with respect to x. Subtracting Eq. 6.1 from Eq. 6.2 and solving for the first derivative evaluated at x_i gives

$$f^{(1)}(x_i) = \frac{f(x_{i+1}) - f(x_{i-1})}{x_{i+1} - x_{i-1}} - \frac{x_{i+1} + x_{i-1} - 2x_i}{2} f^{(2)}(x_i) + O((x_{i+1} - x_i)^2). \qquad (6.3)$$

For the case of equidistant discretization, where $x_i - x_{i-1} = x_{i+1} - x_i = \Delta x$, the second term on the right hand side of Eq. 6.3 vanishes, and the central difference approximation for the first derivative results:

$$f^{(1)}(x_i) = \frac{f(x_{i+1}) - f(x_{i-1})}{2\Delta x} + O((\Delta x)^2). \qquad (6.4)$$

In the limit of $\Delta x \rightarrow 0$, Eq. 6.4 converges to the true first derivative of $f(x)$. Therefore, the numerical error associated with representing the derivative as a finite difference decreases as the grid spacing Δx becomes more fine. For non-equidistant discretization (i.e. $x_i - x_{i-1} \neq x_{i+1} - x_i$), the numerical errors become larger, being of $O(\Delta x)$, and thus a uniform grid is generally desirable. Following a similar procedure, the central difference approximation for the second derivative, assuming equidistant discretization, can be written as

$$f^{(2)}(x_i) = \frac{f(x_{i-1}) - 2f(x_i) + f(x_{i+1})}{(\Delta x)^2} + O((\Delta x)^2). \tag{6.5}$$

The finite difference approximations can take other forms aside from the central difference expressions above, for example, forward and backward differences. However, the central difference approximations are preferred for their smaller numerical error. For functions of several variables, partial derivatives can be approximated by generalizing the 1D approach above.

6.2.2 Semi-vectorial wave equations

In order to correctly capture the boundary conditions on the field components tangential and normal to a dielectric interface, the vectorial form of the Helmholtz equation must be numerically discretized. The vectorial Helmholtz equation for the electric field assumes that the dielectric permittivity $\varepsilon(\overrightarrow{r})$ varies spatially, and is given by

$$\nabla^2 \overrightarrow{E}(\overrightarrow{r}) + \nabla \left(\frac{\nabla \varepsilon_r(\overrightarrow{r})}{\varepsilon_r(\overrightarrow{r})} \cdot \overrightarrow{E}(\overrightarrow{r}) \right) + k_0^2 \varepsilon_r(\overrightarrow{r}) \overrightarrow{E}(\overrightarrow{r}) = 0, \tag{6.6}$$

where $\varepsilon_r(\overrightarrow{r}) = n^2(\overrightarrow{r})$ is the relative dielectric permittivity, k_0 is the wavenumber in free space, and a harmonic time-dependence of the form $\exp(i\omega t)$ has been assumed. In a uniform waveguide, we have $\partial \varepsilon_r(\overrightarrow{r})/\partial z = 0$. Taking a spatial dependence of the form $\exp(-i\beta z)$ along the z-axis allows the x and y components of Eq. 6.6 to be

expressed as

$$\frac{\partial^2 E_x}{\partial x^2} + \frac{\partial}{\partial x}\left(\frac{1}{\varepsilon_r}\frac{\partial \varepsilon_r}{\partial x}E_x\right) + \frac{\partial^2 E_x}{\partial y^2} + (k_0^2\varepsilon_r - \beta^2)E_x + \frac{\partial}{\partial x}\left(\frac{1}{\varepsilon_r}\frac{\partial \varepsilon_r}{\partial y}E_y\right) = 0 \quad (6.7)$$

$$\frac{\partial^2 E_y}{\partial x^2} + \frac{\partial^2 E_y}{\partial y^2} + \frac{\partial}{\partial y}\left(\frac{1}{\varepsilon_r}\frac{\partial \varepsilon_r}{\partial y}E_y\right) + (k_0^2\varepsilon_r - \beta^2)E_y + \frac{\partial}{\partial y}\left(\frac{1}{\varepsilon_r}\frac{\partial \varepsilon_r}{\partial x}E_x\right) = 0, \quad (6.8)$$

where the spatial dependence of all quantities has been suppressed for clarity. The last terms in Eqs. 6.7-6.8 represent coupling between the TE and TM modes typically associated with slab waveguides [65]. Therefore, the general solutions of the vectorial Helmholtz equations will be hybrid modes having six non-zero field components, i.e. E_x, E_y, E_z, H_x, H_y, and H_z.

However, in many cases the coupling terms are small and can be ignored, decoupling Eqs. 6.7-6.8 and making more efficient numerical solution possible. Assuming $E_y = 0$ or $E_x = 0$ leads to the semi-vectorial Helmholtz equations for the quasi-TE (principal field component E_x) and quasi-TM modes (principal field component E_y), respectively, given by

$$\frac{\partial^2 E_x}{\partial x^2} + \frac{\partial}{\partial x}\left(\frac{1}{\varepsilon_r}\frac{\partial \varepsilon_r}{\partial x}E_x\right) + \frac{\partial^2 E_x}{\partial y^2} + k_0^2\varepsilon_r E_x = \beta^2 E_x \quad (6.9)$$

$$\frac{\partial^2 E_y}{\partial x^2} + \frac{\partial^2 E_y}{\partial y^2} + \frac{\partial}{\partial y}\left(\frac{1}{\varepsilon_r}\frac{\partial \varepsilon_r}{\partial y}E_y\right) + k_0^2\varepsilon_r E_y = \beta^2 E_y. \quad (6.10)$$

Figure 6.3 illustrates the primary field components associated with the quasi-TE and quasi-TM modes of a typical channel waveguide cross-section similar to that shown in Fig. 6.1.

Discretizing the cross-sectional relative dielectric permittivity $\varepsilon_r(x, y)$ and electric field $E_{x,y}(x, y)$ on a 2D grid of size $N_x \times N_y$ (where N_x, N_y are the integer number of grid points along the x and y axes, respectively), and replacing all derivatives in Eqs. 6.9-6.10 by their finite difference equivalents as discussed above, results in a set of algebraic finite difference equations which can be cast in the form of a matrix eigenvalue problem,

$$\mathbf{M}\phi = \beta^2\phi. \quad (6.11)$$

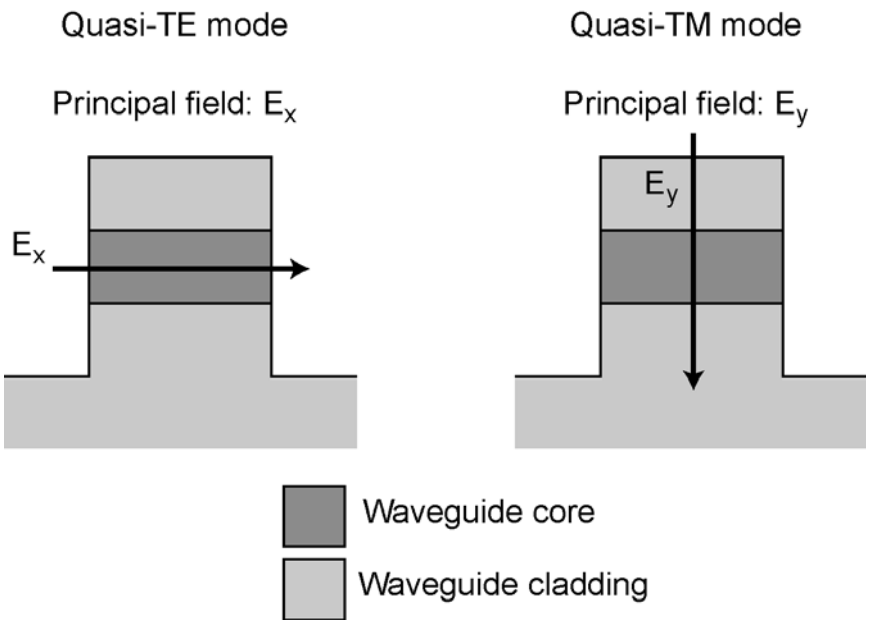

Figure 6.3: Principal field components associated with semivectorial quasi-TE (E_x) and quasi-TM (E_y) modes of a channel waveguide.

In Eq. 6.11, $\mathbf{M}$ is a non-symmetric sparse matrix of size $N_x N_y \times N_x N_y$, and ϕ is a length $N_x N_y$ column eigenvector containing the field $E_{x,y}$ at all the points on the 2D grid. The details of the specific form of the matrix $\mathbf{M}$ for the quasi-TE/quasi-TM modes are presented in [90].

Finally, in order to truncate the simulation domain, a set of boundary conditions must be applied along the domain's edges. These boundary conditions can be of the Dirichlet (field equals zero), Neumann (normal derivative of the field equals zero), or analytical (field decays exponentially) types. If the simulation domain is made large enough and includes sufficient cladding thickness around the waveguide core, the evanescent tails of the guided modes will completely decay away before reaching the outer boundaries, and a simple Dirichlet boundary condition may be used. Details of the incorporation of boundary conditions into the matrix $\mathbf{M}$ will not be presented here, for purposes of brevity. The interested reader is again directed to reference [90] for a thorough discussion.

Once the final form of the matrix $\mathbf{M}$ is known, the guided (and leaky) optical mode

profiles $E_{x,y}^{(i)}(x,y)$ and propagation constants $\beta^{(i)}$ of the particular waveguide structure defined by $\varepsilon_r(x,y)$ may then be found by numerical evaluation of the eigenvectors and eigenvalues of $\mathbf{M}$. The index i refers to the optical mode number, with $i = 0$ labeling the fundamental mode. As an example, a semivectorial finite difference mode solver implementing the approach above was used to numerically solve for the quasi-TE fundamental mode profile $E_x^{(0)}(x,y)$ and propagation constant $\beta^{(0)}$ of a 1.5 μm wide single-mode channel waveguide, as shown in Fig. 6.4. The wavelength was assumed to be $\lambda_0 = 1.55$ μm.

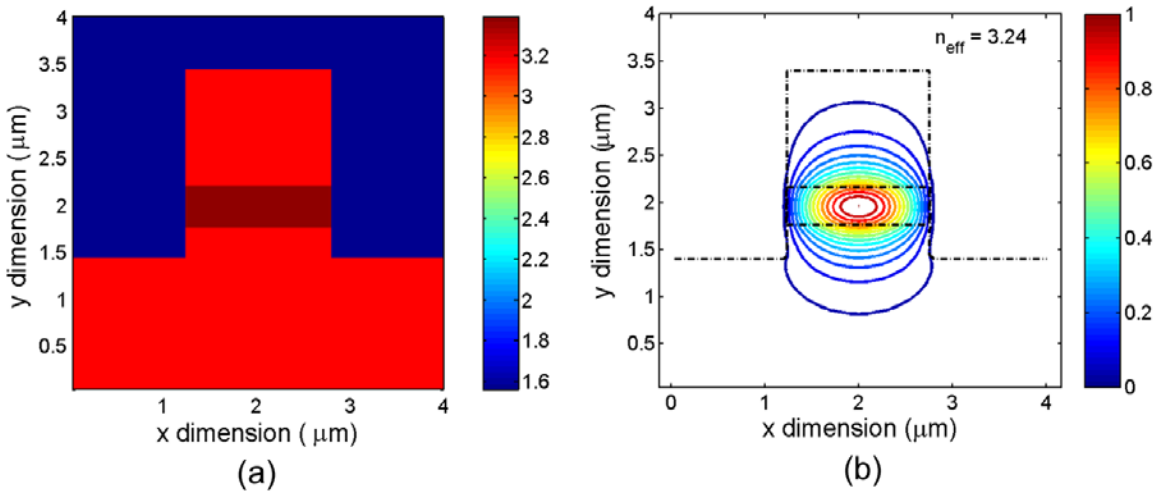

Figure 6.4: (a) Refractive index profile $n(x,y)$ of the simulated channel waveguide structure. The colorbar on the right labels the index within each layer. (b) Numerically computed equi-amplitude contours of the fundamental quasi-TE mode profile $E_x^{(0)}(x,y)$. The effective index for the mode shown is $n_{eff} = 3.24$. The black dash-dotted line illustrates the outline of the waveguide layers. The colorbar on the right indicates the (peak normalized) electric field amplitude.

The values of the refractive index n within each layer illustrated in Fig. 6.4(a), as well as the cross-sectional profile, were chosen to be similar to the deeply etched InGaAsP-InP semiconductor waveguides used in the planar photonic integrated circuits to be discussed in Chapter 7. The semiconductor waveguide core (dark red region) has $n = 3.39$, the semiconductor cladding layers (light red regions) have $n = 3.17$, and the lateral cladding (blue region) has $n = 1.56$. The semiconductor

waveguide core layer is 400 nm thick. Figure 6.4(b) contains a contour plot of the fundamental quasi-TE transverse mode profile $E_x^{(0)}(x, y)$, normalized to have a peak value of unity. The dash-dotted black line illustrates the boundaries of each layer in the waveguide structure, showing that the mode profile is strongly confined to the high index semiconductor waveguide core layer. The computed modal effective index is $n_{eff} = 3.24$, where n_{eff} is proportional to the propagation constant $\beta^{(0)}$ as

$$n_{eff} = \frac{\beta^{(0)}\lambda_0}{2\pi}.$$

Although the discussion presented above has focused upon finite difference techniques for 2D waveguide structures, the concepts are equally applicable to waveguides with only 1D optical confinement, such as the slab waveguides used for ABR microcavities in Chapter 4. For a slab waveguide in which the dielectric layers are oriented normal to the y-axis, setting $\partial/\partial x = 0$ in Eqs. 6.9-6.10 gives the relevant 1D semivectorial Helmholtz equations for the quasi-TE and quasi-TM modes. Application of the finite difference approximations on a 1D axis of length N_y results in a matrix $\mathbf{M}$, this time of size $N_y \times N_y$, whose eigenvectors and eigenvalues give the 1D mode profiles $E_{x,y}^{(i)}(y)$ and propagation constants $\beta^{(i)}$.

6.3 Multimode interference couplers

The coupling region of any waveguide-resonator device must be designed keeping several concerns in mind. Particularly, these can include designing for a desired power coupling ratio, ensuring broadband operation, minimization of the coupler size/length, and ease of fabrication. In-plane lateral evanescent directional couplers, in which power is exchanged between phase-matched modes of two proximal dielectric waveguides separated by a "coupling gap" [65], are commonly used in a number of devices [140]. However, when high index contrast waveguides must be used in order to make low-loss, small radius bends, such as those required for microring and microdisk resonators, the fabrication of appropriate evanescent directional couplers

[12] becomes more difficult. The tight confinement of the optical mode within the waveguide requires that the coupling gap be made extremely small, i.e. on the order of ∼100 nm, in order to achieve evanescent coupling. Fabrication of features on this size scale naturally requires electron beam lithography, and moreover, coupler performance will be extremely sensitive to small deviations in the coupling gap size, leading to issues of reproducibility.

Several other coupling schemes have been studied in order to mitigate the problems associated with lateral evanescent couplers. For example, the vertical evanescent coupling configuration carries the advantage that the coupling gap between the two waveguides can be precisely and reproducibly controlled via epitaxial crystal growth [141], physical vapor deposition [142], or spin coating of dielectric materials [20]. However, the fabrication procedure for vertical couplers can be significantly more complex than that for lateral couplers, at the very least requiring multiple lithography and alignment steps, and potentially incorporating the use of more difficult processes such as direct wafer bonding. Adiabatic couplers [143, 144] make use of the principle that an optical system excited into a given mode will remain in that mode while the system is changed, provided that it is changes slowly. The exact dimensions (length and cross-section) of the adiabatic coupling region are not critical to the coupler performance, and can in fact be very tolerant to the kinds of fabrication errors or offsets which would strongly affect the performance of lateral evanescent couplers. However, in order to make an adiabatic waveguide transition, the coupling region of such a device naturally becomes very long in comparison to that of an evanescent coupler, consuming valuable "real estate" on the substrate.

Multimode interference (MMI) couplers have proven to be useful in realizing highly compact, fabrication tolerant couplers and power splitters/combiners within high index contrast materials [145]. This type of coupler is based upon the concept of self-imaging in a multimode waveguide [146,147]. Self-imaging is a property of multimode waveguides which produces a series of single or multiple images of the electromagnetic field profile at the waveguide input, at periodic intervals along the waveguide propagation direction. If single-mode waveguides are used to generate the input field

profile, a number of identical single-mode waveguides can be placed at any of the image planes along the axis of the multimode waveguide, in order to generate a variety of MMI couplers.

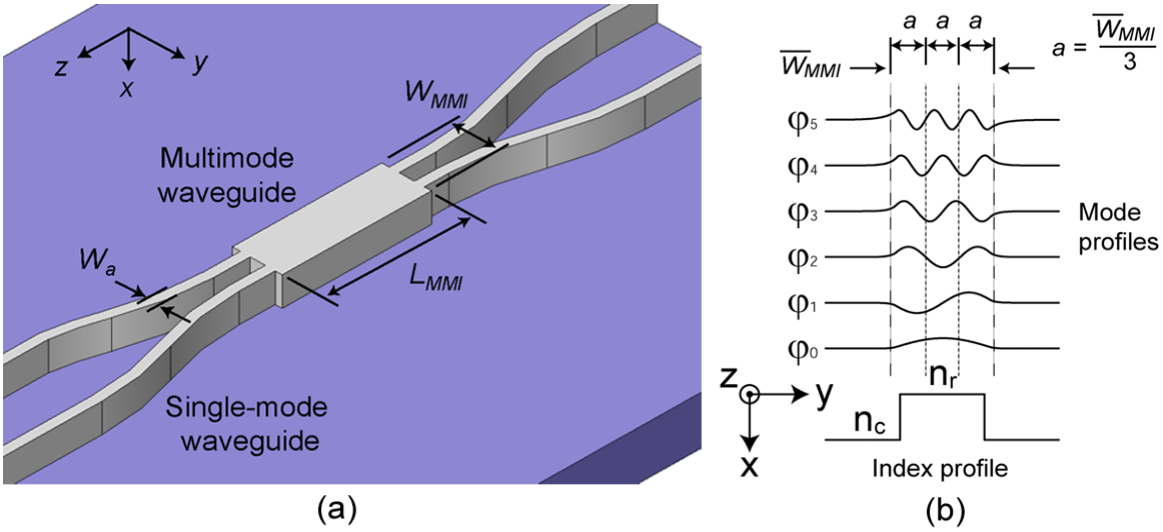

Figure 6.5: (a) Schematic of a typical 2×2 MMI coupler. Propagation occurs along the z-axis. (b) Illustration of the transverse field profiles φ_ν supported by the multimode waveguide, superimposed against the laterial refractive index profile. The effective refractive indexes under the ridge and in the lateral cladding are labeled n_r and n_c, respectively. The vertical dotted lines label the positions dividing the effective MMI width $\overline{W}_{MMI}$ into thirds, used for aligning the access waveguides for restricted interference couplers.

An illustrative analysis of MMI couplers can be carried out by expanding the fields in terms of the guided eigenmodes of the multimode waveguide [148, 149]. Figure 6.5(a) depicts a typical 2×2 MMI coupler, with input/output access waveguides having width W_a butt-coupled into a wider multimode section having width W_{MMI} and length L_{MMI}. The effective index approximation [69] can be used to reduce the refractive index profile of the two-dimensional multimode waveguide cross-section to one dimension (across the lateral y-axis), as shown at the bottom of Fig. 6.5(b). Solution of the Helmholtz equation in the multimode waveguide yields guided field profiles $\varphi_\nu(y)$ similar to those illustrated in this same figure. The propagation constants β_ν

of the modes can be approximated as

$$\begin{aligned}\beta_\nu &= \sqrt{k_0^2 n_r^2 - k_y^2} \simeq \sqrt{k_0^2 n_r^2 - \frac{\pi^2(\nu+1)^2}{\overline{W}_{MMI}^2}} \\ &= k_0 n_r - \frac{\pi^2(\nu+1)^2}{2k_0 n_r \overline{W}_{MMI}^2},\end{aligned} \tag{6.12}$$

where k_0 is the wavenumber in free space, n_r is the effective refractive index under the multimode waveguide ridge, $\overline{W}_{MMI}$ is the effective width of the MMI region, taking into account the finite penetration of the field into the lateral cladding region, and $\nu = 0, 1, 2, ...$ To obtain the expression in the last line, we have made the assumption that $k_y \ll k_0 n_r$ and used the binomial expansion.

The transverse field at the input of the multimode waveguide, $\Phi(y, z) = \Phi(y, 0)$, is assumed to be completely contained within the width of $\overline{W}_{MMI}$. Therefore, this input field can be decomposed into the guided modes of the multimode waveguide, as

$$\Phi(y, 0) = \sum_\nu c_v \varphi_\nu(y), \tag{6.13}$$

where the mode excitation coefficients are given by the overlap integrals

$$c_\nu^2 = \frac{\int |\Phi(y,0)\varphi_\nu(y)|\, dy}{\left[\int |\Phi(y,0)|^2\, dy \int |\varphi_\nu(y)|^2\, dy\right]^{1/2}}. \tag{6.14}$$

The total field within the multimode waveguide at a distance z along its axis can be written as a superposition of all the guided modes excited at the input, with their appropriate phase factors. We have:

$$\begin{aligned}\Phi(y, z) &= \sum_\nu c_v \varphi_\nu(y) \exp(-i\beta_\nu z) \\ &= \exp(-i\beta_0 z) \sum_\nu c_v \varphi_\nu(y) \exp\left[i(\beta_0 - \beta_\nu)z\right] \\ &= \sum_\nu c_v \varphi_\nu(y) \exp\left[i\frac{\nu(\nu+2)\pi}{3L_\pi} z\right],\end{aligned} \tag{6.15}$$

where the expression for β_ν in Eq. 6.12 was used in going from the second to the

third line, and the common phase factor $\exp(-i\beta_0 z)$ was dropped.

The phase factor in the last line of Eq. 6.15 gives rise to the reproduction of single or multiple images of the input field at certain lengths L_{MMI} of the multimode waveguide. Using the fact that $\nu(\nu+2)$ is even for ν even and odd for ν odd, and defining the beat length L_π as

$$L_\pi = \frac{\pi}{\beta_0 - \beta_1}, \tag{6.16}$$

Eq. 6.15 can be rewritten as

$$\Phi(y, L_{MMI}) = \begin{cases} \sum_\nu c_\nu \varphi_\nu(y) \\ \sum_\nu (-1)^{\nu+1} c_\nu \varphi_\nu(y) \\ \sum_{\nu \text{ even}} i(-1)^q c_\nu \varphi_\nu(y) + \sum_{\nu \text{ odd}} c_\nu \varphi_\nu(y) \end{cases} \quad \text{for } L_{MMI} = \begin{cases} 2q(3L_\pi) \\ (2q+1)(3L_\pi) \\ (q+\frac{1}{2})(3L_\pi) \end{cases}, \tag{6.17}$$

where $q = 0, 1, 2, ...$ Making use of the even/odd symmetry of the modes $\varphi_\nu(y)$ with respect to the center line of the multimode waveguide, Eq. 6.17 can be expressed in terms of the input field at $z = 0$, as

$$\Phi(y, L_{MMI}) = \begin{cases} \Phi(y, 0) \\ -\Phi(-y, 0) \\ \frac{i(-1)^q+1}{2}\Phi(y, 0) + \frac{i(-1)^q-1}{2}\Phi(-y, 0) \end{cases} \quad \text{for } L_{MMI} = \begin{cases} 2q(3L_\pi) \\ (2q+1)(3L_\pi) \\ (q+\frac{1}{2})(3L_\pi) \end{cases}. \tag{6.18}$$

Equation 6.18 shows that the MMI coupler operates in the bar state, cross state, and 3 dB state, when L_{MMI} is chosen to be $2q(3L_\pi)$, $(2q+1)(3L_\pi)$, or $(q+1/2)(3L_\pi)$, respectively. Note that in the 3 dB state, the two images are in phase quadrature with one another. Thus, a low-loss MMI coupler is realized by truncating the multimode waveguide at the desired L_{MMI}, and placing the single-mode output waveguides at the lateral positions of the single/multiple images, such that a large overlap between $\Phi(y, L_{MMI})$ and the mode of the output waveguides exists.

The situation above is typically referred to as one of *general interference*, i.e. no special restrictions are placed upon the excitation of modes at $z = 0$. However, if the modes $\nu = 2, 5, 8, ...$ are not excited at $z = 0$, it can be shown that a similar reproduc-

tion of single/multiple images will occur as in Eq. 6.18, only with $3L_\pi$ replaced by L_π. Thus, the MMI coupler can accordingly be made three times shorter. This type of modal excitation can be achieved by exciting the multimode waveguide with a mode of even symmetry (i.e. the fundamental mode of a single-mode waveguide) centered at the positions dividing the effective MMI width $\overline{W}_{MMI}$ into thirds, as labelled by the dotted lines in Fig. 6.5(b). The modes $\nu = 2, 5, 8, ...$ possess odd symmetry about these positions, and the overlap integrals in Eq. 6.14 will consequently yield $c_\nu = 0$ for these modes. This MMI configuration is referred to as one producing *restricted interference*, for the selective excitation of modes.

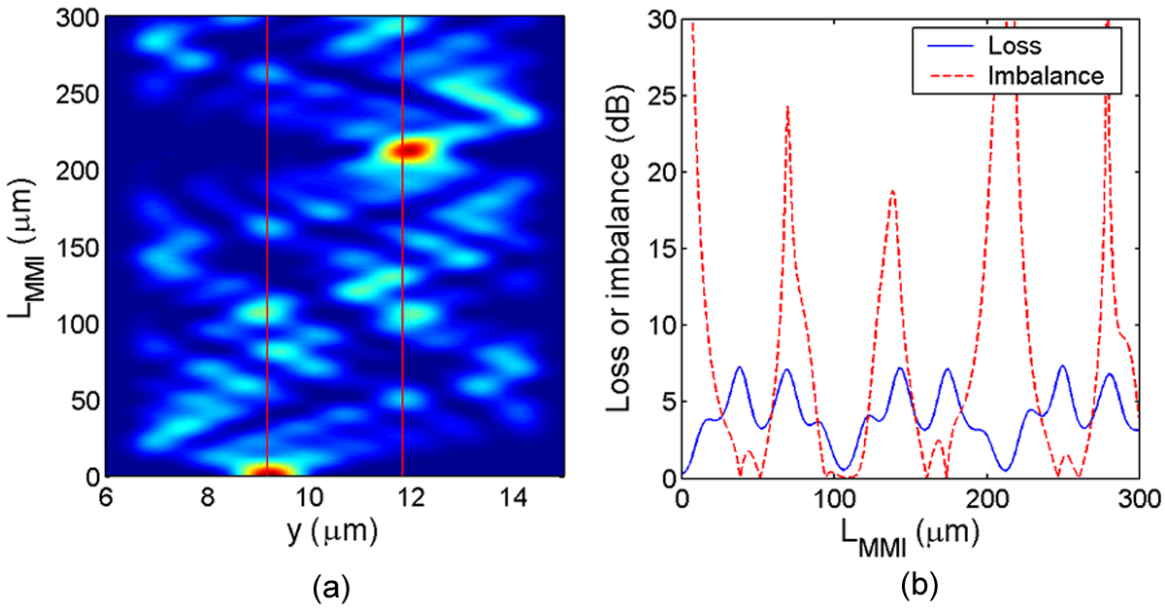

Figure 6.6: (a) Normalized intensity pattern within a 2×2 restricted interference MMI coupler with $W_{MMI} = 8$ μm, $n_r = 3.276$, $n_c = 3.17$, excited at $\lambda = 1.55$ μm. The vertical red lines label the center positions of 1.0 μm wide single-mode input/output access waveguides. The red (bright) and blue (dark) colors indicate regions of high and low intensity, respectively. (b) Net MMI coupler loss and imbalance as a function of L_{MMI}.

Figure 6.6(a) plots the normalized intensity within the multimode waveguide as a function of L_{MMI}, for a 2×2 MMI coupler. The 1.0 μm wide input/output single-mode access waveguides have been placed at the appropriate positions relative to the

8 μm wide multimode section in order to achieve restricted interference. The vertical red lines label the centers of the input/output waveguides. The effective refractive indexes under the waveguide ridge and in the lateral cladding are given by $n_r = 3.276$ and $n_c = 3.17$, respectively, values in the correct range for a typical waveguide with an InGaAsP core and InP cladding. The multimode waveguide is excited from one input waveguide only, as indicated by the high-intensity region along the lower left edge of Fig. 6.6(a). Beating between the excited modes of the multimode waveguide leads to evolution of a complex interference pattern along the propagation direction. A single inverted image of the input is reproduced at a distance $L_\pi = 212$ μm, i.e. the cross state of the coupler, and a double image is produced at $L_\pi/2 = 106$ μm, i.e the 3 dB state. Figure 6.6(b) plots the excess power loss and imbalance at the two outputs as a function of L_{MMI}, as defined by

$$\text{excess loss} = 10\left|\log\left[\frac{P_{out,1}+P_{out,2}}{P_{in,1}+P_{in,2}}\right]\right| \tag{6.19}$$

$$\text{imbalance} = 10\left|\log\left[\frac{P_{out,1}}{P_{out,2}}\right]\right| \tag{6.20}$$

where $P_{out,(1,2)}$ and $P_{in,(1,2)}$ are the power in each of the two output and input waveguides, respectively. In the cross state, the loss is at a local minimum ($\sim$ 0.5 dB) and the imbalance is large ($>$ 30 dB), indicating low cross-talk, since all the power is coupled into a single output waveguide. In the 3 dB state, the loss is again at a local minimum ($\sim$ 0.5 dB), but the imbalance is also minimized ($<$ 0.1 dB), since the power is coupled equally into the two output waveguides. Minimizing the 3 dB coupler imbalance is particularly important when designing Mach-Zehnder interferometers with large extinction ratio.

6.4 Coupled waveguide-resonator device fabrication

The fabrication process used for InGaAsP-InP planar integrated optical devices was common in many respects to the fabrication process for ABR microcavities discussed in Chapter 4, making use of several similar procedures. There were, however, several notable additions with respect to the fabrication of the electrodes required for electrically driven coupled waveguide-resonator-based devices, such as those which will be presented in Chapter 7. Figure 6.7 depicts the InGaAsP-InP semiconductor double heterostructure waveguide used to fabricate these devices. The structure consisted of an n-type InP substrate, a 3 μm InP buffer/lower cladding layer, a 0.4 μm InGaAsP ($\lambda_{gap} = 1.3$ μm) waveguide core layer, a 1.2 μm InP upper cladding layer, and a 0.2 μm p-type InGaAs cap layer. The waveguide core and upper/lower cladding layers were grown nominally undoped, by metal-organic chemical vapor deposition (MOCVD).

The process flow for fabrication of the switch devices discussed in Chapter 7 is illustrated in Fig. 6.8, and can be applied to any InGaAsP-InP semiconductor slab waveguide substrate, as follows. Lower case letters in parentheses (a-i) in the text refer to the sub-diagrams in Fig. 6.8.

First, an etch mask layer of SiO_2 was deposited by PECVD. A layer of PMMA electron beam resist was then applied by spin coating (a). Subsequently, direct electron beam lithography was employed to expose an array of patterns within the PMMA, using a Leica Microsystems EBPG 5000+ electron beam writer operating at 100 keV (b). After development, the PMMA patterns were transferred into the underlying SiO_2 layer using an ICP-RIE etch step and C_4F_8 gas. The remaining PMMA was cleanly removed using an O_2 plasma (c). Transfer of the patterns into the semiconductor substrate was accomplished using ICP-RIE etching and $HI/H_2/Ar$ chemistry [98], using the SiO_2 layer as a hard mask. The waveguides were deeply etched through the InGaAsP waveguide in order to ensure strong optical confinement for compact low-loss waveguide bends [150]. The remaining SiO_2 mask was then removed in a buffered hydrofluoric acid solution (d). Next, a benzocyclobutene (BCB) electrical

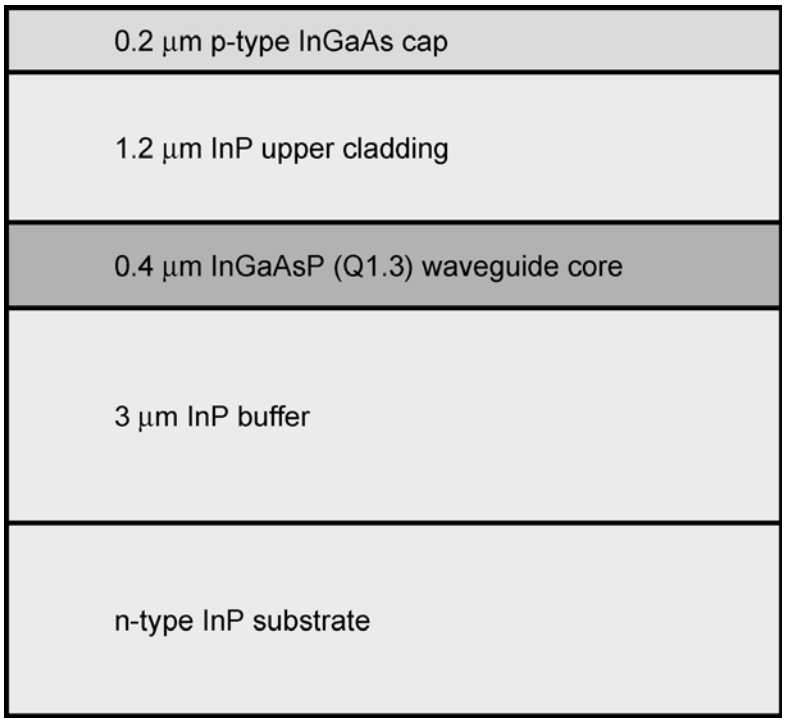

Figure 6.7: InGaAsP-InP semiconductor epistructure used for the hybrid MZI/racetrack resonator switch.

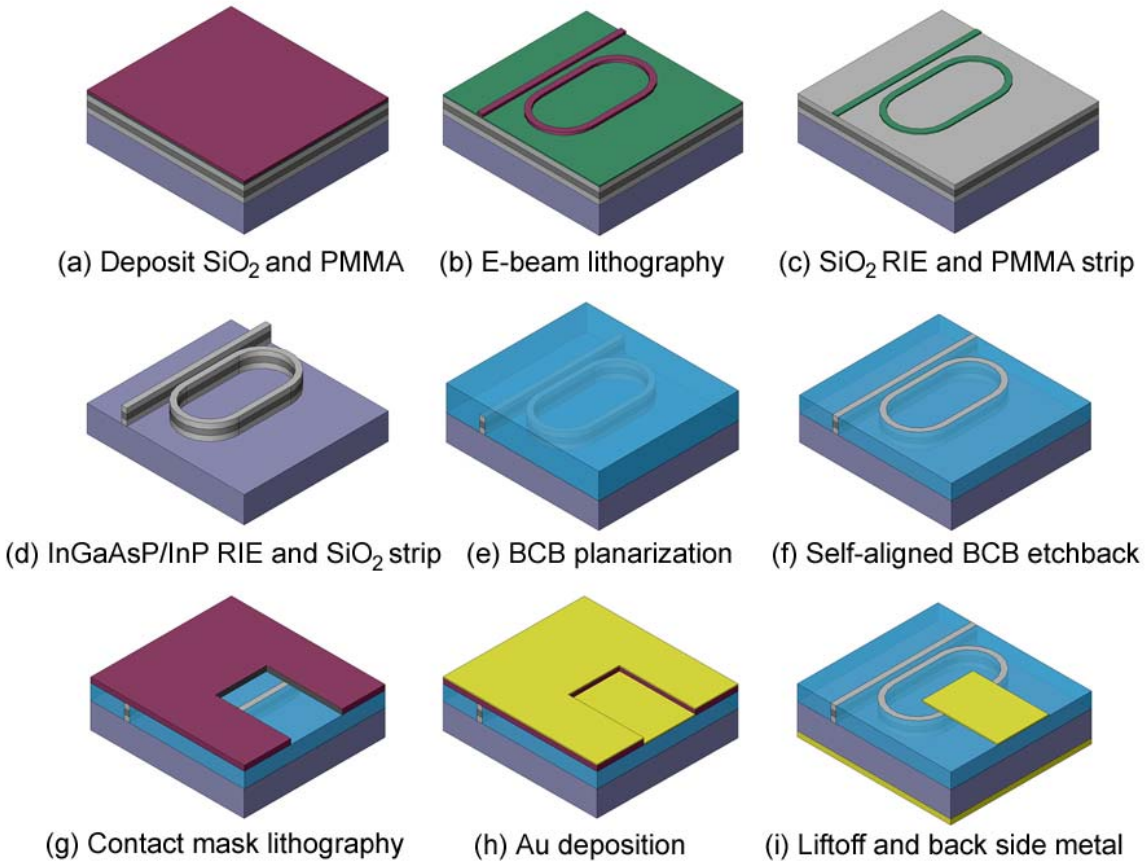

Figure 6.8: Process flow for general electrically contacted ring resonator-based devices.

isolation layer was applied by spin coating and cured at 300 °C. During the thermal cure, the BCB layer reflowed and planarized the sample surface (e). In a self-aligned procedure, a short ICP-RIE etch using a NF_3/O_2 gas mixture was used to partially etch back the BCB, exposing the tops of the waveguide ridges (f). Subsequently, a layer of UV photoresist (Shipley 1813) was applied by spin coating, and was exposed using an appropriate mask and contact lithography to define the desired pattern for the front side electrodes (g). After a short wet etch in a buffered hydrofluoric acid solution to remove any residual oxides on the exposed waveguide ridges, the front side (p-type doped) of the sample was metallized with Cr/AuZn/Au, deposited by thermal evaporation (h). The sample was then soaked in acetone (often with the aid of weak ultrasonic agitation) to lift off the unwanted metal, leaving behind the desired electrodes. The InP substrate was mechanically thinned to a thickness of $\sim$100 μm, metallized on the back side (n-type doped) with AuGe/Au, cleaved into bars, and mounted to brass submounts with conductive epoxy for testing (i).

Chapter 7

Hybrid Mach-Zehnder interferometer/racetrack resonator geometry for low power thermooptic switching via coupling control

7.1 Introduction

In this chapter, a device architecture employing controlled waveguide-resonator coupling for low power optical modulation and switching is presented. The geometry to be illustrated here is a hybrid integration of a Mach-Zehnder interferometer (MZI) with a racetrack resonator, in which the MZI operates as an electronically tunable coupler. A theoretical analysis of the hybrid switch's transmission characteristics will be presented below, illustrating that this geometry achieves a significant reduction of the required electrical switching power with comparison to the conventional MZI configuration. The compromise between switching power reduction and the optical switching bandwidth will also be discussed. The demonstration of an InGaAsP-InP semiconductor hybrid switch device will then be described, in which electrical control of waveguide-resonator coupling is achieved using thermooptic effects [151]. Subsequently, the device's steady state optical transmission and modulation response will be characterized, revealing the predicted reduction in switching power, good ON-OFF

switching contrast, and microsecond switching speed. Finally, a set of measurements used to evaluate the thermooptic coefficients in the demonstrated integrated optical devices will be described.

7.2 Analysis of the hybrid switch geometry

One intriguing application of the microring resonator optical platform is the active control of an optical signal through precise command of the magnitude of waveguide-resonator coupling [152]. Consider the geometry in Fig. 7.1, in which one of the output ports of a 2×2 MZI is connected with one of the input ports to form a racetrack-shaped resonator. In this composite architecture, the waveguide-resonator coupling coefficient κ can be modulated via electrical control of the relative phase $\Delta\phi$ between the MZI arms. As will be shown below, this hybrid MZI/racetrack resonator can achieve high-contrast modulation of an optical input wave, and furthermore, can reduce the required electrical switching power in comparison with a conventional MZI of similar dimensions [152]. Switching is achieved by tuning $\Delta\phi$ to bring the resonator in and out of *critical coupling*, the state in which complete destructive interference occurs between the portion of the travelling wave coupled out of the resonator and the wave transmitted past the resonator [11].

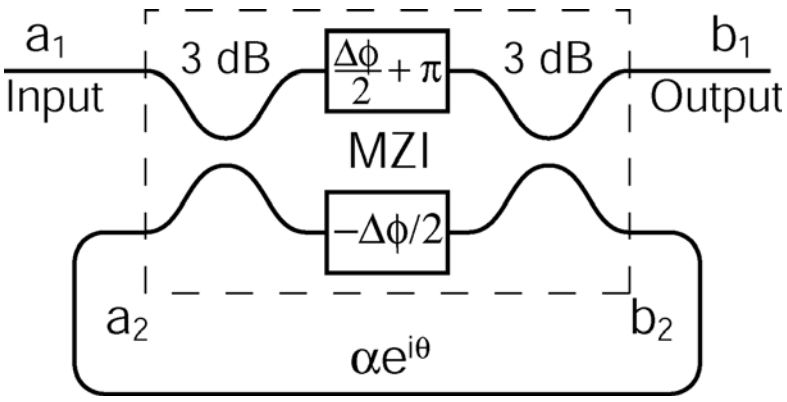

Figure 7.1: Schematic of the hybrid MZI/racetrack resonator switch geometry, illustrating the relevant electric field components a_1, a_2, b_1, b_2, and the relative phase $\Delta\phi$ between the arms of the MZI.

The optical transmission characteristics of the hybrid MZI/racetrack resonator switch in Fig. 7.1 are derived using the coupling matrix in Eq. 7.1, and the resonator circulation condition in Eq. 7.2 [152].

$$\begin{bmatrix} b_1 \\ b_2 \end{bmatrix} = \begin{bmatrix} t & \kappa \\ \kappa^* & -t^* \end{bmatrix} \begin{bmatrix} a_1 \\ a_2 \end{bmatrix} = i \begin{bmatrix} \cos(\Delta\phi/2) & -\sin(\Delta\phi/2) \\ \sin(\Delta\phi/2) & \cos(\Delta\phi/2) \end{bmatrix} \begin{bmatrix} a_1 \\ a_2 \end{bmatrix} \tag{7.1}$$

$$a_2 = \alpha e^{i\theta} b_2 \tag{7.2}$$

The coupling matrix relates the complex electric field components a_1 and a_2 at the MZI input to the MZI output components b_1 and b_2, through the coupling and transmission coefficients κ and t. The field quantities are normalized such that their squared absolute value, i.e., $|a_1|^2$ represents the power at a given port. Equation 7.1 shows that κ and t are functions of the relative phase $\Delta\phi$ between the arms of the MZI. The upper branch of the MZI in Fig. 7.1 is shown with an extra bias phase of π, in order to ensure that $\kappa = 0$ when $\Delta\phi = 0$. For a lossless MZI, $|\kappa|^2 + |t|^2 = 1$. Light propagation through the resonator is characterized by a round-trip transmissivity α, and a phase factor $e^{i\theta}$, as shown in Eq. 7.2. For a lossless resonator, $\alpha = 1$. The round-trip phase is given by $\theta = 2\pi n_{eff} L_r/\lambda$, where n_{eff} is the effective index of the optical mode in the racetrack, L_r is the racetrack circumference, and λ is the optical wavelength. Combining these relationships results in the expression for the normalized transmitted optical power P_{out}/P_{in} shown in Eq. 7.3.

$$\frac{P_{out}}{P_{in}} = \left|\frac{b_1}{a_1}\right|^2 = \frac{\alpha^2 + \cos^2(\Delta\phi/2) - 2\alpha\left|\cos(\Delta\phi/2)\right|\cos(\theta)}{1 + \alpha^2\cos^2(\Delta\phi/2) - 2\alpha\left|\cos(\Delta\phi/2)\right|\cos(\theta)} \tag{7.3}$$

On resonance ($\theta = 2m\pi$, $m = 1, 2, 3...$), the normalized transmission becomes

$$\frac{P_{out}}{P_{in}} = \left|\frac{b_1}{a_1}\right|^2 = \frac{\left[\alpha - \left|\cos(\Delta\phi/2)\right|\right]^2}{\left[1 - \alpha\left|\cos(\Delta\phi/2)\right|\right]^2}. \tag{7.4}$$

Transmission through the device is switched from unity at $\Delta\phi = 0$ ($|t| = |\cos(\Delta\phi/2)| = 1$, $|\kappa| = 0$) to a theoretical value of zero at the condition of critical coupling, given by

$\alpha = |t| = |\cos(\Delta\phi/2)|$, or $\Delta\phi = 2\cos^{-1}(\alpha)$. In contrast, the normalized transmission of a conventional MZI (one without an integrated resonator, equivalent to $\alpha = 0$) is given by

$$\left.\frac{P_{out}}{P_{in}}\right|_{MZI} = \cos^2(\Delta\phi/2), \tag{7.5}$$

and the relative phase required for ON-OFF switching is $\Delta\phi = \pi$. Figure 7.2 compares the normalized transmission on-resonance through the hybrid device with that of a conventional MZI, as a function of the relative phase $\Delta\phi$. For a low loss resonator as shown ($\alpha = 0.99$), the portion of the hybrid device's transmission curve near $\Delta\phi = 0$ is extremely steep. Compared with the conventional MZI, operation within this region makes high-contrast modulation possible with a comparatively small change in the relative phase $\Delta\phi$.

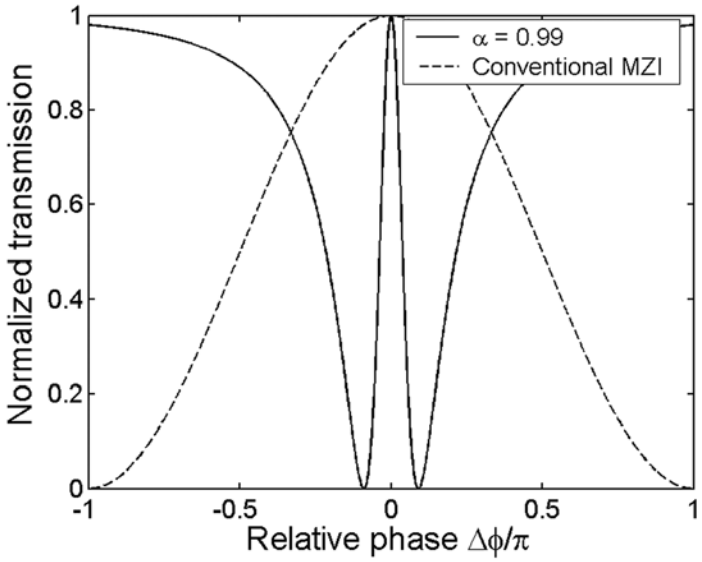

Figure 7.2: Comparison of the on-resonance normalized transmission through the hybrid MZI/racetrack resonator switch with $\alpha = 0.99$, with the transmission through a conventional MZI. The hybrid device switches ON-OFF with a fraction of the π phase shift required for the conventional MZI.

In practical devices, it is possible to control $\Delta\phi$ electronically, through the application of an electric field or current. For example, electrooptic [153], thermooptic [154], or free carrier dispersion [111] effects may be utilized to control $\Delta\phi$. The reduction

in the phase shift required for ON-OFF switching shown in Fig. 7.2 then translates into a reduction in the required applied voltage or electrical power. In the context of the thermooptic effects relevant to the device demonstrated below, it is appropriate to express the relative phase in terms of the dissipated electrical power ΔP_e (which induces a relative temperature change ΔT between the two arms of the MZI), as shown in Eq. 7.6.

$$\Delta\phi = \frac{\pi}{\Delta P_\pi}\Delta P_e \tag{7.6}$$

In the above expression, ΔP_π is defined as the power required to induce $\Delta\phi = \pi$, and is thus equivalent to the switching power for a conventional MZI. Therefore, critical coupling occurs when $\Delta P_e = \Delta P_{cr} = 2\Delta P_\pi \cos^{-1}(\alpha)/\pi$. The ratio of the switching powers $\Delta P_{cr}/\Delta P_\pi$, given in Eq. 7.7, provides a quantitative metric for comparison of the hybrid switch with the conventional MZI.

$$\frac{\Delta P_{cr}}{\Delta P_\pi} = \frac{2\cos^{-1}(\alpha)}{\pi} \tag{7.7}$$

This switching power reduction ratio is plotted in Fig. 7.3 for α in the range $0 \leq \alpha \leq 1$, illustrating that a significant decrease in the switching power can be expected in the limit of low resonator loss, $\alpha \sim 1$.

However, while presenting desirable improvements in terms of the required switching power, the hybrid device naturally has limitations to its maximum switching speed, on account of the feedback path introduced by the racetrack resonator. The switching bandwidth $\Delta\nu_{hybrid}$ is limited by the photon storage time in the racetrack, and is given by the spectral half-width-at-half-maximim of the cavity resonance. Using Eqs. 7.1-7.2 to solve for the circulating power in the racetrack $|a_2/a_1|^2$, and finding the values of the round-trip phase $\pm\theta_{1/2}$ where the circulating power drops to one half its peak value, the switching bandwidth can be expressed as

$$\Delta\nu_{hybrid} = \frac{c}{2\pi n_{eff} L_r}\frac{1-\alpha}{\sqrt{\alpha}}, \tag{7.8}$$

assuming an unloaded resonator ($|t| = 1$), and $\pm\theta_{1/2} \ll 2\pi$. In the above expression, c

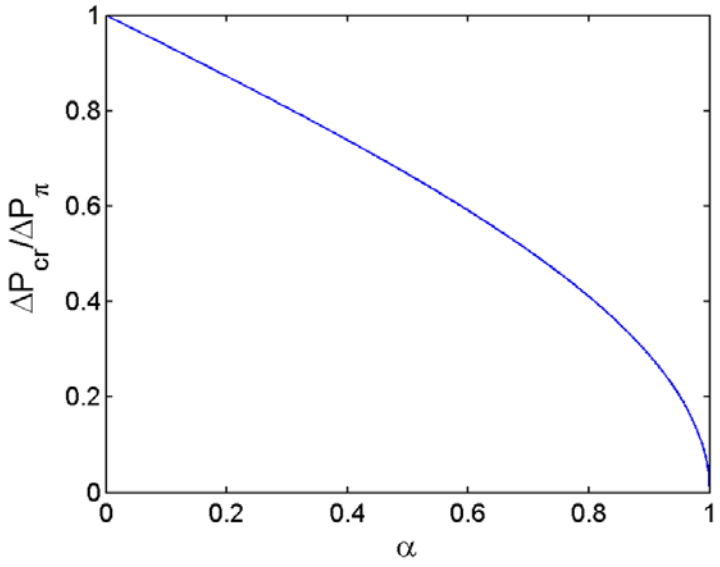

Figure 7.3: Switching power reduction ratio as a function the racetrack round-trip transmissivity α.

is the speed of light, n_{eff} is the effective index of the racetrack resonator mode, and L_r is the racetrack circumference. Figure 7.4 plots the relationship between the switching power reduction ratio and the resulting bandwidth (implicit upon α), illustrating as expected that the optical bandwidth is reduced as the reduction ratio grows small. Values of $n_{eff} = 3.3$ and $L_r = 500$ μm were used for the plot. The bandwidth and power reduction can be traded off with one another to produce a switch with the desired properties, depending upon the application.

7.3 Characterization of InGaAsP-InP switch performance

7.3.1 InGaAsP-InP device parameters

The hybrid switch geometry fabricated and tested is shown in the 3D schematic and optical microscope images in Figs. 7.5(a)-(b), respectively. The MZI was composed of two 3 dB multimode interference (MMI) couplers, designed using the analysis

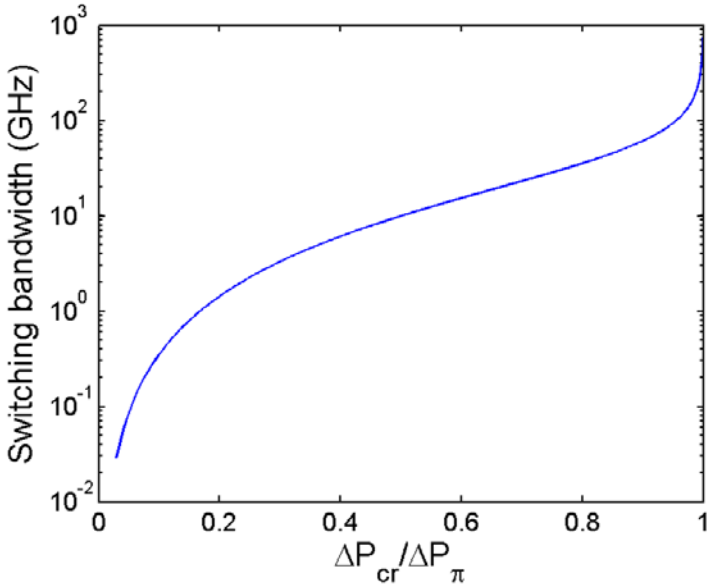

Figure 7.4: Switching bandwidth as a function of the switching power reduction ratio, for a racetrack resonator with effective index $n_{eff} = 3.3$ and circumference $L_r = 500$ μm.

described in Chapter 6. The MMI couplers were 8 μm wide and 90 μm long, and the MZI electrodes were 180 μm long. The racetrack resonator had bends of 50 μm radius, and a total circumference of 1430 μm. The single-mode channel waveguides were nominally 1.5 μm wide.

7.3.2 Measurement apparatus

The hybrid switch device was tested using the apparatus shown in Fig. 7.6. Light from a fiber coupled tunable laser source was collimated for free space, and coupled into the input waveguide facet of the switch through a 60x (NA = 0.65) aspheric lens. A 40x (NA = 0.55) aspheric lens was used to collect the transmitted light from the output end of the device. Both aspheric lenses were mounted on precision 5-axis micrometer translation stages for careful positioning of the lens focal planes relative to the input and output facets. The micrometers used on the stages had a resolution of $\sim$0.02 μm, in order to allow for precise optimization of the input coupling efficiency. However, the input coupling efficiency was in general limited due to a significant

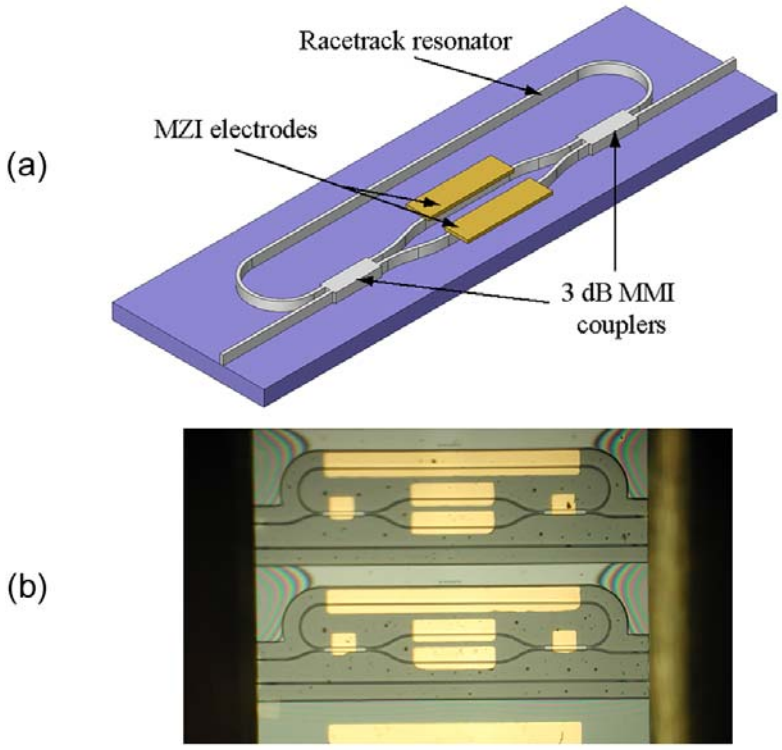

Figure 7.5: (a) 3D schematic of the device geometry as fabricated (not to scale). The relevant component parts are labeled, including the 3 dB MMI couplers, MZI electrodes, and racetrack resonator. (b) Optical microscope image of several InGaAsP-InP switches. The gold-colored regions are the electrodes. The electrodes on the racetrack resonator and MMI couplers were not used.

degree of overlap mismatch between the aspheric lens focal spot size and the optical mode of the semiconductor waveguide. Tapered waveguide mode convertors can be used to improve the input coupling efficiency [144]. The pellicle beamsplitters were used to bring in white light (from two lamp sources not shown in Fig. 7.6) to image the input/output waveguide facets, with the help of the CCD or infrared cameras.

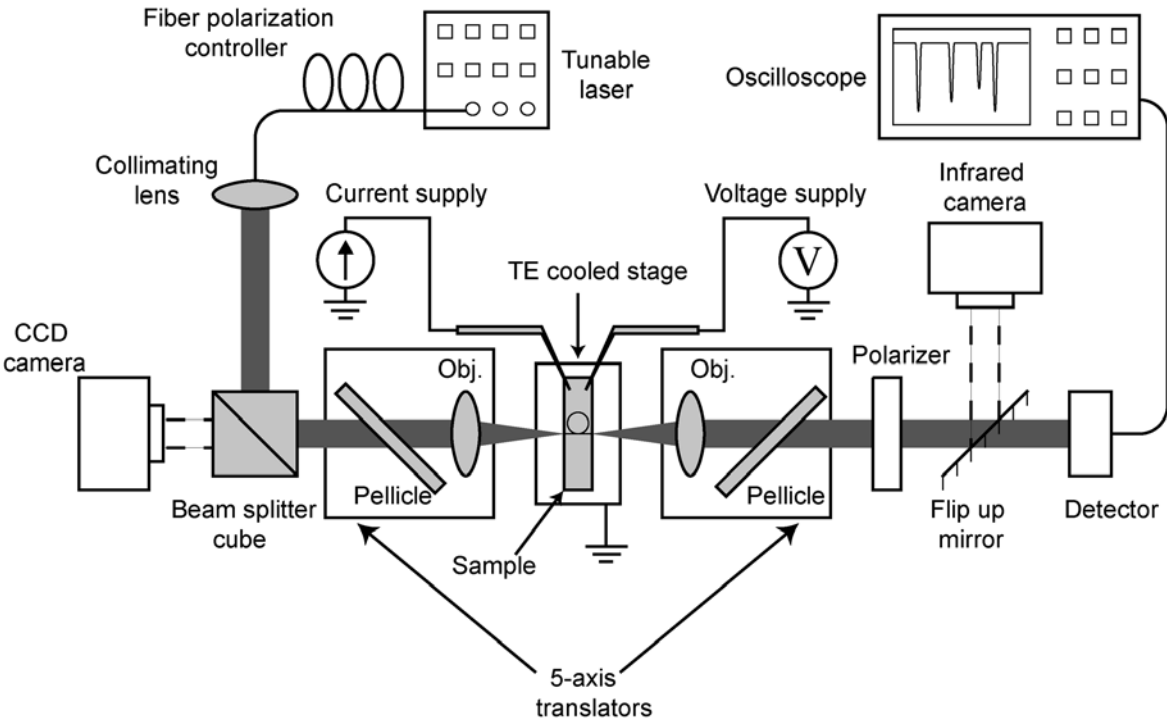

Figure 7.6: Schematic of apparatus used to measure hybrid switch performance.

The polarization of the laser input was controlled with a set of fiber paddles and a linear polarizer, and the input intensity was controlled via a variable attenuator. A calibrated infrared photodetector was placed at the output to measure the power transmitted through the device, and an oscilloscope was used to monitor the detector signal. Alternatively, the output from the hybrid switch could be directed into an infrared vidicon camera via a flip-up mirror. This camera was useful for viewing the optical mode profile at the output waveguide facet, and for optimizing the input coupling conditions. Active control of the switch was achieved through injection of current into one of the MZI electrodes shown in Fig. 7.5(a). Electrical probe tips

with micrometer positioners were used to make contact between the device electrodes and the external circuit.

7.3.3 DC and dynamic output response

As discussed in Section 7.2, switching of the transmitted optical power was achieved through control of the coupling coefficient κ, via electrical modulation of the MZI relative phase $\Delta\phi$. The mechanism of phase control used here was thermooptic in nature. As current injected into the MZI electrode passes vertically through the series resistance of the semiconductor channel waveguide (measured at $\sim$600 Ω) and into the back side contact, ohmic heating changes the waveguide's refractive index, and introduces a phase shift given by

$$\Delta\phi = \frac{2\pi L_e}{\lambda}\frac{\partial n_{eff}}{\partial T}\Delta T = \frac{2\pi L_e}{\lambda}\frac{\partial n_{eff}}{\partial T} Z_T \Delta P_e, \tag{7.9}$$

where L_e is the electrode length, dn_{eff}/dT is the waveguide's thermooptic coefficient, and ΔT is the temperature change [154]. In going from the first to the second equality in Eq. 7.9, the proportionality of the temperature change to the dissipated electrical power is expressed, where the proportionality constant Z_T is the thermal impedance [107]. The thermooptic coefficient is $\partial n_{eff}/\partial T \sim 2.7 \times 10^{-4}$ K^{-1}, as determined through a series of measurements observing the temperature-dependent spectral shift of a characteristic Fabry-Perot transmission spectrum (described below), from waveguide Fabry-Perot cavities fabricated on the same InGaAsP-InP substrate.

Figure 7.7 contains a portion of the switch's normalized transmission spectrum near $\lambda = 1569$ nm, plotted as a function of the electrical power dissipated within a single MZI electrode. The 0.45 nm wavelength span shown corresponds to one free spectral range of the racetrack resonator. Transmission is shown for TE polarized input in Fig. 7.7(a), and for TM polarization in Fig. 7.7(b). When the MZI was biased such that the magnitude of the coupling coefficient $|\kappa|$ is approximately zero, the transmission was rendered relatively flat across the spectral region shown. As $|\kappa|$ was increased by further increasing the electrical power, the waveguide-resonator sys-

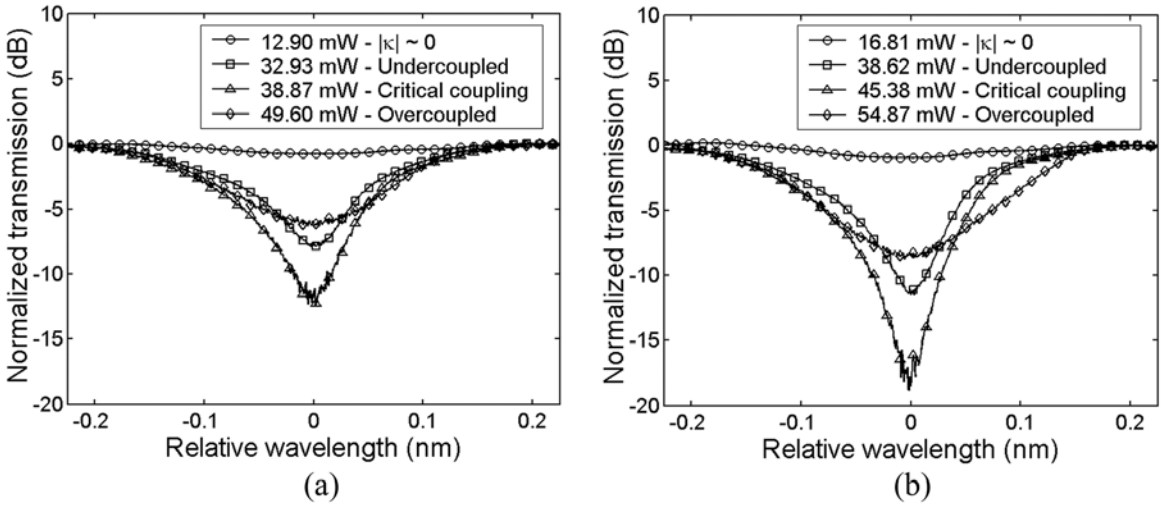

Figure 7.7: Normalized transmission illustrating the behavior of a single racetrack resonance as the MZI is tuned. The electrical power dissipated in a single MZI electrode appears in the legend. (a) TE polarized input, maximum contrast ∼12 dB, switching power ∼ 26 mW. (b) TM polarized input, maximum contrast ∼18.5 dB, switching power ∼ 29 mW.

tem was tuned through undercoupled, critically coupled, and overcoupled conditions. These conditions are characterized by the coupling coefficient being less than, equal to, or greater than the round-trip resonator loss, respectively [155]. On resonance, a contrast ratio of approximately 12 dB and 18.5 dB was observed near critical coupling, for TE and TM polarizations, respectively. The lower extinction observed for TE polarization is likely due to a slight polarization-dependent deviation from the ideal 50%/50% power splitting ratio in the MMI 3 dB couplers. The spectral width of the transmission null broadens as $|\kappa|$ increases with increasing electrical power, corresponding to the expected reduction in the loaded Q. From the linewidth at critical coupling, the unloaded intrinsic resonator Q was estimated to be 1.9×10^4 for TE and 1.7×10^4 for TM. The slight asymmetry seen in the lineshapes of the transmission minima in Fig. 7.7 was attributed to the influence of Fabry-Perot reflections from the cleaved facets of the device.

The switching power ΔP_{cr}, i.e., the power necessary to switch the hybrid device from the $|\kappa| \sim 0$ ($|t| \sim 1$) condition to critical coupling, was approximately 26 mW

for TE and 29 mW for TM. By operating the MZI in the push-pull configuration, the switching power may be further reduced by a factor of two. In comparison, conventional MZI modulators fabricated on the same substrate with identical electrode lengths were observed to have a (single electrode) switching power of $\Delta P_\pi \sim 40$ mW. Using Eq. 7.9 with $\Delta\phi = \pi$ gives a value of approximately 400 K/W for the thermal impedance Z_T. The observed reduction in switching power can be expressed following Eq. 7.7 as $(\Delta P_{cr}/\Delta P_\pi)_{\mathrm{TE}} = 0.65$, and $(\Delta P_{cr}/\Delta P_\pi)_{\mathrm{TM}} = 0.73$. This implies $\alpha_{\mathrm{TE}} \sim 0.52$, and $\alpha_{\mathrm{TM}} \sim 0.41$. Again, the lower switching power of the hybrid MZI/racetrack resonator switch compared to the conventional MZI is strictly due to the unique geometry for controlled waveguide-resonator coupling used here.

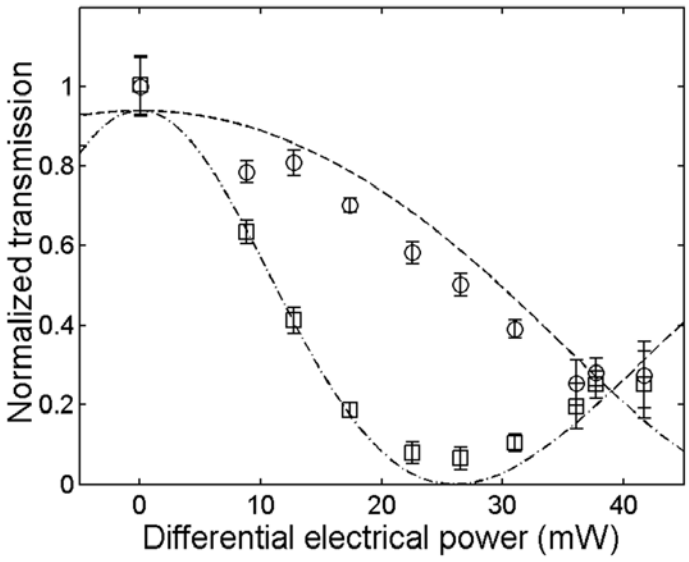

Figure 7.8: Normalized transmission as a function of differential electrical power, for TE-polarized input. Square-marker data and dash-dotted guide-line represent on-resonance transmission. Circle-marker data and dashed guide-line indicate off-resonance transmission. Guide-lines are theoretical plots for $\alpha = 0.50$ and $\Delta P_\pi = 39$ mW.

Figure 7.8 plots the normalized transmission for TE-polarized input, both on-resonance (square markers, $\theta = 2m\pi$, $m = 1, 2, 3...$ in Eq. 7.3) and off-resonance (circle markers, $\theta = (2m-1)\pi$, $m = 1, 2, 3...$ in Eq. 7.3), as a function of the differential electrical power applied to a single MZI electrode. The power axis has been

shifted by the power required to bias the hybrid switch to the state of maximum transmission. The error bars on the data account for uncertainty in the transmitted optical power due to undesirable superimposed Fabry-Perot resonances from reflections at the cleaved facets of the device. The dash-dotted and dashed guide-lines are theoretical plots for the on-resonance and off-resonance transmission, respectively, with $\alpha = 0.50$ and $\Delta P_\pi = 39$ mW, and can be seen to follow the trends in the data. These values are in reasonable agreement with $\alpha_{\mathrm{TE}} \sim 0.52$ and $\Delta P_\pi \sim 40$ mW as obtained above, and suggest that a reasonable estimate of α can be made using the measured switching power reduction ratio $\Delta P_{cr}/\Delta P_\pi$. The theoretical guide-lines fit the data best with a maximum normalized transmission of 0.94 at a differential electrical power of zero, suggesting that the MZI itself may have some additional losses, i.e. $|\kappa|^2 + |t|^2 < 1$. These additional losses, as well as the relatively low values of α suggested by the data, can be attributed to scattering losses in the racetrack resonator, and to free carrier loss from a non-optimal MZI electrode structure.

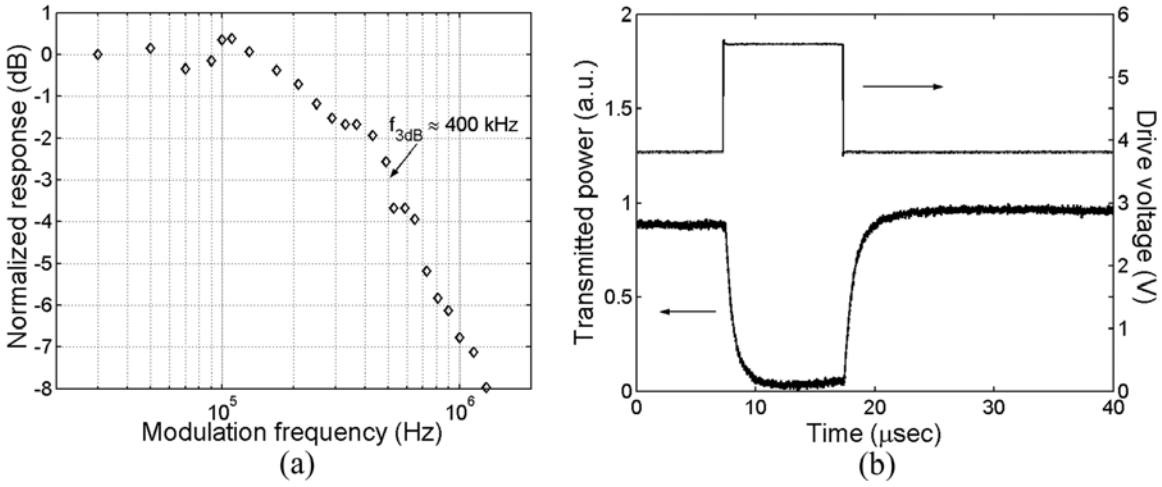

Figure 7.9: (a) Frequency domain modulation response, showing 3 dB small-signal bandwidth of 400 kHz. (b) Temporal response of normalized optical transmission to a 10 μs voltage pulse, showing a rise/fall time of $\sim$1.8 μs.

To investigate the small signal modulation response, the TE polarized input was tuned into resonance with a racetrack mode at $\lambda = 1564.54$ nm. One arm of the MZI was driven at a bias power of $\sim$30 mW, superimposed with a 0.12 mW average

power sinusoidal signal from a function generator. The transmitted optical power was coupled into a single mode optical fiber, amplified by an erbium doped fiber amplifier (EDFA), and fed into a fast photodetector. A lock-in amplifier was used to extract the signal component at the modulation frequency, while this frequency was stepped from 30 kHz – 1.3 MHz. The resulting modulation response is plotted in Fig. 7.9(a), showing a 3 dB bandwidth of approximately 400 kHz. Figure 7.9(b) shows the time domain response to a 10 μs, 1.75 V peak-to-peak pulse. For the bias conditions shown, the positive-going voltage pulse gates the optical output into the OFF state by switching the hybrid MZI/resonator to the critical coupling condition. Fitting an exponential decay to the normalized transmission, a 10%-90% rise/fall time of $\sim$1.8 μs is extracted. In comparison with previous studies of integrated thermooptic switches, for example the silicon-on-insulator (SOI) MZI devices in [154], the InP-based hybrid switch presented here exhibits a $\sim$4x faster rise time and a switching power 60% smaller, while using a shorter thermooptic drive section. The improved performance is due to the unique hybrid design, in addition to enhanced thermal conductance in the InP structure. This switch may be easily integrated with other passive or thermally tunable InP-based devices, for compact photonic integrated systems.

The response time of the device can be improved dramatically by reduction of the large series resistance of the current path through the MZI waveguide. This can be achieved by inclusion of a p-i-n diode in the semiconductor epitaxial substrate, and would permit fast free carrier dispersion effects [111] to become the dominant mechanism for control of the relative phase $\Delta\phi$. In addition, straightforward reduction of the racetrack resonator loss can result in further reduction of the switching power by as much as an order of magnitude [152]. Decreasing the length of the racetrack, and/or introduction of optical amplification within the resonator, can accomplish this goal. However, the latter option requires the difficult challenge of simultaneously integrating both active and passive regions on the same substrate. Various techniques, including semiconductor regrowth [156], quantum well intermixing [157–159], and vertical coupling between active/passive layers [160, 161], constitute potential means of achieving this integration.

7.4 Measurement of waveguide thermooptic coefficients

The thermooptic coefficient $\partial n/\partial T$ of a given bulk material describes how its refractive index changes with temperature. In semiconductor materials, several physical processes can contribute to the observed thermooptic effects, including the temperature dependence of the bandgap due to thermal expansion and/or changes in phonon populations [104], lattice stress-optical effects due to thermal expansion mismatch in epitaxial structures [91], and changes in the thermal population of the conduction and valence bands with free carriers [110]. However, for the majority of semiconductors, the shrinkage of the bandgap with increasing temperature is generally the dominant contribution. As the temperature increases, the optical absorption edge moves to lower energy, and therefore, by the Kramers-Kronig relations [162], the refractive index of the material increases for wavelengths within the semiconductor bandgap, giving the thermooptic coefficient a positive sign. Although tabulated values of $\partial n/\partial T$ do not exist for arbitrary $In_{1-x}Ga_xAs_yP_{1-y}$ alloy compositions, the necessary coefficients may be estimated by interpolating the more readily available [38] values of $\partial n/\partial T$ for the constituent binary alloys InAs, InP, GaAs, GaP, using Vegard's Law [163].

In semiconductor optical waveguides, the core and cladding are typically composed of heterogeneous alloys, and the relevant thermooptic coefficient is not that of any particular layer, but rather the coefficient for the effective index of the optical mode itself, $\partial n_{eff}/\partial T$, as illustrated in Eq. 7.9. In general, $\partial n_{eff}/\partial T$ depends upon the specific cross-sectional geometry and material composition of the waveguide. While it is possible to estimate $\partial n_{eff}/\partial T$ by computing modal confinement factors and averaging the respective bulk thermooptic coefficients in each layer over the waveguide mode profile, a more accurate numerical value can be found by measuring $\partial n_{eff}/\partial T$ directly. This may be accomplished by examining the thermal dependence of the transmission spectrum of a Fabry-Perot (FP) passive filter, formed by a straight semiconductor waveguide with end facets cleaved perpendicular to the waveguide axis.

Consider a typical FP transmission spectrum as shown in Fig. 7.10, with successive longitudinal modes labelled λ_{m-1}, λ_m, λ_{m+1}, ..., (m integer) obtained at a temperature T. Upon changing the temperature of the entire FP cavity to T', using a thermoelectric cooler (TEC), for example, the transmission spectrum is red shifted by less than one FSR, with longitudinal modes labelled λ'_{m-1}, λ'_m, λ'_{m+1}, and so on. The resonance conditions for the modes at λ_m and λ'_m, neglecting thermal expansion

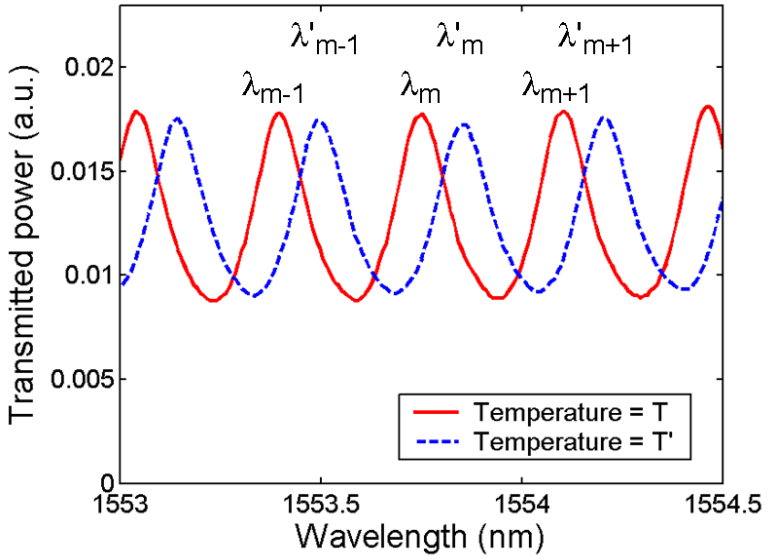

Figure 7.10: Illustration of Fabry-Perot transmission spectra taken at temperatures T and T'. The spectrum at T' is redshifted with respect to the spectrum at T.

of the FP cavity, are given by

$$\beta(\lambda_m, T)L = \frac{2n_{eff}(\lambda_m, T)L}{\lambda_m} = m\pi \tag{7.10}$$

$$\beta(\lambda'_m, T')L = \frac{2n_{eff}(\lambda'_m, T')L}{\lambda'_m} = m'\pi, \tag{7.11}$$

where the modal propagation constant β and effective index n_{eff} have been expressed as functions of the wavelength λ and temperature T. Subtracting Eq. 7.10 from Eq. 7.11, assuming $m' = m$, and expanding $n_{eff}(\lambda'_m, T')$ in a Taylor series to first order

in λ and T as

$$n_{eff}(\lambda_m', T') = n_{eff}(\lambda_m, T) + \Delta\lambda_m \left.\frac{\partial n_{eff}}{\partial \lambda}\right|_{\lambda_m} + \Delta T \left.\frac{\partial n_{eff}}{\partial T}\right|_{T}, \tag{7.12}$$

gives

$$\frac{\partial n_{eff}}{\partial T} = \frac{n_g(\lambda_m, T)}{\lambda_m}\frac{\Delta\lambda_m}{\Delta T} = \frac{n_g(\lambda_m, T)}{\lambda_m}\frac{\partial\lambda_m}{\partial T}. \tag{7.13}$$

In Eq. 7.13, $\Delta\lambda = \lambda_m' - \lambda_m$, $\Delta T = T' - T$, and $n_g(\lambda_m, T)$ is the group index, given by

$$n_g(\lambda_m, T) = n_{eff}(\lambda_m, T) - \lambda_m \left.\frac{\partial n_{eff}}{\partial \lambda}\right|_{\lambda_m}. \tag{7.14}$$

The group index can be calculated using numerical mode solver techniques (such as the finite-difference technique discussed in Chapter 6), by taking into account the dispersion of the various materials in the waveguide core and cladding [95]. Assuming that n_g is independent of temperature and wavelength is sufficient to obtain a first-order estimate for $\partial n_{eff}/\partial T$. Thus, $\partial n_{eff}/\partial T$ may be calculated by measuring $\partial\lambda_m/\partial T$ from a series of FP spectra taken at various temperatures.

In practical thermooptic devices, such as the hybrid MZI/racetrack switch discussed above, only a portion of the device is heated to produce a change in the modal effective index, i.e., through ohmic heating by current injected into an on-chip electrode. Consider for example, a two-section FP cavity, having an active heated section of length L_a, and a passive unheated section of length L_p, where $L = L_a + L_p$. The general resonance condition for a longitudinal mode with wavelength λ_m in a two-section FP cavity, assuming no reflection occurs at the interface between the heated and unheated sections, is given by

$$\frac{2n_{eff,a}(\lambda_m, T)L_a}{\lambda_m} + \frac{2n_{eff,p}(\lambda_m, T)L_p}{\lambda_m} = m\pi, \tag{7.15}$$

where $n_{eff,a}(\lambda_m, T)$ and $n_{eff,p}(\lambda_m, T)$ are the modal effective indexes in the heated and unheated sections, respectively. Following a procedure similar to that outlined

above for the case of heating the entire FP cavity results in the expression

$$\frac{\partial n_{eff,a}}{\partial T} = \frac{L}{L_a}\frac{n_g(\lambda_m, T)}{\lambda_m}\frac{\partial \lambda_m}{\partial T}, \tag{7.16}$$

where the heated and unheated sections are assumed to have the same group index n_g.

When working with thermooptic devices actuated by on-chip electrodes, the temperature change of the waveguide is in general unknown. Rather, it is more feasible to measure the shift in the FP resonance at λ_m with the electrical power P_e dissipated in the heated section, i.e., $\partial\lambda_m/\partial P_e$, as opposed to $\partial\lambda_m/\partial T$. The change in temperature is related to the change in dissipated electrical power by the thermal impedance Z_T, as

$$\Delta T = Z_T \Delta P_e. \tag{7.17}$$

Substituting Eq. 7.17 into Eq. 7.16, and equating the resulting expression with Eq. 7.13 permits calculation of the thermal impedance, as

$$Z_T = \frac{L}{L_a}\left(\frac{\partial \lambda_m}{\partial T}\right)^{-1}_{TEC}\left(\frac{\partial \lambda_m}{\partial P_e}\right)_{on-chip}, \tag{7.18}$$

where the subscripts TEC and $on-chip$ have been used to label the cases of changing the temperature of the entire FP cavity or just a portion of the cavity length, respectively.

Chapter 8

Chemical and biological sensing applications of optical microcavities

8.1 Introduction

The application of miniaturized photonic devices for the detection of extremely small quantities of chemical or biological agents has enabled significant progress toward the realization of compact "lab-on-a-chip" systems. One possible means of using optical components to monitor various chemical and biological systems is via sensing of the refractive index. For example, chemical and biological compounds are often used and handled in liquid form, after being dissolved within an appropriate solvent solution. The dissolved compound and solvent are together referred to as the analyte. Small relative changes in the concentration or composition of the solute will in general have an effect upon the refractive index of the analyte.

Optical waveguide devices can perform as ideal refractive index sensors, particularly when the analyte becomes a physical part of the device, such as the waveguide cladding. In this case, the evanescent portion of the guided mode within the cladding will overlap spatially and interact with the analyte. Any changes occurring in the refractive index of the analyte will consequently result in modification of the optical path length seen by the propagating waveguide mode. This change in the optical path length can in general manifest itself as a change in one or more measurable

transfer characteristics of the device, such as the optical power transmission or reflection coefficients. A number of refractive index sensors based upon optical waveguide geometries have been demonstrated, including etched core fiber Bragg grating [164], directional coupler [165], and Mach-Zehnder interferometer [166] configurations.

The use of optical microcavities as sensors presents intrinsic advantages over non-resonant waveguide-based geometries. These advantages stem from the fact that light resonant with the microcavity can be trapped for times long compared with the cavity round-trip time. Therefore, the effective interaction length of the optical mode with the surrounding analyte becomes proportional to the physical cavity length multiplied by a factor on the order of the finesse of the cavity [18]. This resonant enhancement permits high sensitivity to changes in the local refractive index using an optical device occupying only a fraction of the physical footprint consumed by typical waveguide-based devices. For microcavity sensors, changes in the round-trip optical path length results in red or blue shifting of the supported mode spectrum.

While the ability to measure an alteration of the environmental refractive index does not necessarily provide information regarding the exact nature of the substance responsible for the change, chemical and/or biological specificity can be achieved by careful preparation of the sensing surfaces, such that only a single compound will bind to the optical interaction region. For example, for biosensors in which detection of a specific antibody is desired, functionalization of the sensing surfaces with an antigen having an affinity for only the desired antibody can ensure that the optical transfer characteristics of the sensor will only be affected by the presence of the matching antibody [167, 168]. Biosensors of this type are referred to as affinity-based biosensors.

Therefore, the chief concern is to identify particular optical device geometries demonstrating externally observable transfer characteristics having high sensitivity to small changes in the local refractive index. This chapter will discuss the advantages of both annular Bragg resonators and the hybrid Mach-Zehnder/racetrack resonator switch in the context of optical microcavity refractive index sensing applications.

8.2 ABR microcavity sensors

8.2.1 Passive vs. active microcavity sensor designs

Development of refractive index sensors based on semiconductor optical microcavities has largely focused upon passive cavity designs. For example, the whispering gallery modes in cylindrical ring and disk microcavities [26, 169], and the localized defect modes in 2D photonic crystal membrane structures [170], have been proposed and demonstrated in sensing applications. As mentioned above, changes in the refractive index of the analyte induce a corresponding red or blue shift of the cavity mode spectrum. The resolution Δn_0 of a passive microcavity sensor, i.e., the minimum detectable change in the refractive index of the analyte, is determined by both the sensitivity S and the smallest resolvable shift in the resonant wavelength. The sensitivity S is defined as the observed shift in the wavelength of a given cavity mode per unit change in the refractive index, and is a function of the microcavity geometry and the resulting optical spatial mode profile. The minimum resolvable spectral shift is generally determined by the larger of the instrument resolution (i.e., tunable laser, resolution typically on the order of 1 pm), or the linewidth $\Delta\lambda_{FWHM}$ of the cavity resonance. The linewidth $\Delta\lambda_{FWHM}$ (inversely proportional to the square of the cavity quality factor Q) is in general larger than the instrument resolution, and therefore plays a dominant role in determining Δn_0.

On the other hand, active cavity sensors, which are fabricated using an amplifying semiconductor medium to achieve optical gain and ultimately laser oscillation, have received less attention. For example, some limited work incorporating photoluminescent porous silicon DBR microcavity sensors [171], and photonic crystal defect laser refractive index [172] and nanoparticle [173] sensors has been demonstrated. Active designs, particularly those with sufficient gain and intrinsic cavity losses low enough to achieve laser oscillation, theoretically possess the advantage that the emission linewidth $\Delta\lambda_{laser}$ is subject to a large degree of spectral narrowing above threshold [120, 121]. Comparing passive and active cavities with similar unsaturable losses, the above threshold active cavity emission linewidth can be much narrower than the

passive cold-cavity spectral linewidth. Therefore, assuming that the shift of the active cavity emission spectrum can be measured with an instrument-limited resolution similar to that in the passive cavity case, it follows that active cavity sensors should demonstrate an improved index resolution Δn_0 with respect to passive cavity sensors.

8.2.2 Demonstration of ABR laser refractive index sensors

For conventional TIR-based microring or microdisk resonators, a surrounding analyte will only interact with the small evanescent tails of the optical mode penetrating beyond the high index waveguide core layer. The small overlap between the mode and the analyte will consequently limit the sensitivity to changes in refractive index. In contrast, distributed Bragg reflector type microresonators such as the ABR radial defect resonator geometry possess a unique optical mode profile, which can be advantageous for enhancing the sensitivity [174]. For example, the ABR defect mode profile carries significant field amplitude within the low index layers adjacent to the high index defect layer, as a result of the oscillatory manner in which the field decays into the cylindrical Bragg reflectors. With appropriate ABR design and fabrication, the analyte can completely fill the low index regions, leading to a larger interaction volume and an enhanced degree of sensitivity in comparison to a conventional resonator of similar dimensions.

In order to demonstrate this concept, a set of ABR radial defect microcavities was fabricated along with several conventional microring resonators, using the active InGaAsP quantum well membrane material and epitaxial transfer process described in Chapter 4. The grating design of the ABR sensor devices used here was quite similar to that of the vertically emitting lasers described in Chapter 5, with 5 and 10 periods in the inner and outer Bragg reflectors, respectively. The ABR devices were designed to support a mode with $m = 9$ at a wavelength $\lambda = 1570$ nm, with mixed-order Bragg reflectors and a first-order defect layer. The conventional index-guided microring resonators had a bend radius of 5 μm, similar to the defect radius of the ABR devices, and a width of 1 μm. All high index semiconductor layers

were assumed to have an effective index of 2.8, and an index of 1.56 was used for the low index regions and ABR trenches. After the patterned 250 nm semiconductor membrane was transferred to a sapphire substrate, the low index trenches in the ABR devices and the areas surrounding the microring resonators were cleared of the NOA 73 UV curable transfer polymer using an NF_3/O_2 ICP-RIE etch, thus permitting the analyte to efficiently surround the semiconductor devices from three sides.

The devices were mounted to a specially designed clamp, and immersed within a glass cuvette filled with an index matching fluid (Cargille Labs) which served as the analyte. The devices were exposed to a total of five fluids, having refractive indexes in the range of 1.52-1.60, in steps of 0.02. The series was chosen to have an average refractive index of 1.56, matching that used for the low index layers during the device design. The fluid refractive index values were standardized by the manufacturer at $\lambda = 5893$ Å and 25 °C, with an error of ± 0.0002. The fluids were composed of a mixture of organic liquids, and were found to be compatible with both the InGaAsP membrane and the NOA 73 adhesive. During prolonged exposures, the index matching fluids caused a slight swelling of the adhesive, but this was not found to affect any of the observed device optical characteristics. The mounted sample, clamp, and cuvette were thoroughly rinsed with acetone and isopropyl alcohol between immersion in each fluid, to ensure that no residues of the previous fluid remained.

For each matching fluid, both the radial defect ABR and conventional microring devices were optically pumped above laser threshold, and the emission spectra were recorded. The optical characterization apparatus was very similar to that shown in Chapter 5, with the difference that the Ti:sapphire mode locked pump laser was tuned to a center wavelength of $\lambda_p = 980$ nm. The incident pump power used for each index matching fluid was $\sim$2.5 mW for the ABR devices, and $\sim$3.5 mW for the microrings. Figures 8.1(a)-(b) plot the set of spectra obtained for the ABR and conventional microring sensors, respectively, with the fluid refractive index indicated in the legend. As expected, the lasing wavelengths were redshifted as the refractive index of the fluid was increased.

Figure 8.2 compares the relative shift in the peak wavelength for both the ABR

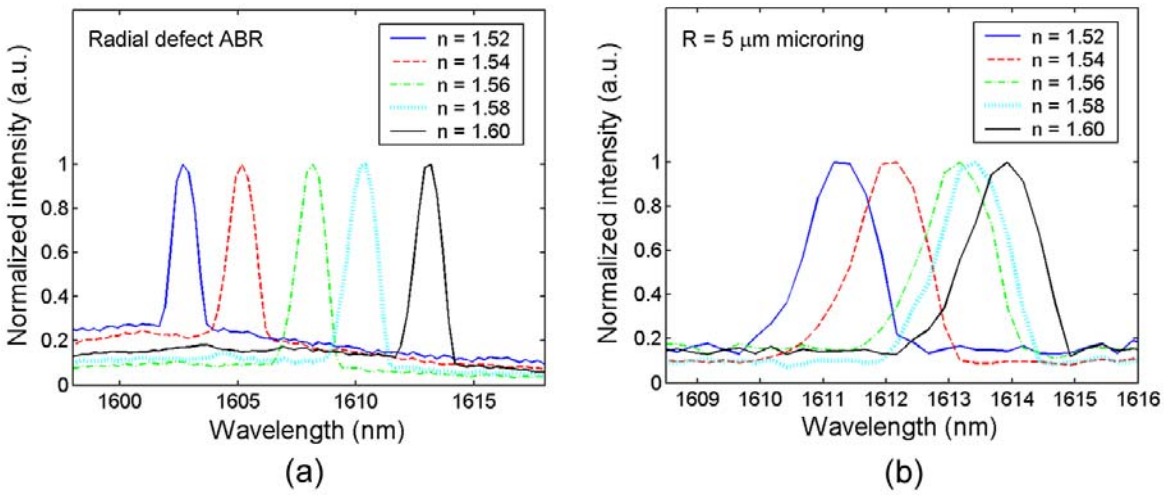

Figure 8.1: Laser emission spectra as a function of refractive index of the surrounding fluid, indicated in the legend. Spectra have been normalized to the peak values. (a) Spectra for radial defect ABR sensor. (b) Spectra for conventional TIR-guided microring with 5 μm bend radius.

and microring devices, as a function of fluid refractive index. The blue diamonds and solid red line refer to the ABR sensor, and the magenta circles and black dotted line refer to the microring. While the lasing wavelength of the ABR sensor redshifted by more than 10 nm through a total refractive index change of 0.08, the microring sensor lasing wavelength shifted by only 2.6 nm under the same conditions. The sensitivity evaluated from the slope of each numerical fit line was $S_{ABR} = 130$ nm and $S_r = 33$ nm, for the ABR and microring sensors, respectively, illustrating that the ABR geometry tested here exhibits a sensitivity approximately four times that of the microring.

An estimate of the index resolution Δn_0 possible for each sensor configuration can be obtained by considering the measured sensitivity in conjunction with the FWHM emission linewidth of the lasing modes shown in Fig. 8.1. The linewidths for both the ABR and microring sensors are $\Delta\lambda_{laser} \sim 1.4$ nm. Assuming that a spectral shift of 0.14 nm can be easily detected, the ABR and microring sensors have an estimated resolution of $\Delta n_{0,ABR} \sim 1 \times 10^{-3}$ and $\Delta n_{0,r} \sim 4 \times 10^{-3}$, respectively. However, it

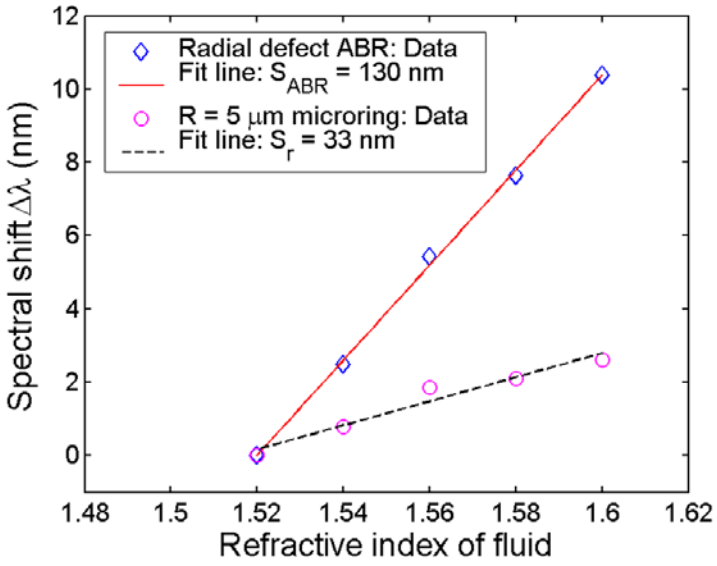

Figure 8.2: Relative spectral shift of lasing wavelength as a function of index matching fluid refractive index. Comparison of data from radial defect ABR and microring sensors demonstrates a four times greater sensitivity for the ABR device.

is important to point out that the observed linewidths, and thus the resolution, are limited by dynamic broadening effects occurring due to optical pumping with ∼100 fs pulses, as discussed in Chapter 5. By increasing the duration of the excitation pulses to ∼1 μs, reduction of the linewidth and improvement of the resolution by one to two orders of magnitude should be possible. However, the onset of thermal effects degrading the optical gain may limit the effectiveness of this approach. Further improvements in the resolution can be obtained through reduction of the fundamental laser emission linewidth, by optimization of the ABR cavity design to obtain lower cavity losses and a higher cold-cavity Q.

Although the observed ABR laser linewidths are larger than those measured for various ultrahigh-Q passive microcavities demonstrated recently [35, 116], they are comparable if not smaller than the linewidths demonstrated for the active photonic crystal laser sensor devices reported in [172], despite suffering from enhanced dynamic broadening. Nevertheless, the above measurements serve to illustrate the inherent advantages of ABR microcavities in sensor applications. Further improvements in

sensitivity can be made by designing an ABR microcavity to support an optical mode with peak field amplitude located within a low-index radial defect [50], which will consequently increase the interaction volume with the analyte.

It is worthwhile to note that the choice of a low-index crystalline sapphire transfer substrate is not critical to the success of the polymer epitaxial transfer technique employed in the fabrication of the ABR microcavity sensors, nor does it impact the device optical properties. The low-index NOA 73 adhesive layer is thick enough to optically isolate the ABR devices, and as such, common substrates such as a Si wafer or glass slide would function equally well as sapphire. Indeed, the ability to epitaxially transfer ABR devices in single units or large arrays to any substrate creates the potential for integration and application of ABR microcavities as key elements within chemical and biological sensing systems incorporating microfluidic technology [175, 176].

8.3 Hybrid MZI/racetrack resonator sensors

8.3.1 Conventional MZI sensors

Conventional planar integrated MZIs have previously been demonstrated as refractive index sensors [166, 177]. In this application, the relative phase shift $\Delta\phi$ between the two MZI branches, and thus the optical power transmitted through the MZI, can be made a function of the environmental refractive index, via the modal effective index n_{eff}. During the sensor fabrication process, the interferometer's waveguiding layer is encapsulated by an upper cladding, everywhere isolating the optical mode from the surrounding environment. As shown in Fig. 8.3, a window in the upper cladding isolation layer over one arm of the MZI is then opened to create an active sensing region of length L_a, in which the evanescent tail of the waveguide mode may interact with an analyte. The other branch of the MZI remains optically isolated from the analyte, and serves as a reference.

The relative phase shift $\Delta\phi$ between the sensing and reference arms impacts the

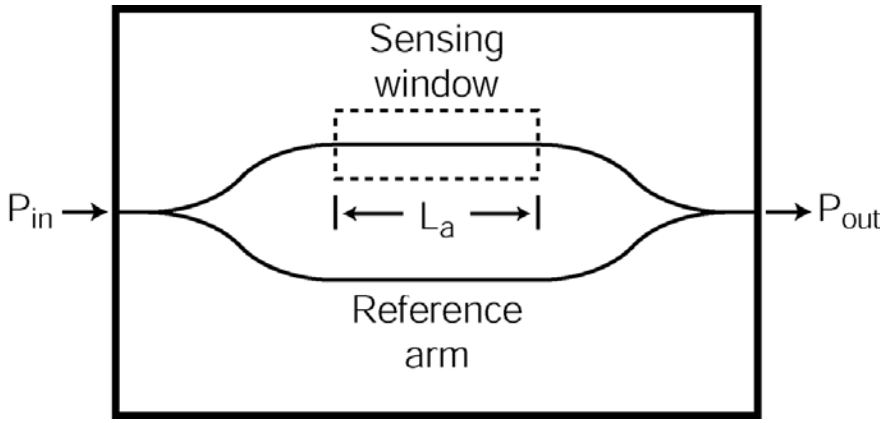

Figure 8.3: Schematic of a conventional Mach-Zehnder interferometric refractive index sensor. The analyte only interacts with the evanescent tail of the waveguide mode in the sensing window of length L_a in the upper branch. The resulting relative phase difference between the reference arm and the sensing arm modulates the transmitted power P_{out}.

normalized transmitted optical power T_{MZI} at the output, given by

$$\begin{aligned} T_{MZI} &= \left.\frac{P_{out}}{P_{in}}\right|_{MZI} = \cos^2\left(\frac{\Delta\phi}{2}\right) \\ &= \cos^2\left(\frac{\pi L_a}{\lambda}\left(n_{eff,a} - n_{eff,ref}\frac{\Delta L}{L_a}\right) + \frac{\pi L_a}{\lambda}\Delta n_{eff,a}\right) \\ &= \cos^2\left(\frac{\phi_0 + \Delta\phi_a}{2}\right), \end{aligned} \tag{8.1}$$

where

$$\phi_0 = \frac{2\pi L_a}{\lambda}\left(n_{eff,a} - n_{eff,ref}\frac{\Delta L}{L_a}\right), \tag{8.2}$$

$$\Delta\phi_a = \frac{2\pi L_a}{\lambda}\Delta n_{eff,a}. \tag{8.3}$$

The relative phase in Eq. 8.1 has been expressed as the sum of a constant bias phase ϕ_0, and a term $\Delta\phi_a$ depending upon the change $\Delta n_{eff,a}$ in the modal effective index within the active sensing region. The bias phase depends upon the nominal effective indexes within the sensing and reference regions, $n_{eff,a}$ and $n_{eff,ref}$ respectively, as well as the physical path difference ΔL, which is the difference in the length between

complete lower branch and the portion of the upper branch in which the waveguide mode has $n_{eff,ref}$, i.e., the total length of the upper branch less the length of the sensing region.

Strictly speaking, the MZI sensor output quantified in Eq. 8.1 depends upon $\Delta n_{eff,a}$, not the desired quantity $\Delta n_{analyte}$. The degree to which $\Delta n_{eff,a}$ depends upon $\Delta n_{analyte}$ varies depending upon the specific details of both the geometrical and dielectric design of the optical waveguide within the sensing region. However, it is in general possible to express $\Delta n_{eff,a}$ in terms of $\Delta n_{analyte}$ and a modal confinement factor Γ_{xy} [178], as

$$\Delta n_{eff,a} = \Gamma_{xy} \Delta n_{analyte}, \tag{8.4}$$

where

$$\Gamma_{xy} = \frac{\dfrac{n_{analyte}}{n_{eff,a}} \int\limits_{analyte} |E_a(x,y)|^2 \, dxdy}{\int |E_a(x,y)|^2 \, dxdy}. \tag{8.5}$$

In Eq. 8.5, $n_{analyte}$ is the nominal refractive index of the analyte, and $E_a(x,y)$ is the transverse field profile of the optical mode within the sensing region, calculated assuming a dielectric material with index $n_{analyte}$ occupies the appropriate part of the cross-section. The integral in the numerator is carried out over the fraction of the waveguide cross-section occupied by the analyte, and the integral in the denominator is carried out over the whole cross-section. It is assumed that any changes in the refractive index of the analyte $\Delta n_{analyte}$ are sufficiently small so as to have only a perturbative effect, allowing the unperturbed values of $n_{eff,a}$ and $E_a(x,y)$ to be used in estimating $\Delta n_{eff,a}$.

The sensitivity S_{MZI} of the MZI sensor is defined as the change in normalized transmission per unit change in the refractive index. Specifically, S_{MZI} is given by the absolute value of the derivative of Eq. 8.1 with respect to $\Delta n_{analyte}$, evaluated at $\Delta n_{analyte} = 0$. Substitution of Eq. 8.4 and differentiation gives

$$\begin{aligned} S_{MZI} &= \left| \frac{dT_{MZI}}{d\Delta n_{analyte}} \right|_{\Delta n_{analyte}=0} = \left| \frac{dT_{MZI}}{d\Delta\phi_a} \frac{d\Delta\phi_a}{d\Delta n_{eff,a}} \frac{d\Delta n_{eff,a}}{d\Delta n_{analyte}} \right|_{\Delta n_{analyte}=0} \\ &= \frac{\pi L_a \Gamma_{xy}}{\lambda} \left| \sin(\phi_0) \right|. \end{aligned} \tag{8.6}$$

Equation 8.6 shows that S_{MZI} can be maximized by designing or operating the MZI sensor with a bias phase of $\phi_0 = \pi/2$. This corresponds to biasing the MZI at the quadrature point at $T_{MZI} = 0.5$, where the slope of the MZI output characteristic is largest. The above expression also indicates that the sensitivity can be improved by increasing the sensing window length and/or increasing the confinement factor.

The resolution $\Delta n_{0,MZI}$ of the MZI sensor, i.e., the minimum detectable change in the refractive index of the analyte, is determined by both the sensitivity S_{MZI} and the instrument-limited signal-to-noise ratio for the measurement of changes in the normalized transmission T_{MZI}. Index resolution values on the order of 10^{-6}-10^{-7} have previously been reported for MZI-based devices with sensing regions 15-20 mm long [166, 177].

8.3.2 Enhancement of sensitivity using the hybrid MZI/racetrack resonator switch geometry

Recalling that the hybrid MZI/racetrack resonator geometry discussed in Chapter 7 exhibited a significant reduction in the phase shift required for ON-OFF switching when compared to a conventional MZI, it follows that a proportional enhancement in the sensitivity and resolution may be expected when the hybrid device is utilized as a passive cavity sensor. An illustration of the hybrid switch sensor geometry is shown in Fig. 8.4, demonstrating how the optical device may be integrated with a microfluidic flow circuit [179, 180] for the manipulation of single or multiple chemical/biological analytes. As with the conventional MZI sensor device discussed above, a segment of one MZI branch having length L_a overlaps with the flow channel, forming the sensing region. The other MZI branch and the racetrack resonator can be intentionally encapsulated and optically isolated from the analyte by the microfluidic circuit's substrate.

The normalized optical power transmitted through the hybrid sensor at a wave-

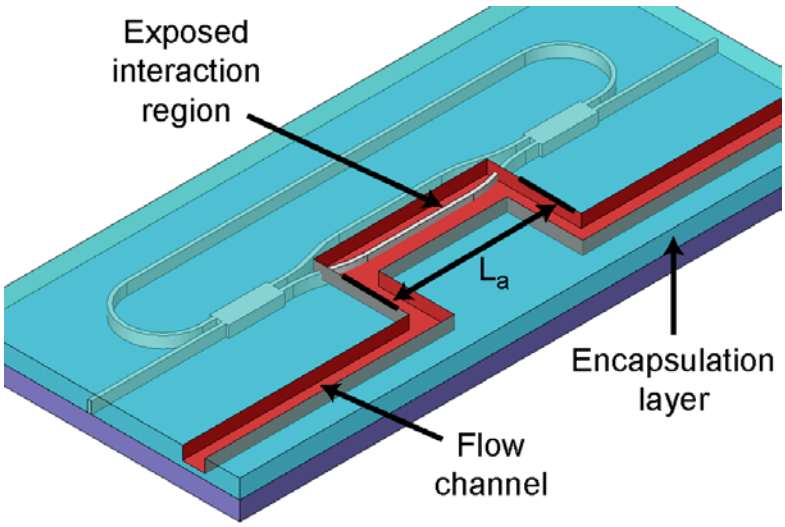

Figure 8.4: Schematic of a hybrid MZI/racetrack resonator sensor integrated with a microfluidic flow channel for analyte delivery. One branch of the MZI is exposed to the analyte within the interaction region of length L_a.

length on resonance with the racetrack is given by

$$T_{hybrid} = \left.\frac{P_{out}}{P_{in}}\right|_{hybrid} = \frac{\left[\alpha - \left|\cos\left(\frac{\phi_0 + \Delta\phi_a}{2}\right)\right|\right]^2}{\left[1 - \alpha\left|\cos\left(\frac{\phi_0 + \Delta\phi_a}{2}\right)\right|\right]^2}, \tag{8.7}$$

where the definitions of ϕ_0 and $\Delta\phi_a$ are identical to those for the conventional MZI sensor, as per Eqs. 8.2-8.3. In Eq. 8.7, α is the round-trip transmissivity of the racetrack resonator, with $0 \leq \alpha \leq 1$. Figure 8.5(a) compares the normalized transmission for the hybrid sensor with $\alpha = 0.99$ with that for the conventional MZI sensor, as a function of the total relative phase $\Delta\phi = \phi_0 + \Delta\phi_a$. Given that the sensitivity is linearly proportional to the slope of the power transfer characteristic, Fig. 8.5(a) reveals that the hybrid switch sensor should have a larger sensitivity to a change in the index of the analyte than the conventional MZI sensor, when biased for operation within the region of large slope near $\Delta\phi = 0$.

The ratio of the sensitivities evaluated at $T_{hybrid} = T_{MZI} = 1/2$ gives a measure of the sensitivity enhancement factor provided by the hybrid geometry. Using

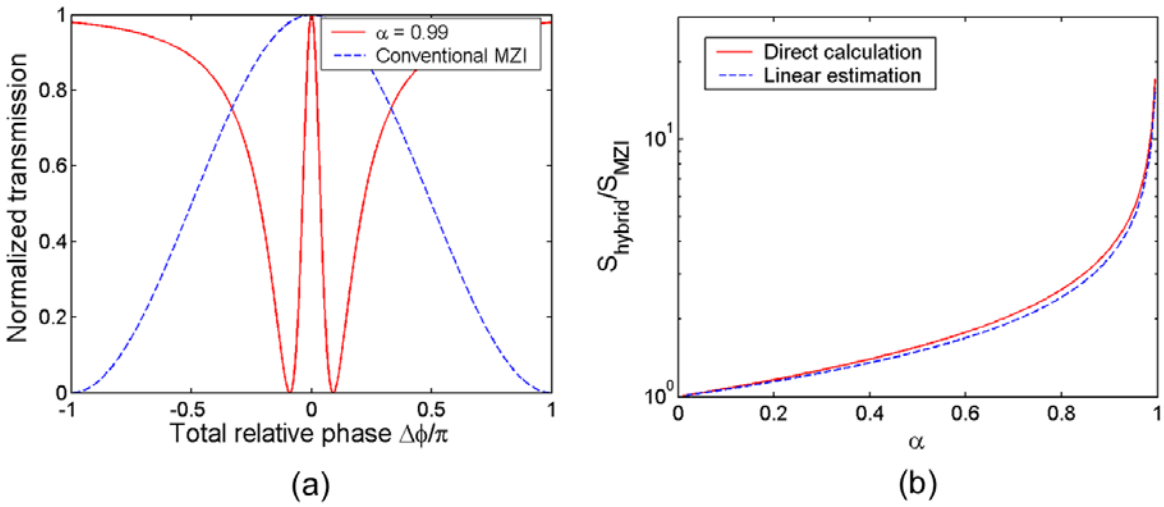

Figure 8.5: (a) Normalized optical transmission as a function of total relative phase, for hybrid switch sensor with $\alpha = 0.99$ and conventional MZI sensor. (b) Calculated and estimated sensitivity enhancement factor for the hybrid sensor geometry. An enhancement factor of ∼10 is obtained for $\alpha = 0.99$.

expressions for the hybrid switch similar to those in Eq. 8.6, the ratio is given by

$$\frac{S_{hybrid}}{S_{MZI}} = \left| \frac{dT_{hybrid}/d\Delta\phi}{dT_{MZI}/d\Delta\phi} \right|_{T=1/2}, \tag{8.8}$$

which can be evaluated numerically. Alternatively, a crude linear estimation of the slope of each curve in Fig. 8.5(a) gives

$$\left. \frac{S_{hybrid}}{S_{MZI}} \right|_{estimated} = \frac{\pi}{2\cos^{-1}(\alpha)}, \tag{8.9}$$

which is recognized as the inverse of the switching power reduction ratio $\Delta P_{cr}/\Delta P_{\pi}$ derived in Chapter 7.

The sensitivity enhancement factor S_{hybrid}/S_{MZI} of Eq. 8.8 was calculated for values of α between 0 and 1, and is plotted in Fig. 8.5(b). The estimated expression in Eq. 8.9 is also shown, and closely approximates the directly calculated curve. For $\alpha = 0.99$, an enhancement factor of approximately 10 is obtained. Therefore, given an index resolution of $\Delta n_{0,MZI} = 10^{-7}$ as previously reported for the conventional MZI

sensor, the hybrid MZI/racetrack switch geometry could be expected to resolve index changes to a resolution of at least $\Delta n_{0,hybrid} = 10^{-8}$, when using a comparably sized sensing region. Alternatively, the sensing region of the hybrid sensor could be reduced in length by the enhancement factor, obtaining the same resolution but using only a fraction of the substrate area occupied by a conventional MZI device. It is worthwhile to point out that the optical modulation bandwidth limitations imposed by the use of high Q resonators are not expected to influence the performance of sensors based on the hybrid MZI/racetrack resonator geometry, given that the properties of the analyte will typically vary at frequencies in the range of Hz-kHz.

In the event that changes in the absorptivity of the analyte provide a more appropriate measure of the chemical/biological compound's composition and/or concentration than changes in its refractive index, the optical transmission characteristics of a coupled waveguide-resonator system can similarly be modulated by the analyte's effect upon the racetrack transmission coefficient α. Changes in α can, for example, be achieved by introducing a chemical or biological compound with significant absorption at the resonant wavelength(s) into proximity with the evanescent tail of the optical mode in the racetrack resonator [26]. The expression for the transmitted power in Eq. 8.7 is invariant upon exchange of the positions of α and the absolute value of the coupler transmission coefficient $|t| = |\cos[(\phi_0 + \Delta\phi_a)/2]|$, and therefore, similar sensor performance should be expected under these conditions. Furthermore, for an analyte prepared with fluorescent labels tagging the chemical/biological compounds of interest, changes in the resonator absorption may also be accompanied by changes in the excitation of fluorescence. The fluorescence signal can be resonantly enhanced by the high intensity of pump light building up within the racetrack resonator, providing the basis for high-resolution fluorescence-based sensors [27].

Chapter 9

Conclusions

In the preceding chapters, the design, fabrication, and characterization of several unique semiconductor optical microcavity architectures based upon the InGaAsP-InP material system has been described.

First, the annular Bragg resonator, a novel ring resonator geometry in which radial optical confinement is provided by diffraction from a set of cylindrical Bragg gratings, was described and demonstrated. A transfer matrix formalism for analyzing multi-layer cylindrically symmetric structures was outlined, and was used to show that the ideal cylindrical grating possesses layers with chirped thickness along the radial direction, in contrast with the uniform quarter-wavelength layers typical of Bragg reflectors in Cartesian coordinates. After numerically investigating several cylindrical grating designs and the optical properties of radial defect ABR microcavities, a versatile process for the fabrication of ABR devices was presented. This process made use of electron beam lithography and several reactive ion etching steps to pattern a thin InGaAsP quantum well membrane. A technique for epitaxial transfer of the membrane to a sapphire transfer substrate was developed, making use of a polymer adhesive for bonding. Several vertically emitting ABR lasers with sub-milliwatt thresholds were then demonstrated using pulsed optical excitation, including ring defect and pillar nanocavity resonators. Multiple characteristics of the laser emission were investigated, including emission spectra, polarization, infrared near field images, and sensitivity to fabrication process variations.

Second, a coupled waveguide-resonator geometry having applications to low power

optical switching was presented. This geometry made use of a Mach-Zehnder interferometer as an electrically tunable coupler to an integrated racetrack resonator. The fundamental advantage predicted by the analysis of this hybrid MZI/racetrack resonator structure was the reduction of the switching power in comparison with a conventional Mach-Zehnder interferometer. The hybrid switch was based upon a conventional TIR-guided microcavity design, and was fabricated using InGaAsP-InP passive semiconductor waveguide material. Characterization of the device's DC and dynamic optical transmission performance revealed high-contrast switching capabilities with the predicted reduction in required power, as well as microsecond thermooptic response time.

Finally, both the ABR microcavity and hybrid switch architecture were shown to have excellent potential in applications as chemical and biological sensors. Both classes of device were shown to be highly sensitive to very small fluctuations in the refractive index of a chemical or biological analyte in which they are immersed.

Directions for the future study of semiconductor ABR microcavities can include the introduction of additional degrees of optical feedback into the existing radial defect ABR geometries. While the devices explored in the previous chapters employed cylindrical Bragg gratings arranged to provide radial Bragg reflection, it is also possible to periodically modulate the dielectric medium along the azimuthal coordinate. If such an azimuthal Bragg grating is appropriately introduced in order to have some degree of interaction with the ABR defect mode, 2D optical Bragg feedback, both radial and azimuthal, may be achievable. Several "gear ABR" structures of this sort, named after the gear tooth perturbation applied to the semiconductor rings, have been fabricated, and are shown in Fig. 9.1. In Figs. 9.1(a)-(b) an azimuthal grating having 100 nm tooth depth is applied to only the radial defect layer, and in Figs. 9.1(c)-(d) a perturbation of similar size is applied to the defect layer and the two adjacent rings in the internal and external Bragg reflectors. By designing the azimuthal grating to have a number of periods N_g equal to twice the azimuthal number m of

the ABR defect mode divided by an integer, i.e.,

$$-\frac{2m}{M} = N_g, \tag{9.1}$$

it is possible to induce coupling between the two degenerate counter-propagating ABR defect modes having $\pm m$. In Eq. 9.1, $M = \pm 1, \pm 2, \pm 3, ...$ is the azimuthal Bragg reflection order. This inter-modal coupling is expected to lift the degeneracy of the modes phase-matched to the azimuthal grating, resulting in the splitting of their resonant wavelengths. In addition, the presence of the azimuthal grating may contribute to a significant increase in the optical losses experienced by the non-phase-matched resonant modes with $|m| \neq MN_g/2$, relative to those modes which are phase-matched. Therefore, the introduction of even a small azimuthal perturbation can potentially serve to restrict the number of oscillating modes observed for gear ABR lasers in comparison to the radial defect ABR lasers discussed in Chapter 5, perhaps resulting in single-mode laser operation for a range of pump powers significantly above threshold. The validity of these concepts is supported by previous work considering the operation of a "microgear" laser, which incorporates an azimuthal grating patterned around the periphery of a pedestal whispering gallery microdisk resonator [181, 182]. The subtleties of the design of gear ABR microcavities, including the influence of the azimuthal grating strength and spatial profile, as well as their experimental performance in terms of azimuthal mode selection, remain to be investigated.

Furthermore, the concept of azimuthal modulation of the ABR geometry can also be framed within the context of 2D cylindrical photonic crystal structures. Two types of photonic crystal structures commonly occurring in the literature are based upon thin semiconductor membranes perforated with a lattice of air holes, having either square [136] or hexagonal [83] symmetry. Resonant optical cavities are formed by creating a point or line defect within the lattice, by removing or altering the size of one or more of the air holes. By extension, the structures shown in Figs. 9.2(a)-(b) comprise the cylindrical analogues of Cartesian coordinate-based square and hexagonal lattice photonic crystal defect cavities, respectively, and are thus referred to as pho-

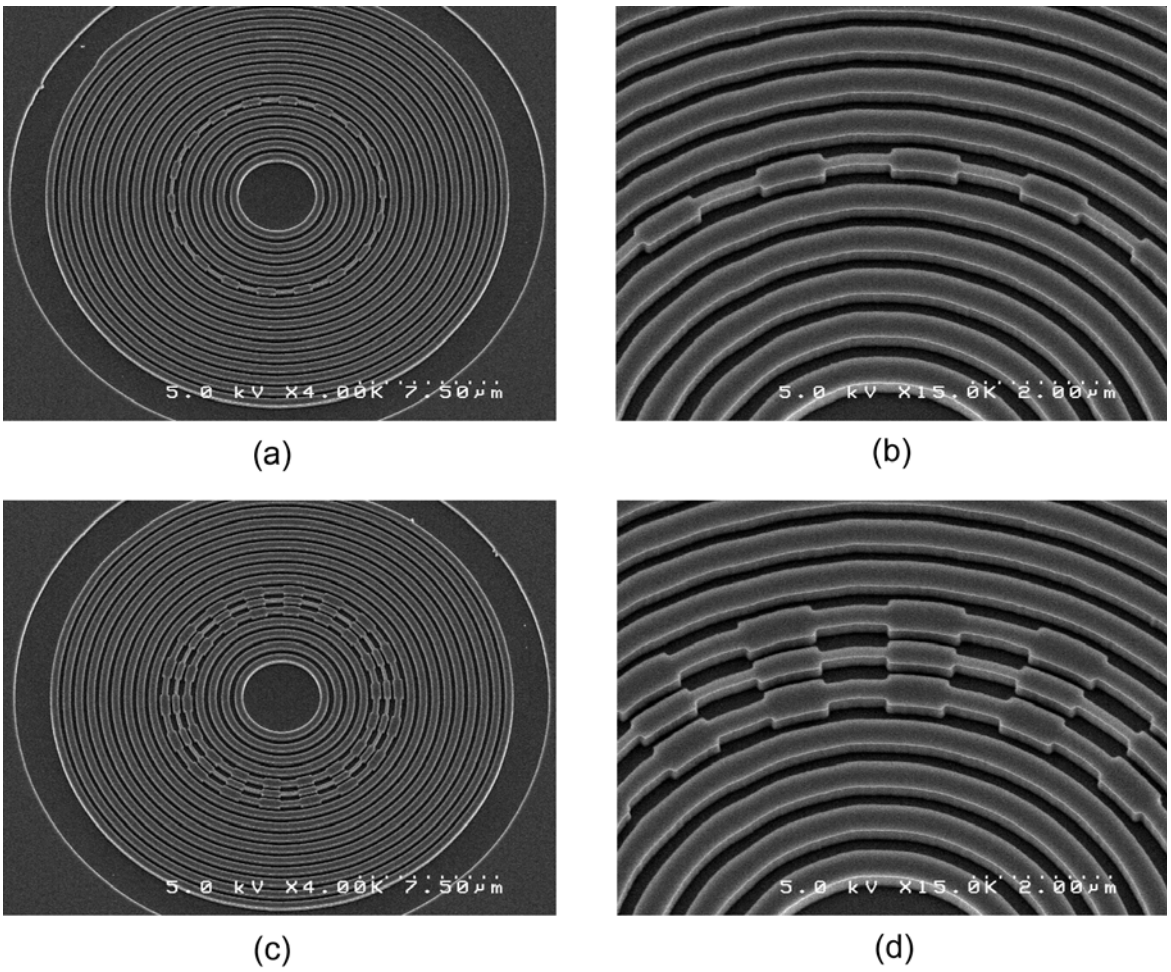

Figure 9.1: The InGaAsP gear ABR structures in the SEM images shown here were obtained by modifying the semiconductor layer widths of the nominal mixed-order grating, first-order radial defect ABR microcavity structures discussed in previous chapters. Within each azimuthally perturbed ring, the nominal ring width was changed by ± 50 nm within the "high" and "low" index regions, respectively, for a net tooth depth of 100 nm. The azimuthal gratings shown were designed with $N_g = 18$, serving as first-order Bragg reflectors for the $m = \pm 9$ ABR defect modes. Azimuthal gratings were patterned into only the radial defect layer of the device in (a)-(b), and into the defect layer and two adjacent semiconductor rings of the device in (c)-(d).

tonic crystal (PC) ABRs. The optical modes of such structures are radially confined within the central high-index region by cylindrical Bragg reflection from the array of air holes, and have been analyzed using a coupled mode approach [52, 135] similar to that applied in the case of the Bragg pillar ABR geometry discussed in Chapter 5. In general, the number of azimuthal periods N_g within the PC ABR structure is chosen to be much larger than the azimuthal number m of the optical mode to be confined, i.e., $N_g \gg m$, and also chosen such that $N_g \neq -2m/M$, in order to avoid the inter-modal coupling described by Eq. 9.1 for $m \neq 0$. Specifically, the devices in Fig. 9.2 are designed to support the non-degenerate $m = 0$ cylindrical mode, having the smallest mode volume within such a structure. Photonic crystal ABR devices also possess the added advantage that the InGaAsP patterned membrane maintains physical continuity throughout the device, and therefore, such microcavities could be fabricated using the traditional air-suspended membrane undercutting process common to many 2D photonic crystals. Of course, the polymer epitaxial transfer method developed here remains as another viable fabrication alternative for PC ABR devices. The experimental demonstration of optical confinement and lasing from the various possible PC ABR lattices represents a promising direction for further consideration.

Another relevant topic of study includes improving the heat-sinking of the InGaAsP quantum well membrane, in order to reduce thermal effects and allow for optical excitation with long duty cycles, or even continuous wave pumping. Steady state (or quasi-steady state) operation of ABR lasers would help to significantly reduce the laser linewidth, permitting much higher resolution in refractive index sensing applications. Finally, the epitaxial transfer process utilized for the fabrication of ABR microcavities can be exploited to transfer arrays of such resonators onto glass substrates, facilitating their integration with compact microfluidic circuits for complete "lab-on-a-chip" systems.

For the hybrid switch, future work could potentially include the introduction of an optical amplifier section into the racetrack resonator. The round-trip cavity losses could be offset by such an amplifier, resulting in a greater reduction of the required electrical switching power. Possible means of introducing such an amplifying section

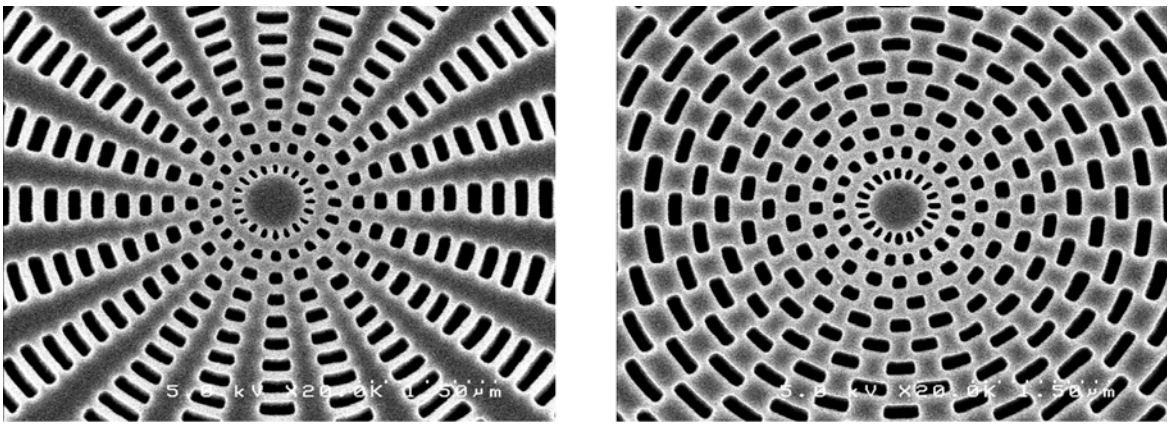

Figure 9.2: SEM images of several InGaAsP photonic crystal ABR devices. These resonators have been designed to support the $m = 0$ cylindrical mode within the central high-index disk, and employ azimuthal modulation with $N_g = 20$. The cylindrical patterning of the air holes is chosen in analogy to the square lattice (a), and the hexagonal lattice (b) forms commonly used in Cartesian coordinate-based 2D photonic crystal structures.

could involve semiconductor regrowth or quantum well intermixing techniques. In addition, using an appropriately designed p-i-n diode semiconductor optical waveguide structure could potentially provide an improvement in the switching response time, by replacing thermooptic effects with faster free carrier dispersion effects as the mechanism for control of the waveguide-resonator coupling coefficient.

Bibliography

[1] L. Rayleigh, "The Problem of the Whispering Gallery," in *Scientific Papers*, vol. 5, pp. 617–620. Cambridge University, Cambridge, England, 1912.

[2] E. A. J. Marcatili, "Bends in optical dielectric guides," *Bell Syst. Tech. J.* **47**, pp. 2103–2132, 1969.

[3] J. Haavisto and G. A. Pajer, "Resonance effects in low-loss ring waveguides," *Opt. Lett.* **5**(12), pp. 510–512, 1980.

[4] K. Honda, E. M. Garmire and K. E. Wilson, "Characteristics of an integrated optics ring resonator fabricated in glass," *J. Lightwave Technol.* **2**(5), pp. 714–719, 1984.

[5] M. K. Smit, E. C. M. Pennings and H. Blok, "A normalized approach to the design of low-loss optical waveguide bends," *J. Lightwave Technol.* **11**(11), pp. 1737–1742, 1993.

[6] T. Krauss, P. J. R. Laybourn and J. Roberts, "CW operation of semiconductor ring lasers," *Electron. Lett.* **26**(25), pp. 2095–2097, 1990.

[7] S. L. McCall, A. F. J. Levi, R. E. Slusher, S. J. Pearton and R. A. Logan, "Whispering-gallery mode microdisk lasers," *Appl. Phys. Lett.* **60**(3), pp. 289–291, 1992.

[8] A. F. J. Levi, S. L. McCall, S. J. Pearton and R. A. Logan, "Room temperature operation of submicrometre radius disk laser," *Electron. Lett.* **29**(18), pp. 1666–1667, 1993.

[9] L. F. Stokes, M. Chodorow and H. J. Shaw, "All-single-mode fiber resonator," *Opt. Lett.* **7**(6), pp. 288–290, 1982.

[10] B. E. Little, S. T. Chu, H. A. Haus, J. Foresi and J.-P. Laine, "Microring resonator channel dropping filters," *J. Lightwave Technol.* **15**(6), pp. 998–1005, 1997.

[11] A. Yariv, "Universal relations for coupling of optical power between microresonators and dielectric waveguides," *Electron. Lett.* **36**(4), pp. 321–322, 2000.

[12] D. Rafizadeh, J. P. Zhang, S. C. Hagness, A. Taflove, K. A. Stair, S. T. Ho and R. C. Tiberio, "Waveguide-coupled AlGaAs/GaAs microcavity ring and disk resonators with high finesse and 21.6-nm free spectral range," *Opt. Lett.* **22**(16), pp. 1244–1246, 1997.

[13] B. E. Little, S. T. Chu, W. Pan, D. Ripin, T. Kaneko and E. Ippen, "Vertically coupled glass microring resonator channel dropping filters," *IEEE Photon. Technol. Lett.* **11**(2), pp. 215–217, 1999.

[14] J. C. Knight, G. Cheung, F. Jacques and T. A. Birks, "Phase-matched excitation of whispering-gallery-mode resonances by a fiber taper," *Opt. Lett.* **22**(15), pp. 1129–1131, 1997.

[15] M. Borselli, K. Srinivasan, P. E. Barclay and O. Painter, "Rayleigh scattering, mode coupling, and optical loss in silicon microdisks," *Appl. Phys. Lett.* **85**(17), pp. 3693–3695, 2004.

[16] P. P. Absil, J. V. Hryniewicz, B. E. Little, R. A. Wilson, L. G. Joneckis and P.-T. Ho, "Compact microring notch filters," *IEEE Photon. Technol. Lett.* **12**(4), pp. 398–400, 2000.

[17] B. E. Little, J. S. Foresi, G. Steinmeyer, E. R. Thoen, S. T. Chu, H. A. Haus, E. P. Ippen, L. C. Kimerling and W. Greene, "Ultra-compact Si-SiO2 microring resonator optical channel dropping filters," *IEEE Photon. Technol. Lett.* **10**(4), pp. 549–551, 1998.

[18] J. E. Heebner and R. W. Boyd, "Enhanced all-optical switching by use of a nonlinear fiber ring resonator," *Opt. Lett.* **24**(12), pp. 847–849, 1999.

[19] C. K. Madsen and J. H. Zhao, *Optical Filter Design and Analysis: A Signal Processing Approach.*, Wiley-Interscience, New York, 1999.

[20] P. Rabiei and W. H. Steier, "Tunable polymer double micro-ring filters," *IEEE Photon. Technol. Lett.* **15**(9), pp. 1255–1257, 2003.

[21] G. T. Paloczi, J. Scheuer and A. Yariv, "Compact microring-based wavelength-selective inline optical reflector," *IEEE Photon. Technol. Lett.* **17**(2), pp. 390–392, 2005.

[22] M. T. Hill, H. J. S. Dorren, T. de Vries, X. J. M. Leijtens, J. H. den Besten, B. Smalbrugge, Y.-S. Oei, H. Binsma, G.-D. Khoe and M. K. Smit, "A fast low-power optical memory based on coupled micro-ring lasers," *Nature.* **432**(7014), pp. 206–209, 2004.

[23] T. A. Ibrahim, W. Cao, Y. Kim, J. Li, J. Goldhar, P.-T. Ho and C. H. Lee, "All-optical switching in a laterally coupled microring resonator by carrier injection," *IEEE Photon. Technol. Lett.* **15**(1), pp. 36–38, 2003.

[24] P. P. Absil, J. V. Hryniewicz, B. E. Little, P. S. Cho, R. A. Wilson, L. G. Joneckis and P.-T. Ho, "Wavelength conversion in GaAs micro-ring resonators," *Opt. Lett.* **25**(8), pp. 554–556, 2000.

[25] B. Liu, A. Shakouri and J. E. Bowers, "Passive microring-resonator-coupled lasers," *Appl. Phys. Lett.* **79**(22), pp. 3561–3563, 2001.

[26] R. W. Boyd and J. E. Heebner, "Sensitive disk resonator photonic biosensor," *Appl. Opt.* **40**(31), pp. 5742–5747, 2001.

[27] S. Blair and Y. Chen, "Resonant-enhanced evanescent-wave fluorescence biosensing with cylindrical optical cavities," *Appl. Opt.* **40**(4), pp. 570–582, 2001.

[28] J. E. Heebner and R. W. Boyd, "'Slow' and 'fast' light in resonator-coupled waveguides," *J. Mod. Opt.* **49**(14-15), pp. 2629–2636, 2002.

[29] J. K. S. Poon, J. Scheuer, Y. Xu and A. Yariv, "Designing coupled-resonator optical waveguide delay lines," *J. Opt. Soc. Am. B.* **21**(9), pp. 1665–1673, 2004.

[30] K. Jinguji, "Synthesis of coherent two-port optical delay-line circuit with ring waveguides," *J. Lightwave Technol.* **14**(8), pp. 1882–1898, 1996.

[31] M. S. Rasras, C. K. Madsen, M. A. Capuzzo, E. Chen, L. T. Gomez, E. J. Laskowski, A. Griffin, A. Wong-Foy, A. Gasparyan, A. Kasper, J. Le Grange and S. S. Patel, "Integrated resonance-enhanced variable optical delay lines," *IEEE Photon. Technol. Lett.* **17**(4), pp. 834–836, 2005.

[32] L. V. Hau, S. E. Harris, Z. Dutton and C. H. Behroozi, "Light speed reduction to 17 meters per second in an ultracold atomic gas," *Nature.* **397**(6720), pp. 594–598, 1999.

[33] D. D. Smith and H. Chang, "Coherence phenomena in coupled optical resonators," *J. Mod. Opt.* **51**(16-18), pp. 2503–2513, 2004.

[34] A. B. Matsko, A. A. Savchenkov, D. Strekalov, V. S. Ilchenko and L. Maleki, "Interference effects in lossy resonator chains," *J. Mod. Opt.* **51**(16-18), pp. 2515–2522, 2004.

[35] D. K. Armani, T. J. Kippenberg, S. M. Spillane and K. J. Vahala, "Ultra-high-Q toroid microcavity on a chip," *Nature.* **421**(6926), pp. 925–928, 2003.

[36] T. J. Kippenberg, S. M. Spillane, D. K. Armani and K. J. Vahala, "Ultralow-threshold microcavity Raman laser on a microelectronic chip," *Opt. Lett.* **29**(11), pp. 1224–1226, 2004.

[37] T. J. Kippenberg, S. M. Spillane and K. J. Vahala, "Kerr-nonlinearity optical parametric oscillation in an ultrahigh-Q toroid microcavity," *Phys. Rev. Lett.* **93**(8), pp. 083904, 2004.

[38] V. Swaminathan, "Chapter 1: Properties of InP and Related Materials," in *Indium Phosphide and Related Materials: Processing, Technology, and Devices*, A. Katz, Ed. Artech, Boston, 1991.

[39] M. Toda, "Single-mode behavior of a circular grating for potential disk-shaped DFB lasers," *IEEE J. Quantum Electron.* **26**(3), pp. 473–481, 1990.

[40] T. Erdogan and D. G. Hall, "Circularly symmetric distributed feedback semiconductor laser: an analysis," *J. Appl. Phys.* **68**(4), pp. 1435–1444, 1990.

[41] X. H. Zheng and S. Lacroix, "Mode coupling in circular-cylindrical system and its application to fingerprint resonators," *J. Lightwave Technol.* **8**(10), pp. 1509–1516, 1990.

[42] T. Erdogan and D. G. Hall, "Circularly symmetric distributed feedback laser: coupled mode treatment of TE vector fields," *IEEE J. Quantum Electron.* **28**(3), pp. 612–623, 1992.

[43] A. A. Tovar and G. H. Clark, "Concentric-circle-grating, surface-emitting laser beam propagation in complex optical systems," *J. Opt. Soc. Am. A.* **14**(12), pp. 3333–3340, 1997.

[44] M. A. Kaliteevski, R. A. Abram, V. V. Nikolaev and G. S. Sokolovski, "Bragg reflectors for cylindrical waves," *J. Mod. Opt.* **46**(5), pp. 875–890, 1999.

[45] C. Wu, M. Svilans, M. Fallahi, T. Makino, J. Glinski, C. Maritan and C. Blaauw, "Optically pumped surface-emitting DFB GaInAsP/InP lasers with circular grating," *Electron. Lett.* **27**(20), pp. 1819–1821, 1991.

[46] X. M. Gong, A. K. Chan and H. F. Taylor, "Lateral mode discrimination in surface emitting DBR lasers with cylindrical symmetry," *IEEE J. Quantum Electron.* **30**(5), pp. 1212–1218, 1994.

[47] D. Labilloy, H. Benisty, C. Weisbuch, T. F. Krauss, C. J. M. Smith, R. Houdre and U. Oesterle, "High-finesse disk microcavity based on a circular Bragg reflector," *Appl. Phys. Lett.* **73**(10), pp. 1314–1316, 1998.

[48] A. Shaw, B. Roycroft, J. Hegarty, D. Labilloy, H. Benisty, C. Weisbuch, T. F. Krauss, C. J. M. Smith, R. Stanley, R. Houdre and U. Oesterle, "Lasing properties of disk microcavity based on a circular Bragg reflector," *Appl. Phys. Lett.* **75**(20), pp. 3051–3053, 1999.

[49] D. Ochoa, R. Houdre, M. Ilegems, H. Benisty, T. F. Krauss and C. J. M. Smith, "Diffraction of cylindrical Bragg reflectors surrounding an in-plane semiconductor microcavity," *Phys. Rev. B.* **61**(7), pp. 4806–4812, 2000.

[50] J. Scheuer and A. Yariv, "Annular Bragg defect mode resonators," *J. Opt. Soc. Am. B.* **20**(11), pp. 2285–2291, 2003.

[51] J. Scheuer and A. Yariv, "Two-dimensional optical ring resonators based on radial Bragg resonance," *Opt. Lett.* **28**(17), pp. 1528–1530, 2003.

[52] J. Scheuer and A. Yariv, "Coupled-waves approach to the design and analysis of Bragg and photonic crystal annular resonators," *IEEE J. Quantum Electron.* **39**(12), pp. 1555–1562, 2003.

[53] L. A. Coldren and S. W. Corzine, "Chapter 3: Mirrors and Resonators for Diode Lasers," in *Diode Lasers and Photonic Integrated Circuits*. Wiley-Interscience Publications, New York, 1995.

[54] P. Rabiei, W. H. Steier, C. Zhang and L. R. Dalton, "Polymer micro-ring filters and modulators," *J. Lightwave Technol.* **20**(11), pp. 1968–1975, 2002.

[55] T. Sadagopan, S. J. Choi, S. J. Choi, K. Djordjev and P. D. Dapkus, "Carrier-induced refractive index changes in InP-based circular microresonators for low-voltage high-speed modulation," *IEEE Photon. Technol. Lett.* **17**(2), pp. 414–416, 2005.

[56] S. T. Chu, W. Pan, S. Sato, T. Kaneko, B. E. Little and Y. Kokubun, "Wavelength trimming of a microring resonator filter by means of a UV sensitive polymer overlay," *IEEE Photon. Technol. Lett.* **11**(6), pp. 688–690, 1999.

[57] C. H. Cox, "Gain and noise figure in analogue fibre-optic links," *IEE Proc. J.* **139**(4), pp. 238–242, 1992.

[58] Y. Zhuang, W. S. C. Chang and P. K. L. Yu, "Peripheral-coupled-waveguide MQW electroabsorption modulator for near transparency and high spurious free dynamic range RF fiber-optic link," *IEEE Photon. Technol. Lett.* **16**(9), pp. 2033–2035, 2004.

[59] M. Nakamura, K. Aiki, J. Umeda and A. Yariv, "CW operation of distributed-feedback GaAs-GaAlAs diode lasers at temperatures up to 300 K," *Appl. Phys. Lett.* **27**(7), pp. 403–405, 1975.

[60] A. Yariv, "Chapter 16: Advanced Semiconductor Lasers: Quantum Well Lasers, Distributed Feedback Lasers, Vertical Cavity Surface Emitting Lasers," in *Optical Electronics in Modern Communications*. Oxford University Press, New York, 5th edition, 1997.

[61] A. Scherer, J. L. Jewell, M. Walther, J. P. Harbison and L. T. Florez, "Fabrication of low threshold voltage microlasers," *Electron. Lett.* **28**(13), pp. 1224–1226, 1992.

[62] P. Yeh, A. Yariv and E. Marom, "Theory of Bragg fiber," *J. Opt. Soc. Am.* **68**(9), pp. 1196–1201, 1978.

[63] A. Yariv, "Chapter 3: Propagation of Optical Beams in Fibers," in *Optical Electronics in Modern Communications*. Oxford University Press, New York, 5th edition, 1997.

[64] G. P. Agrawal, "Chapter 2: Optical Fibers," in *Fiber-Optic Communication Systems*. Wiley, New York, 2nd edition, 1997.

[65] A. Yariv, "Chapter 13: Propagation and Coupling of Modes in Optical Dielectric Waveguides - Periodic Waveguides," in *Optical Electronics in Modern Communications*. Oxford University Press, New York, 5th edition, 1997.

[66] J. Scheuer, W. M. J. Green, G. A. DeRose and A. Yariv, "InGaAsP annular Bragg lasers: theory, applications, and modal properties," *IEEE J. Sel. Top. Quantum Electron.* **11**(2), pp. 476–484, 2005.

[67] Y. Shani, R. Alferness, T. Koch, U. Koren, M. Oron, B. I. Miller and M. G. Young, "Polarization rotation in asymmetric periodic loaded rib waveguides," *Appl. Phys. Lett.* **59**(11), pp. 1278–1280, 1991.

[68] A. Adibi, R. K. Lee, A. Yariv and A. Scherer, "Properties of the slab modes in photonic crystal optical waveguides," *J. Lightwave Technol.* **18**(11), pp. 1554–1564, 2000.

[69] K. Kawano and T. Kitoh, "Chapter 2: Analytical Methods," in *Introduction to Optical Waveguide Analysis: Solving Maxwell's Equation and the Schodinger Equation*. Wiley-Interscience Publications, New York, 2001.

[70] M. Abramowitz and A. Stegun, Eds., *Handbook of Mathematical Functions*, Constable, New York, 1972.

[71] V. Jayaraman, A. Mathur, L. A. Coldren and P. D. Dapkus, "Extended tuning range in sampled grating DBR lasers," *IEEE Photon. Technol. Lett.* **5**(5), pp. 489–491, 1993.

[72] K. Utaka, S. Akiba, K. Sakai and Y. Matsushima, "lambda/4-shifted InGaAsP/InP DFB lasers," *IEEE J. Quantum Electron.* **22**(7), pp. 1042–1051, 1986.

[73] R. F. Kazarinov and C. H. Henry, "Second-order distributed feedback lasers with mode selection provided by first-order radiation losses," *IEEE J. Quantum Electron.* **21**(2), pp. 144–150, 1985.

[74] R. J. Noll and S. H. Macomber, "Analysis of grating surface emitting lasers," *IEEE J. Quantum Electron.* **26**(3), pp. 456–466, 1990.

[75] M. Kasraian and D. Botez, "Metal-grating-outcoupled, surface-emitting distributed-feedback diode lasers," *Appl. Phys. Lett.* **69**(19), pp. 2795–2797, 1996.

[76] A. Inoue, T. Iwashima, T. Enomoto, S. Ishikawa and H. Kanamori, "Optimization of fiber Bragg grating for dense WDM transmission system," *IEICE Trans. Electron.* **E81-C**(8), pp. 1209–1218, 1998.

[77] S. G. Johnson, M. Ibanescu, M. Skorobogatiy, O. Weisberg, T. D. Engeness, M. Soljacic, S. A. Jacobs, J. D. Joannopoulos and Y. Fink, "Low-loss asymptotically single-mode propagation in large-core OmniGuide fibers," *Opt. Express.* **9**(13), pp. 748–779, 2001.

[78] L. Raffaele, R. M. De La Rue, J. S. Roberts and T. F. Krauss, "Edge-emitting semiconductor microlasers with ultrashort-cavity and dry-etched high-reflectivity photonic microstructure mirrors," *IEEE Photon. Technol. Lett.* **13**(3), pp. 176–178, 2001.

[79] F. Pommereau, L. Legouezigou, S. Hubert, S. Sainson, J.-P. Chandouineau, S. Fabre and G.-H. Duan, "Fabrication of low loss two-dimensional InP photonic crystals by inductively coupled plasma etching," *J. Appl. Phys.* **95**(5), pp. 2242–2245, 2004.

[80] P.-A. Clerc, L. Dellmann, F. Gretillat, M.-A. Gretillat, P.-F. Indermuhle, S. Jeanneret, P. Luginbuhl, C. Marxer, T. L. Pfeffer, G.-A. Racine, S. Roth, U. Staufer, P. Thiebaud and N. F. de Rooij, "Advanced deep reactive ion etching: a versatile tool for microelectromechanical systems," *J. Micromech. Microeng.* **8**(4), pp. 272–278, 1998.

[81] S. Fan, P. R. Villeneuve, J. D. Joannopoulos and E. F. Schubert, "High extraction efficiency of spontaneous emission from slabs of photonic crystals," *Phys. Rev. Lett.* **78**(17), pp. 3294–3297, 1997.

[82] B. D'Urso, O. Painter, J. O'Brien, T. Tombrello, A. Yariv and A. Scherer, "Modal reflectivity in finite-depth two-dimensional photonic-crystal microcavities," *J. Opt. Soc. Am. B.* **15**(3), pp. 1155–1159, 1998.

[83] O. Painter, R. K. Lee, A. Scherer, A. Yariv, J. D. O'Brien, P. D. Dapkus and I. Kim, "Two-dimensional photonic band-gap defect mode laser," *Science.* **284**(5421), pp. 1819–1821, 1999.

[84] A. Scherer, O. Painter, B. D'Urso, R. Lee and A. Yariv, "InGaAsP photonic band gap crystal membrane microresonators," *J. Vac. Sci. Technol. B.* **16**(6), pp. 3906–3910, 1998.

[85] M. H. Shih, W. J. Kim, W. Kuang, J. R. Cao, H. Yukawa, S. J. Choi, J. D. O'Brien and P. D. Dapkus, "Two-dimensional photonic crystal Mach-Zehnder interferometers," *Appl. Phys. Lett.* **84**(4), pp. 460–462, 2004.

[86] H.-G. Park, S.-H. Kim, S.-H. Kwon, Y.-G. Ju, J.-K. Yang, J.-H. Baek, S.-B. Kim and Y.-H. Lee, "Electrically driven single-cell photonic crystal laser," *Science.* **305**(5689), pp. 1444–1447, 2004.

[87] S. Lin, J. G. Fleming and I. El-Kady, "Three-dimensional photonic-crystal emission through thermal excitation," *Opt. Lett.* **28**(20), pp. 1909–1911, 2003.

[88] C. C. Cheng, V. Arbet-Engels, A. Scherer and E. Yablonovich, "Nanofabricated three dimensional photonic crystals operating at optical wavelengths," *Physica Scripta.* **T68**, pp. 17–20, 1996.

[89] D. Schmitz, "Chapter 4: Low-Pressure MOVPE of InP-Based Compound Semiconductors," in *Indium Phosphide and Related Materials: Processing, Technology, and Devices*, A. Katz, Ed. Artech, Boston, 1991.

[90] K. Kawano and T. Kitoh, "Chapter 4: Finite-Difference Methods," in *Introduction to Optical Waveguide Analysis: Solving Maxwell's Equation and the Schodinger Equation*. Wiley-Interscience Publications, New York, 2001.

[91] L. A. Coldren and S. W. Corzine, "Appendix 11: Strained Bandgaps," in *Diode Lasers and Photonic Integrated Circuits*. Wiley-Interscience Publications, New York, 1995.

[92] G. E. Pikus and B. G. L., "Effect of deformation on the hole energy spectrum of germanium and silicon," *Sov. Phys. Solid State*. **1**, pp. 1502–1517, 1959.

[93] E. Yablonovich and E. O. Kane, "Reduction of lasing threshold current density by the lowering of valence band effective mass," *J. Lightwave Technol.* **4**(5), pp. 504–506, 1986.

[94] A. R. Adams, "Band-structure engineering for low-threshold high-efficiency semiconductor lasers," *Electron. Lett.* **22**(5), pp. 249–250, 1986.

[95] T. P. Pearsall, Ed., *GaInAsP Alloy Semiconductors*, Wiley, New York, 1982.

[96] S. R. Sakamoto, C. Ozturk, Y. T. Byun, J. Ko and N. Dagli, "Low-loss substrate-removed (SURE) optical waveguides in GaAs-AlGaAs epitaxial layers embedded in organic polymers," *IEEE Photon. Technol. Lett.* **10**(7), pp. 985–987, 1998.

[97] W. M. J. Green, J. Scheuer, G. DeRose and A. Yariv, "Vertically emitting annular Bragg lasers using polymer epitaxial transfer," *Appl. Phys. Lett.* **85**(17), pp. 3669–3671, 2004.

[98] W. M. J. Green, J. Scheuer, G. A. DeRose, A. Yariv and A. Scherer, "Assessment of lithographic process variation effects in InGaAsP annular Bragg resonator lasers," *J. Vac. Sci. Technol. B.* **22**(6), pp. 3206–3209, 2004.

[99] S. J. Pearton, U. K. Chakrabarti, A. Katz, F. Ren and T. R. Fullowan, "High-rate, anisotropic dry etching of InP in HI-based discharges," *Appl. Phys. Lett.* **60**(7), pp. 838–840, 1992.

[100] U. Niggebrugge, M. Klug and G. Garus, "A novel process for reactive ion etching on InP, using CH4/H2," *Inst. Phys. Conf. Ser.* **79**, pp. 367–372, 1985.

[101] V. M. Donnelly, D. L. Flamm, C. W. Tu and D. E. Ibbotson, "Temperature dependence of InP and GaAs etching in a chlorine plasma," *J. Electrochem. Soc.* **129**(11), pp. 2533–2537, 1982.

[102] L. A. Coldren and S. W. Corzine, "Chapter 4: Gain and Current Relations," in *Diode Lasers and Photonic Integrated Circuits*. Wiley-Interscience Publications, New York, 1995.

[103] S. M. Sze, "Chapter 1: Physics and Properties of Semiconductors - A Resume," in *Physics of Semiconductor Devices*. Wiley, New York, 2nd edition, 1981.

[104] N. W. Ashcroft and N. D. Mermin, "Chapter 28: Homogeneous Semiconductors," in *Solid State Physics*. Saunders College, Fort Worth, 1976.

[105] R. K. Lee, O. Painter, B. Kitzke, A. Scherer and A. Yariv, "Emission properties of a defect cavity in a two-dimensional photonic bandgap crystal slab," *J. Opt. Soc. Am. B.* **17**(4), pp. 629–633, 2000.

[106] M. Loncar, T. Yoshie, K. Okamoto, Y. Qiu, J. Vuckovic and A. Scherer, "Planar photonic crystal nanolasers (I): porous cavity lasers," *IEICE Trans. Electron.* **E87-C**(3), pp. 291–299, 2004.

[107] L. A. Coldren and S. W. Corzine, "Chapter 2: A Phenomenological Approach to Diode Lasers," in *Diode Lasers and Photonic Integrated Circuits*. Wiley-Interscience Publications, New York, 1995.

[108] E. K. Byrne, "Chapter 5: Doping of InP as Grown by Metalorganic Chemical Vapor Deposition," in *Indium Phosphide and Related Materials: Processing, Technology, and Devices*, A. Katz, Ed. Artech, Boston, 1991.

[109] B. R. Bennet, R. A. Soref and J. A. Del Alamo, "Carrier-induced change in refractive index of InP, GaAs, and InGaAsP," *IEEE J. Quantum Electron.* **26**(1), pp. 113–122, 1990.

[110] J. G. Mendoza-Alvarez, R. H. Yan and L. A. Coldren, "Contribution of the band-filling effect to the effective refractive-index change in double-heterostructure GaAs/AlGaAs phase modulators," *J. Appl. Phys.* **62**(11), pp. 4548–4553, 1987.

[111] C. H. Lee, P. S. Mak and A. P. DeFonzo, "Optical control of millimeter-wave propagation in dielectric waveguides," *IEEE J. Quantum Electron.* **16**(3), pp. 277–288, 1980.

[112] P. K. Tien, "Light waves in thin films and integrated optics," *Appl. Opt.* **10**(11), pp. 2395–2413, 1971.

[113] F. P. Payne and J. P. R. Lacey, "A theoretical-analysis of scattering loss from planar optical wave-guides," *Opt. Quantum Electron.* **26**(10), pp. 977–986, 1994.

[114] K. K. Lee, D. R. Lim, H.-C. Luan, A. Agarwal, J. Foresi and L. C. Kimerling, "Effect of size and roughness on light transmission in a Si/SiO2 waveguide: experiments and model," *Appl. Phys. Lett.* **77**(11), pp. 1617–1619, 2000.

[115] M. Haverlag, D. Vender and G. S. Oehrlein, "Ellipsometric study of silicon surface damage in electron cyclotron resonance plasma etching using CF4 and SF6," *Appl. Phys. Lett.* **61**(24), pp. 2875–2877, 1992.

[116] M. Borselli, T. J. Johnson and O. Painter, "Beyond the Rayleigh scattering limit in high-Q silicon microdisks: theory and experiment," *Opt. Express.* **13**(5), pp. 1515–1530, 2005.

[117] J. Vuckovic, *Photonic Crystal Structures for Efficient Localization or Extraction of Light*, Ph. D. Thesis, California Institute of Technology, 2002.

[118] S.-K. Kim, S.-H. Kim, G.-H. Kim, H.-G. Park, D.-J. Shin and Y.-H. Lee, "Highly directional emission from few-micron-size elliptical microdisks," *Appl. Phys. Lett.* **84**(6), pp. 861–863, 2004.

[119] S. V. Boriskina, T. M. Benson, P. Sewell and A. I. Nosich, "Highly efficient design of spectrally engineered whispering-gallery-mode microlaser resonators," *Opt. Quantum Electron.* **35**(4), pp. 545–559, 2003.

[120] A. L. Schawlow and C. H. Townes, "Infrared and optical masers," *Phys. Rev.* **112**(6), pp. 1940–1949, 1958.

[121] C. H. Henry, "Theory of the linewidth of semiconductor lasers," *IEEE J. Quantum Electron.* **18**(2), pp. 259–264, 1982.

[122] M. W. Fleming and A. Mooradian, "Fundamental line broadening of single-mode (GaAl)As diode lasers," *Appl. Phys. Lett.* **38**(7), pp. 511–513, 1981.

[123] A. Yariv, "Chapter 10: Noise in Optical Detection and Generation," in *Optical Electronics in Modern Communications*. Oxford University Press, New York, 5th edition, 1997.

[124] L. A. Coldren and S. W. Corzine, "Chapter 5: Dynamic Effects," in *Diode Lasers and Photonic Integrated Circuits*. Wiley-Interscience Publications, New York, 1995.

[125] J. P. van der Ziel, "Spectral broadening of pulsating Al(x)Ga(1-x)As double heterostructure lasers," *IEEE J. Quantum Electron.* **15**(11), pp. 1277–1281, 1979.

[126] B. W. Hakki, "Optical and microwave instabilities in injection lasers," *J. Appl. Phys.* **51**(1), pp. 68–73, 1980.

[127] K. Yee, "Numerical solution of initial boundary value problems involving maxwell's equations in isotropic media," *IEEE Trans. Antennas Propagat.* **14**(3), pp. 302–307, 1966.

[128] A. Taflove and S. C. Hagness, *Computational Electrodynamics: The Finite-Difference Time-Domain Method*, Artech House, Norwood, 2nd edition, 2000.

[129] J. Scheuer, W. M. J. Green, G. DeRose and A. Yariv, "Low threshold two-dimensional annular Bragg lasers," *Opt. Lett.* **29**(22), pp. 2641–2643, 2004.

[130] O. Painter, A. Husain, A. Scherer, P. T. Lee, I. Kim, J. D. O'Brien and P. D. Dapkus, "Lithographic tuning of a two-dimensional photonic crystal laser array," *IEEE Photon. Technol. Lett.* **12**(9), pp. 1126–1128, 2000.

[131] Y.-S. Choi, S.-K. Kim, S.-H. Kim, H.-G. Park, Y.-H. Lee, I. N. Kaiander, F. Hopfer, R. L. Sellin and D. Bimberg, "Lithographic tuning of photonic-crystal unit-cell resonators with InGaAs/GaAs quantum dots emitting at 1.2 um.," *J. Vac. Sci. Technol. B.* **23**(1), pp. 252–256, 2005.

[132] S. Yasin, D. G. Hasko and H. Ahmed, "Comparison of sensitivity and exposure latitude for polymethylmethacrylate, UVIII, and calixarene using conventional dip and ultrasonically assisted development," *J. Vac. Sci. Technol. B.* **17**(6), pp. 3390–3393, 1999.

[133] J. Scheuer, W. M. J. Green, G. A. DeRose and A. Yariv, "Lasing and mode switching in circular Bragg nano-resonators," in Proceedings of the *Conference on Lasers and Electro-Optics/Quantum Electronics and Laser Science Conference*, Baltimore, Maryland, 2005, Paper QME1.

[134] J. Scheuer, W. M. J. Green, G. A. DeRose and A. Yariv, "Lasing from a circular Bragg nanocavity with an ultra-small modal volume," submitted, 2005.

[135] J. Scheuer and A. Yariv, "Circular photonic crystal resonators," *Phys. Rev. E.* **70**, pp. 036603, 2004.

[136] T. Yoshie, O. B. Shchekin, H. Chen, D. G. Deppe and A. Scherer, "Planar photonic crystal nanolasers (II): low-threshold quantum dot lasers," *IEICE Trans. Electron.* **E87-C**(3), pp. 300–307, 2004.

[137] M. Koshiba, *Optical Waveguide Theory by the Finite Element Method*, KTK Scientific Publishers and Kluwer Academic Publishers, Dordrecht, Holland, 1992.

[138] M. S. Stern, "Semivectorial polarised finite difference method for optical waveguides with arbitrary index profiles," *IEE Proc. J.* **135**(1), pp. 56–63, 1988.

[139] W. H. Press, S. A. Teukolsky, W. T. Vetterling and B. P. Flannery, *Numerical Recipes in C: The Art of Scientific Computing*, Cambridge University Press, Cambridge, 2nd edition, 1992.

[140] P. D. Trinh, S. Yegnanarayanan and B. Jalali, "Integrated optical directional couplers in silicon-on-insulator," *Electron. Lett.* **31**(24), pp. 2097–2098, 1995.

[141] D. V. Tishinin, P. D. Dapkus, A. E. Bond, I. Kim, C. K. Lin and J. O'Brien, "Vertical resonant couplers with precise coupling efficiency control fabricated by wafer bonding," *IEEE Photon. Technol. Lett.* **11**(8), pp. 1003–1005, 1999.

[142] B. E. Little, S. T. Chu, W. Pan, D. Ripin, T. Kaneko, Y. Kokubun and E. Ippen, "Vertically coupled glass microring resonator channel dropping filters," *IEEE Photon. Technol. Lett.* **11**(2), pp. 215–217, 1999.

[143] Y. Shani, C. H. Henry, R. C. Kistler, R. F. Kazarinov and K. J. Orlowsky, "Integrated optic adiabatic devices on silicon," *IEEE J. Quantum Electron.* **27**(3), pp. 556–566, 1991.

[144] K. Kasaya, O. Mitomi, M. Naganuma, Y. Kondo and Y. Noguchi, "A simple laterally tapered waveguide for low-loss coupling to single-mode fibers," *IEEE Photon. Technol. Lett.* **5**(3), pp. 345–347, 1993.

[145] E. C. M. Pennings, R. J. Deri, A. Scherer, R. Bhat, T. R. Hayes, N. C. Andreadakis, M. K. Smit, L. B. Soldano and R. J. Hawkins, "Ultracompact, low-loss directional couplers on InP based on self-imaging by multimode interference," *Appl. Phys. Lett.* **59**(16), pp. 1926–1928, 1991.

[146] O. Bryngdahl, "Image formation using self-imaging techniques," *J. Opt. Soc. Am.* **63**(4), pp. 416–419, 1973.

[147] R. Ulrich and G. Ankele, "Self-imaging in homogeneous planar optical waveguides," *Appl. Phys. Lett.* **27**(6), pp. 337–339, 1975.

[148] L. B. Soldano, F. B. Veerman, M. K. Smit, B. H. Verbeek, A. H. Dubost and E. C. M. Pennings, "Planar monomode optical couplers based on multimode interference effects," *J. Lightwave Technol.* **10**(12), pp. 1843–1850, 1992.

[149] L. B. Soldano and E. C. M. Pennings, "Optical multi-mode interference devices based on self-imaging: principles and applications," *J. Lightwave Technol.* **13**(4), pp. 615–627, 1995.

[150] L. H. Spiekman, Y. S. Oei, E. G. Metaal, F. H. Groen, I. Moerman and M. K. Smit, "Extremely small multimode interference couplers and ultrashort bends on InP by deep etching," *IEEE Photon. Technol. Lett.* **6**(8), pp. 1008–1010, 1994.

[151] W. M. J. Green, R. K. Lee, G. A. DeRose, A. Scherer and A. Yariv, "Hybrid InGaAsP-InP Mach-Zehnder racetrack resonator for thermooptic switching and coupling control," *Opt. Express.* **13**(5), pp. 1651–1659, 2005.

[152] A. Yariv, "Critical coupling and its control in optical waveguide-ring resonator systems," *IEEE Photon. Technol. Lett.* **14**(4), pp. 483–485, 2002.

[153] A. Yariv, "Chapter 9: Electrooptic Modulation of Laser Beams," in *Optical Electronics in Modern Communications*. Oxford University Press, New York, 5th edition, 1997.

[154] R. L. Espinola, M.-C. Tsai, J. T. Yardley and R. M. Osgood, "Fast and low-power thermooptic switch on thin silicon-on-insulator," *IEEE Photon. Technol. Lett.* **15**(10), pp. 1366–1368, 2003.

[155] J. M. Choi, R. K. Lee and A. Yariv, "Ring fiber resonators based on fused-fiber grating add-drop filters: application to resonator coupling," *Opt. Lett.* **27**(18), pp. 1598–1600, 2002.

[156] W. T. Tsang, M. C. Wu, Y. K. Chen, F. S. Choa, R. A. Logan, S. N. G. Chu, A. M. Sergent, P. Magill, K. C. Reichmann and C. A. Burrus, "Long-wavelength InGaAsP/InP multiquantum well distributed feedback and distributed Bragg reflector lasers grown by chemical beam epitaxy," *IEEE J. Quantum Electron.* **30**(6), pp. 1370–1380, 1994.

[157] S. Charbonneau, E. S. Koteles, P. J. Poole, J. J. He, G. C. Aers, J. Haysom, M. Buchanan, Y. Feng, A. Delage, F. Yang, M. Davies, R. D. Goldberg, P. G. Piva and I. V. Mitchell, "Photonic integrated circuits fabricated using ion implantation," *IEEE J. Sel. Top. Quantum Electron.* **4**(4), pp. 772–793, 1998.

[158] S. D. McDougall, O. P. Kowalski, C. J. Hamilton, F. Camacho, B. Qiu, M. Ke, R. M. De La Rue, A. C. Bryce and J. H. Marsh, "Monolithic integration via a universal damage enhanced quantum-well intermixing technique," *IEEE J. Sel. Top. Quantum Electron.* **4**(4), pp. 636–646, 1998.

[159] H. S. Djie, C. Sookdhis, T. Mei and J. Arokiaraj, "Photonic integration using inductively coupled argon plasma enhanced quantum well intermixing," *Electron. Lett.* **38**(25), pp. 1672–1673, 2002.

[160] P. V. Studenkov, M. R. Gokhale, J. C. Dries and S. R. Forrest, "Monolithic integration of a quantum-well laser and an optical amplifier using an asymmetric twin-waveguide structure," *IEEE Photon. Technol. Lett.* **10**(8), pp. 1088–1090, 1998.

[161] S. J. Choi, K. Djordjev, S. J. Choi and P. D. Dapkus, "Microdisk lasers vertically coupled to output waveguides," *IEEE Photon. Technol. Lett.* **15**(10), pp. 1330–1332, 2003.

[162] P. Y. Yu and M. Cardona, "Chapter 6: Optical Properties I," in *Fundamentals of Semiconductors: Physics and Materials Properties*. Springer-Verlag, New York, 3rd edition, 2003.

[163] S. Adachi, "Material parameters of In(1-x)Ga(x)As(y)P(1-y) and related binaries," *J. Appl. Phys.* **53**(12), pp. 8775–8792, 1982.

[164] W. Liang, Y. Huang, Y. Xu, R. K. Lee and A. Yariv, "Highly sensitive fiber Bragg grating refractive index sensors," *Appl. Phys. Lett.* **86**, pp. 151122, 2005.

[165] B. J. Luff, R. D. Harris, J. S. Wilkinson, R. Wilson and D. J. Schiffrin, "Integrated-optical directional coupler biosensor," *Opt. Lett.* **21**(8), pp. 618–620, 1996.

[166] B. J. Luff, J. S. Wilkinson, J. Piehler, U. Hollenbach, J. Ingenhoff and N. Fabricius, "Integrated optical Mach-Zehnder biosensor," *J. Lightwave Technol.* **16**(4), pp. 583–592, 1998.

[167] K. R. Rogers, "Principles of affinity-based biosensors," *Mol. Biotechnol.* **14**(2), pp. 109–129, 2000.

[168] S. Y. Wu, H. P. Ho, W. C. Law, C. Lin and S. K. Kong, "Highly sensitive differential phase-sensitive surface plasmon resonance biosensor based on the Mach-Zehnder configuration," *Opt. Lett.* **29**(20), pp. 2378–2380, 2004.

[169] C.-Y. Chao and L. J. Guo, "Biochemical sensors based on polymer microrings with sharp asymmetrical resonance," *Appl. Phys. Lett.* **83**(8), pp. 1527–1529, 2003.

[170] E. Chow, A. Grot, L. W. Mirkarimi, M. Sigalas and G. Girolami, "Ultracompact biochemical sensor built with two-dimensional photonic crystal microcavity," *Opt. Lett.* **29**(10), pp. 1093–1095, 2004.

[171] S. Chan, P. M. Fauchet, Y. Li, L. J. Rothberg and B. L. Miller, "Porous silicon microcavities for biosensing applications," *Phys. Stat. Sol. A.* **182**(1), pp. 541–546, 2000.

[172] M. Loncar, A. Scherer and Y. Qiu, "Photonic crystal laser sources for chemical detection," *Appl. Phys. Lett.* **82**(26), pp. 4648–4650, 2003.

[173] M. L. Adams, *Integration of Optoelectronics and Microfluidics of Biological and Chemical Sensing*, Ph. D. Thesis, California Insititute of Technology, 2004.

[174] W. M. J. Green, J. Scheuer, G. DeRose and A. Yariv, "Ultra-sensitive biochemical sensor based on circular Bragg micro-cavities," in Proceedings of the *Conference on Lasers and Electro-Optics/Quantum Electronics and Laser Science Conference*, Baltimore, Maryland, 2005, Paper CPDA7.

[175] T. Thorsen, S. J. Maerkl and S. R. Quake, "Microfluidic large-scale integration," *Science.* **298**(5593), pp. 580–584, 2002.

[176] J. R. Anderson, D. T. Chiu, R. J. Jackman, O. Cherniavskaya, J. C. McDonald, H. Wu, S. H. Whitesides and G. M. Whitesides, "Fabrication of topologically complex three-dimensional microfluidic systems in PDMS by rapid prototyping," *Anal. Chem.* **72**(14), pp. 3158–3164, 2000.

[177] F. Prieto, B. Sepulveda, A. Calle, A. Llobera, C. Dominguez, A. Abad, A. Montoya and L. M. Lechuga, "An integrated optical interferometric nanodevice based on silicon technology for biosensor applications," *Nanotechnology.* **14**(8), pp. 907–912, 2003.

[178] L. A. Coldren and S. W. Corzine, "Chapter 6: Perturbation and Coupled-Mode Theory," in *Diode Lasers and Photonic Integrated Circuits.* Wiley-Interscience Publications, New York, 1995.

[179] P. Mach, T. Krupenkin, S. Yang and J. A. Rogers, "Dynamic tuning of optical waveguides with electrowetting pumps and recirculating fluid channels," *Appl. Phys. Lett.* **81**(2), pp. 202–204, 2002.

[180] K. Mogensen, Y. C. Kwok, J. C. T. Eijkel, N. J. Petersen, A. Manz and J. P. Kutter, "A microfluidic device with an integrated waveguide beam splitter for velocity measurements of flowing particles by Fourier transformation," *Anal. Chem.* **75**(18), pp. 4931–4936, 2003.

[181] M. Fujita and T. Baba, "Proposal and finite-difference time-domain simulation of whispering gallery mode microgear cavity," *IEEE J. Quantum Electron.* **37**(10), pp. 1253–1258, 2001.

[182] M. Fujita and T. Baba, "Microgear laser," *Appl. Phys. Lett.* **80**(12), pp. 2051–2053, 2002.